nature chemistry

Supplementary information

https://doi.org/10.1038/s41557-025-02045-x

Wavelength-steered directional rotation in an autonomous light-driven molecular motor

In the format provided by the authors and unedited

Table of contents

1. Experimental details

Solvents and reagents formaldehyde, glyoxal, ammonium acetate, ammonium hexafluorophosphate, *tert*-butylamine, potassium carbonate, sodium nitrite, hexafluorophosphoric acid, imidazole, 4-*tert*-butylaniline, benzyl bromide, silver oxide, (S)-(−)-1-Phenylethanol, triphenyl phosphine and carbon tetrachloride were all used as supplied by FluoroChem, Merck or VWR without further purification. Flash column chromatography was performed using Sigma Aldrich Silica 40 (230-400 mesh size or 40-63 μm) as the stationary phase. Gel permeation chromatography was performed using Biorad Biobeads SX-1 as the stationary phase. Thin layer chromatography was performed on TLC Silica gel 60 F254 coated aluminium plates from Merck.

NMR measurements

^{1}H NMR spectra were recorded on an Agilent DD2 spectrometer operating at 500 MHz or a Varian Mercury spectrometer operating at 400 MHz; ^{13}C NMR spectra were recorded on an Agilent DD2 spectrometer operating at 126 MHz or a Varian Mercury spectrometer operating at 101 MHz; ^{19}F NMR spectra were recorded on an Agilent DD2 spectrometer operating at 470 MHz. Chemical shifts are quoted in ppm relative to tetramethylsilane ($SiMe_4$, δ = 0 ppm), using the residual solvent peak as a reference standard; all coupling constants (*J*) are expressed in Hertz (Hz). The samples were irradiated directly inside the thermostated NMR probe, using a 1 mm silica core optical fiber (Thorlabs) connected to a Prizmatix UHP-T-365-SR LED Illuminator (1.5 W, λ_{max}= 369 nm, FWHM, 15.56 nm) through a FCA-SMA adaptor. At its other end, the protective coating of the optical fiber was removed (about 6 cm) and the exposed fiber was sanded to enable the diffusion of light from the fiber core into the solution. The fiber prepared in this way was immersed directly into the thermostated solution (550 μL of 10 mM or 5 mM solution of the rotor) in the NMR tube. The obtained experimental data were processed using the softwares MestReNova and OriginPro 2019.

UV irradiation experiments

Absorption spectra were recorded on a Perkin Elmer Lambda750 double beam spectrophotometer using 10 mm pathlength quartz cuvettes (Hellma). Irradiation experiments were performed on air equilibrated solutions, thoroughly stirred, using a medium pressure Hg lamp (200 W) at room temperature. The Hg lamp was also coupled with an Avantes StarLine AvaSpec-ULS2048CL-EVO-RS spectrophotometer to collect absorption spectra with high rates under continuous irradiation. The spectrophotometer was equipped with an optical fiber which enables the fast acquisition of absorption spectra (ms) and concomitant *in situ* irradiation. The desired wavelength of irradiation was selected using an appropriate interference filter. The incident photon flux of the irradiation lamp was determined to be 4.4×10^{-9} Einstein s^{-1}, 2.8×10^{-9} Einstein s^{-1} and 4.3×10^{-9} Einstein s^{-1} respectively at 365 nm, 405 nm and 436 nm, using the 4,4′-dimethylazobenzene actinometer.[1] The absorption spectra of the unknown *Z* isomers were extrapolated mathematically, according to the method reported by Fischer in 1967.[2] The photoisomerization quantum yields ($\Phi_{E\rightarrow Z}$) were determined from the disappearance of the π-π* band of the azoimidazolium unit by fitting the initial part of the global photokinetic[3] taking into account just low conversion percentages (<10%) and the thermal back-isomerization contribution. This choice was required by the need to consider negligible the quantum yield of the photochemical back-isomerization processes ($\Phi_{Z\rightarrow E}$), since only mathematically extrapolated absorption spectra of pure *Z* isomers could be obtained for the investigated molecules. Determination of $\Phi_{Z\rightarrow E}$ was also attempted, but the high uncertainty on the molar absorption coefficient of the *Z* form prevented its accurate assessment. The fraction of light transmitted at the irradiation wavelength was taken into account in the calculation of the quantum yields. The fitting was performed using the software Berkeley Madonna. The rate constants for thermal back-isomerization reactions were obtained by fitting the

back-isomerization spectral data at the maximum wavelength against time using a first-order kinetics (exponential) model in OriginPro 2019.

2. Synthetic procedures

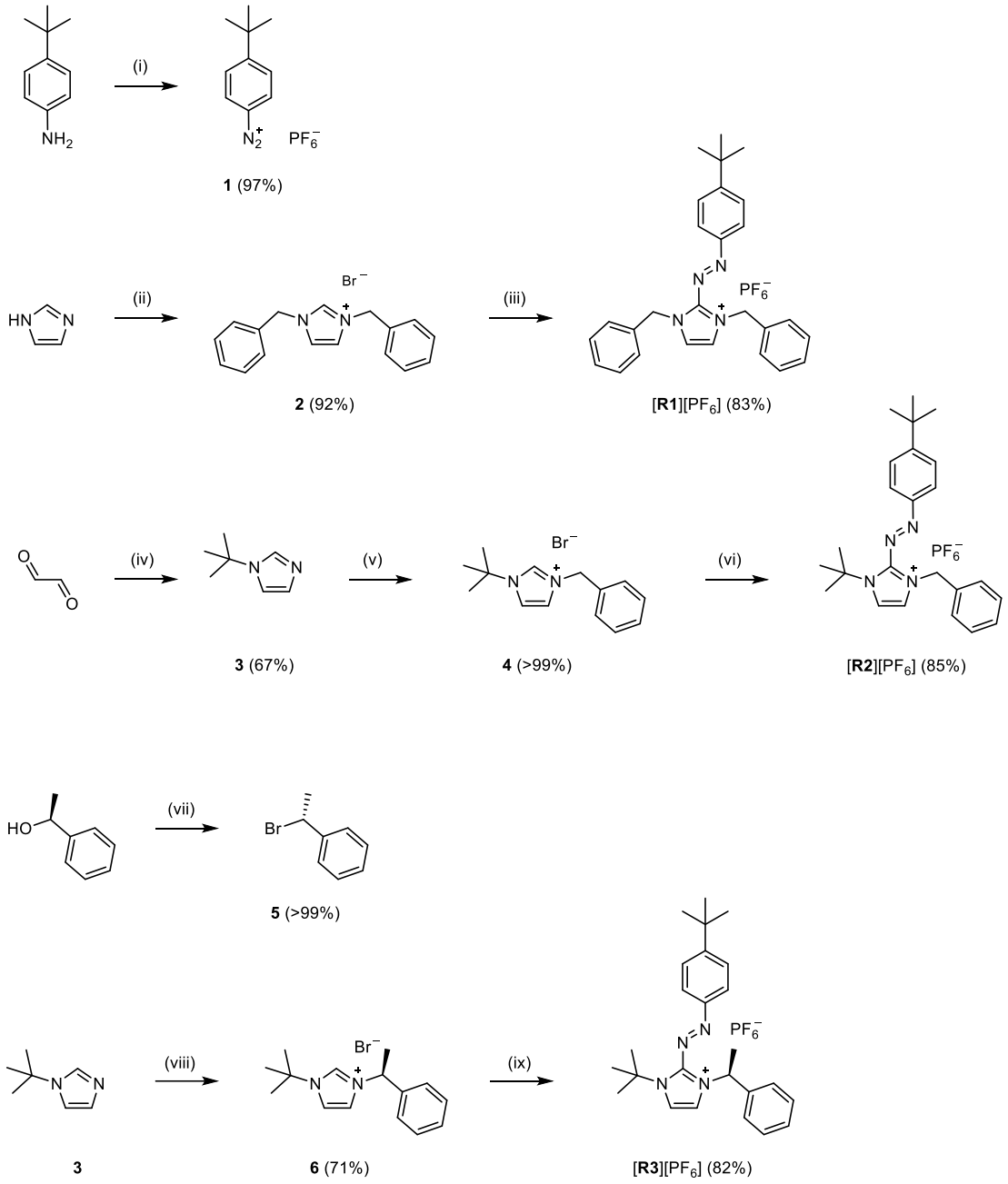

Supplementary Fig.1. Synthetic routes to [**R1**][PF_6], [**R2**][PF_6] and [**R3**][PF_6]; i) HPF_6, $NaNO_2$; ii) K_2CO_3, BnBr; iii) Ag_2O, **1**; iv) $tBuNH_2$, NH_4OH, HCHO; v) BnBr; vi) Ag_2O, **1**; vii) PPh_3, CBr_4; viii) **5**; ix) Ag_2O, **1**.

p-tert-butylphenyldiazonium hexafluorophosphate, 1

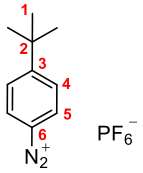

Adapting a reported procedure,[4] *p-tert*-butylaniline (1.49 g, 10 mmol) was suspended in water (150 mL) and reacted with an aqueous solution of hexafluorophosphoric acid (6.04 M, 25 mmol, 4.14 mL) at 0 °C until complete dissolution. An aqueous solution (2 mL) of sodium nitrite (1.03 g, 15 mmol) was dropwise added and the resulting mixture was stirred at 0 °C for 40 min, with the formation of the product as a colourless precipitate. The latter was collected by filtration and washed with water (3×50 mL) and diethyl ether (3×50 mL) to provide **1** as a colourless solid (2.96 g, 97%). ^{1}H NMR (500 MHz, 298 K, Acetone-d_6) δ 8.72 (d, J = 9.0 Hz, 2H, **5**), 8.15 (d, J = 9.0 Hz, 2H, **4**), 1.43 (s, 9H, **1**). ^{13}C NMR (101 MHz, 298 K, Acetone-d_6) δ 168.0, 133.6, 130.0, 112.3, 37.5, 30.6. ^{19}F NMR (470 MHz, 298 K, Acetone-d_6) δ –72.20 (d, J = 707.8 Hz, 6F, PF_6).

N,N'-dibenzylimidazolium bromide, 2

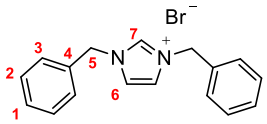

An acetonitrile solution (60 mL) of imidazole (1.00 g, 14.7 mmol), benzyl bromide (5.25 mL, 44.1 mmol) and potassium carbonate (4.06 g, 29.4 mmol) was stirred at 83 °C for 16 h. The resulting mixture was cooled down to room temperature, the solvent removed under reduced pressure and the residue extracted in dichloromethane (30 mL) and filtered. Removal of the solvent under reduced pressure provided a crude solid which was further triturated with diethyl ether (3×20 mL) to provide **2** as an off-white solid (4.45 g, 92%). ^{1}H NMR (500 MHz, 298 K, Acetonitrile-d_3) δ 9.81 (t, J = 1.7 Hz, 1H, **7**), 7.56 (d, J = 1.7 Hz, 2H, **6**), 7.51 - 7.45 (m, 4H, **3**), 7.42 - 7.33 (m, 6H, **2**+**3**), 5.47 (s, 4H, **5**). ^{13}C NMR (126 MHz, 298 K, Acetonitrile-d_3) δ 137.3 (**7**), 135.1 (**4**), 130.0 (**2** or **1**), 129.9 (**1** or **2**), 129.6 (**3**), 123.4 (**6**), 53.4 (**5**).

[R1][PF$_6$]

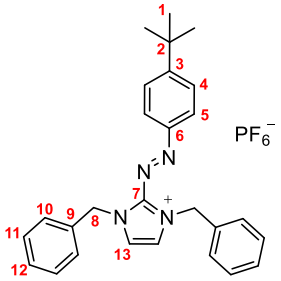

Solid silver oxide (927 mg, 4.00 mmol) was added to a dry dichloromethane solution (50 mL) of imidazolium **2** (358 mg, 2.0 mmol) and the resulting suspension was stirred at room temperature for 18 h in the dark. The resulting mixture was filtered through celite, the solvent was removed under reduced pressure to provide the intermediate silver NHC complex as a dark solid, which was redissolved in dichloromethane (40 mL). The solution was cooled down to 0 °C and solid **1** (2.76 g, 10.00 mmol) was added in a single portion to provide an orange mixture that was warmed up to room temperature and stirred for 18 h. The solution was filtered and the solvent was removed under reduced pressure to provide a dark orange solid which was purified by recrystallization from methanol to obtain product **[R1][PF$_6$]** as bright orange crystals (921 mg, 83%). ^{1}H NMR (500 MHz, 298 K, Chloroform-*d*) δ 7.89 (d, *J* = 8.7 Hz, 2H, **5**), 7.61 (d, *J* = 8.7 Hz, 2H, **4**), 7.43 (s, 2H, **13**), 7.41 - 7.29 (m, 10H, **10**+**11**+**12**), 5.69 (s, 4H, **8**), 1.38 (s, 9H, **1**). ^{13}C NMR (126 MHz, 298 K, Chloroform-*d*) δ 161.2 (**3**), 150.9 (**6**), 143.3 (**7**), 133.0 (**9**), 129.6 (**11**), 129.5 (**12**), 128.5 (**10**), 127.2 (**4**), 124.6 (**5**), 123.7 (**13**), 53.5 (**8**), 35.9 (**2**), 31.1 (**1**). ^{19}F NMR (470 MHz, 298 K, Chloroform-*d*) δ –73.01 (d, *J* = 712.8 Hz, 6F. PF_6). HRMS-ESI (m/z): calcd for [$C_{27}H_{29}N_4$], 409.2392; found 409.2392 [**R1**]$^+$.

***N-tert*-butylimidazole, 3**

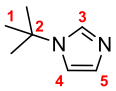

Adapting a reported procedure,[5] a mixture of an aqueous glyoxal solution (40%, 40 mmol, 4.59 mL) and an aqueous formaldehyde solution (40%, 40 mmol, 2.78 mL) and a separate mixture of tert-butylamine (40 mmol, 4.2 mL) and an aqueous ammonium hydroxide solution (30%, 40 mmol, 5.20 mL) were independently and simultaneously dropwise added to water (30 mL) at 100 °C. The mixture obtained upon completion of the addition was stirred at 100 °C for 1 h. Upon cooling to room temperature, the mixture was extracted with diethyl ether (3×50 mL) and the organic phase washed with water (3×25 mL) and dried over anhydrous Na_2SO_4. Filtration through a silica pad and removal of the solvent provided compound **3** as a yellow-orange oil (3.33 g, 67%). ^{1}H NMR (500 MHz, 298 K, Chloroform-*d*) δ 7.56 (t, *J* = 1.2 Hz, 1H, **3**), 7.01 (t, *J* = 1.2 Hz, 1H, **5**), 6.99 (t, *J* = 1.4 Hz, 1H, **4**), 1.51 (s, 9H, **1**). ^{13}C NMR (101 MHz, 298 K; Chloroform-*d*) δ 134.4, 129.1, 116.3, 54.7, 30.6.

***N-tert*-butyl-*N'*-benzylimidazolium bromide, 4**

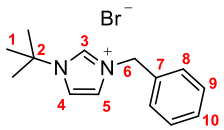

A toluene solution (10 mL) of **3** (372 mg, 3.0 mmol) and benzyl bromide (428 µL, 3.6 mmol) was reacted in a microwave reactor at 100 °C for 2 h. The clear toluene phase was decanted and the crude dark brown oil washed with toluene (3×10 mL). Solvent traces were removed under reduced pressure to provide **4** as a pale brown solid (883 mg, quantitative). ^{1}H NMR (500 MHz, 298 K, Chloroform-*d*) δ 10.61 (t, *J* = 1.7 Hz, 1H, **3**), 7.54 (t, *J* = 1.8 Hz, 1H, **4**), 7.53 - 7.47 (m, 2H, **8**), 7.43 (t, *J* = 1.8 Hz, 1H, **5**), 7.27 - 7.21 (m, 3H, **9**+**10**), 5.61 (s, 2H, **6**), 1.61 (s, 9H, **1**). ^{13}C NMR (126 MHz, 298 K, Chloroform-*d*) δ 135.3, 133.4, 129.2 (×3), 122.1, 119.9, 60.4, 52.8, 30.1.

[R2][PF$_6$]

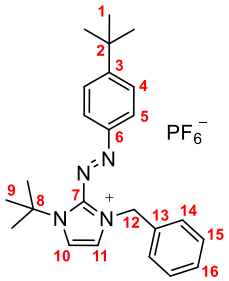

Solid silver oxide (959 mg, 4.14 mmol) was added to a dry dichloromethane solution (50 mL) of imidazolium **4** (611 mg, 2.07 mmol) and the resulting suspension was stirred at room temperature for 18 h in the dark. The resulting mixture was filtered through celite, the solvent was removed under reduced pressure to provide the intermediate silver NHC complex as a dark solid, which was redissolved in dichloromethane (40 mL). The solution was cooled down to 0 °C and solid **1** (3.17 g, 10.35 mmol) was added in a single portion to provide an orange mixture that was warmed up to room temperature and stirred for 18 h. The solution was filtered and the solvent was removed under reduced pressure to provide the crude product, which was purified through flash chromatography (methylene chloride/hexane gradient) and gel permeation chromatography (SX-3, methylene chloride) to obtain **[R2][PF$_6$]** as a bright orange solid (893 mg, 83%). ^{1}H NMR (500 MHz, 298 K, Chloroform-*d*) δ 7.87 - 7.81 (d, *J* = 7.4 Hz, 2H, **5**), 7.68 (d, *J* = 2.3 Hz, 1H, **10**), 7.65 - 7.59 (d, *J* = 7.4 Hz, 2H, **4**), 7.41 (d, *J* = 2.3 Hz, 1H, **11**), 7.40 - 7.31 (m, 3H, **15**+**16**), 7.26 (d, *J* = 5.2 Hz, 2H, **14**), 5.61 (s, 2H, **12**), 1.87 (s, 9H, **9**), 1.38 (s, 9H, **1**). ^{13}C NMR (126 MHz, 298 K, Chloroform-*d*) δ 160.9 (**3**), 150.8 (**6**), 143.8 (**7**), 133.0 (**13**), 129.6 (**15** or **16**), 129.3 (**16** or **15**), 128.2 (**14**), 127.3 (**4**), 124.5 (**5**), 123.6 (**11**), 121.0 (**10**), 64.4 (**8**), 55.3 (**12**), 35.9 (**2**), 31.1 (**1**), 30.4 (**9**). ^{19}F NMR (470 MHz, 298 K, Chloroform-*d*) δ –73.24 (d, *J* = 712.7 Hz, 6F, PF_6). HRMS-ESI (m/z): calcd for [$C_{24}H_{31}N_4$], 375.2549; found 375.2549 [**R2**]$^{+}$.

(*R*)-(1-bromoethyl)benzene, 5

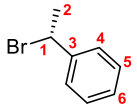

Adapting a reported procedure,[6] a dichloromethane solution (30 mL) of triphenyl phosphine (7.73 g, 29.5 mmol) and carbon tetrabromide (3.90 g, 11.8 mmol) was stirred for 40 min at room temperature inside a sealed vessel. A dichloromethane (30 mL) solution of (*S*)-(−)-1-Phenylethanol (1.2 g, 9.8 mmol) was added dropwise and the resulting mixture reacted at room temperature until TLC analysis showed complete consumption of the starting material. The mixture was diluted with a 3:1 diethyl ether:pentane mixture to precipitate triphenyl phosphine oxide and then filtered through a silica pad. Removal of the solvent under reduced pressure provided the product **5** as a pale brown solid (1.8 g, quantitative). ^{1}H NMR (500 MHz, 298 K, Chloroform-*d*) δ 7.47 - 7.42 (m, 2H, **4**), 7.37 - 7.32 (m, 2H, **5**), 7.31 - 7.27 (m, 1H, **6**), 5.22 (q, *J* = 6.9 Hz, 1H, **1**), 2.06 (d, *J* = 6.9 Hz, 3H, **2**). ^{13}C NMR (126 MHz, 298 K, Chloroform-*d*) δ 143.4, 128.8, 128.5, 126.9, 49.7, 27.0.

(*S*)-*N*-(tert-butyl)-*N*'-(1-phenylethyl)- imidazolium bromide, 6

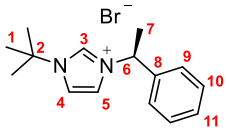

A toluene solution (10 mL) of **3** (124 mg, 1.0 mmol) and **5** (925 mg, 5.0 mmol) was heated at 50 °C for 12 h in a sealed tube. The clear toluene phase was decanted and the crude dark brown oil washed with toluene (3×20 mL). Solvent traces were removed under reduced pressure to provide **6** as a pale brown solid (231 mg, 71%). ^{1}H NMR (500 MHz, 298 K, Chloroform-*d*) δ 10.82 (d, *J* = 1.5 Hz, 1H, **3**), 7.58 - 7.52 (m, 2H, **9**), 7.40 (t, *J* = 1.9 Hz, 1H, **4**), 7.40 - 7.32 (m, 3H, **10**+**11**), 7.27 (d, *J* = 1.9 Hz, 1H, **5**), 6.38 (q, *J* = 7.1 Hz, 1H, **6**), 2.00 (d, *J* = 7.1 Hz, 3H, **7**), 1.73 (s, 9H, **1**). ^{13}C NMR (126 MHz, 298 K, Chloroform-*d*) δ 138.0, 135.7, 129.4, 129.4, 127.4, 119.9, 119.5, 60.8, 59.4, 30.3, 21.2.

[R3][PF$_6$]

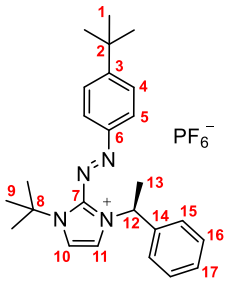

Solid silver oxide (264 mg, 1.14 mmol) was added to a dry dichloromethane solution (30 mL) of imidazolium **6** (176 mg, 0.57 mmol) and the resulting suspension was stirred at room temperature for 18 h in the dark. The resulting mixture was filtered through celite, the solvent was removed under reduced pressure to provide the intermediate silver NHC complex as a dark solid, which was redissolved in dichloromethane (20 mL). The solution was cooled down to 0 °C and solid **1** (873 mg, 2.85 mmol) was added in a single portion to provide an orange mixture that was warmed up to room temperature and stirred for 18 h. The solution was filtered and the solvent was removed under reduced pressure to provide the crude product, which was purified through flash chromatography (methylene chloride/hexane gradient) and gel permeation chromatography (SX-3, methylene chloride) to obtain **[R3][PF$_6$]** as an orange solid (250 mg, 82%). ^{1}H NMR (500 MHz, 298 K, Chloroform-*d*) δ 7.86 - 7.81 (m, 2H, **5**), 7.80 (d, *J* = 2.4 Hz, 1H, **10**), 7.68 (d, *J* = 2.4 Hz, 1H, **11**), 7.66 - 7.61 (m, 2H, **4**), 7.41 - 7.35 (m, 2H, **16**), 7.35 - 7.29 (m, 1H, **17**), 7.21 (dd, *J* = 7.1, 1.7 Hz, 2H, **15**), 6.27 (q, *J* = 7.0 Hz, 1H, **12**), 1.94 (d, *J* = 7.0 Hz, 3H, **13**), 1.85 (s, 9H, **9**), 1.39 (s, 9H, **1**). ^{13}C NMR (126 MHz, 298 K, Chloroform-*d*) δ 160.9 (**3**), 150.8 (**6**), 143.5 (**7**), 138.6 (**14**), 129.6 (**16**), 129.1 (**17**), 127.3 (**4**), 126.5 (**15**), 124.4 (**5**), 121.8 (**10**), 120.6 (**11**), 64.5 (**8**), 60.7 (**12**), 35.9 (**2**), 31.1 (**1**), 30.4 (**9**), 21.8 (**13**). ^{19}F NMR (470 MHz, 298 K, Chloroform-*d*) δ –73.26 (d, *J* = 712.7 Hz, 6F, PF$_6$). HRMS-ESI (m/z): calcd for [$C_{25}H_{33}N_4$], 389.2705; found 389.2705 [**R3**]$^+$.

3. NMR data

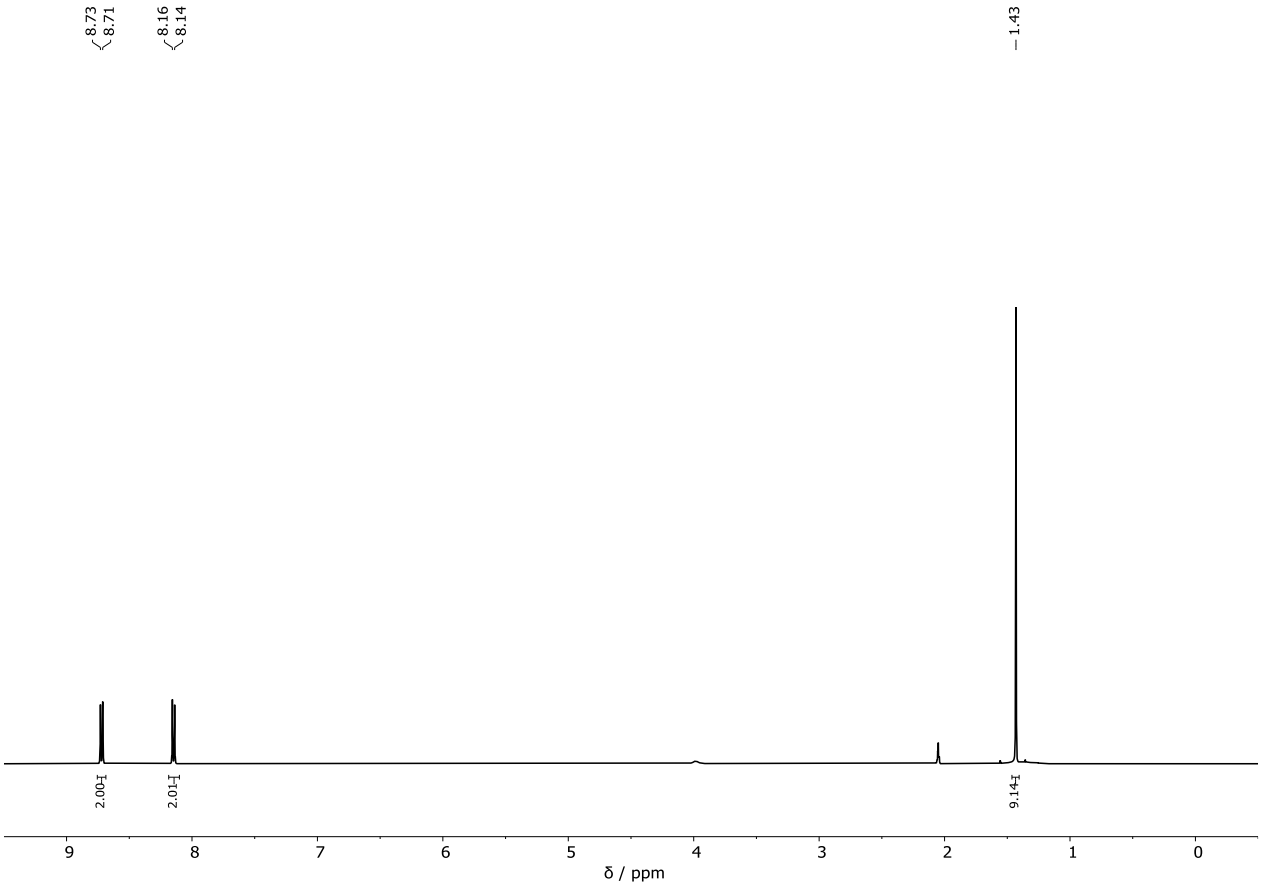

Supplementary Fig. 2. ^{1}H NMR spectrum of **1** (Acetone-d_6, 298 K, 500 MHz).

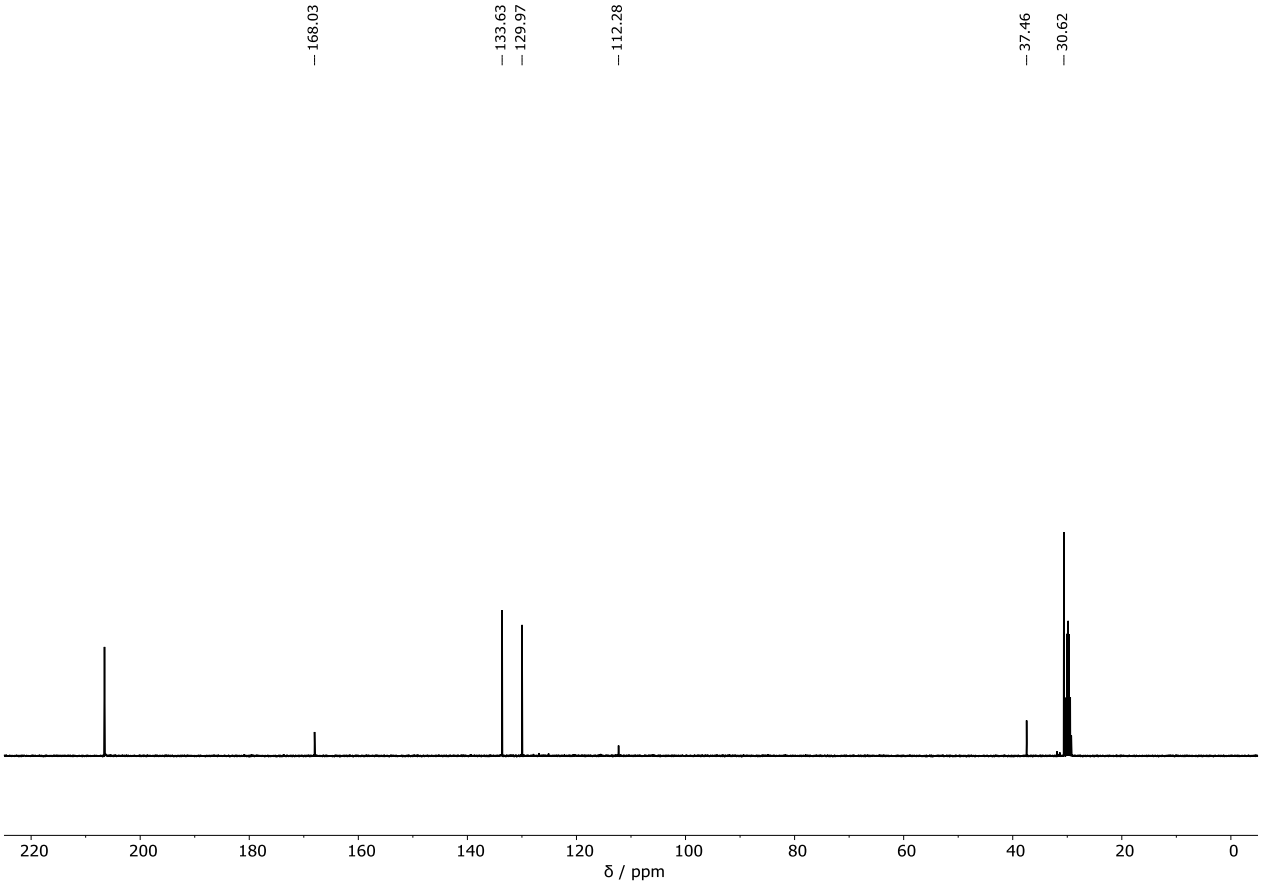

Supplementary Fig. 3. ^{13}C NMR spectrum of **1** (Acetone-d_6, 298 K, 101 MHz).

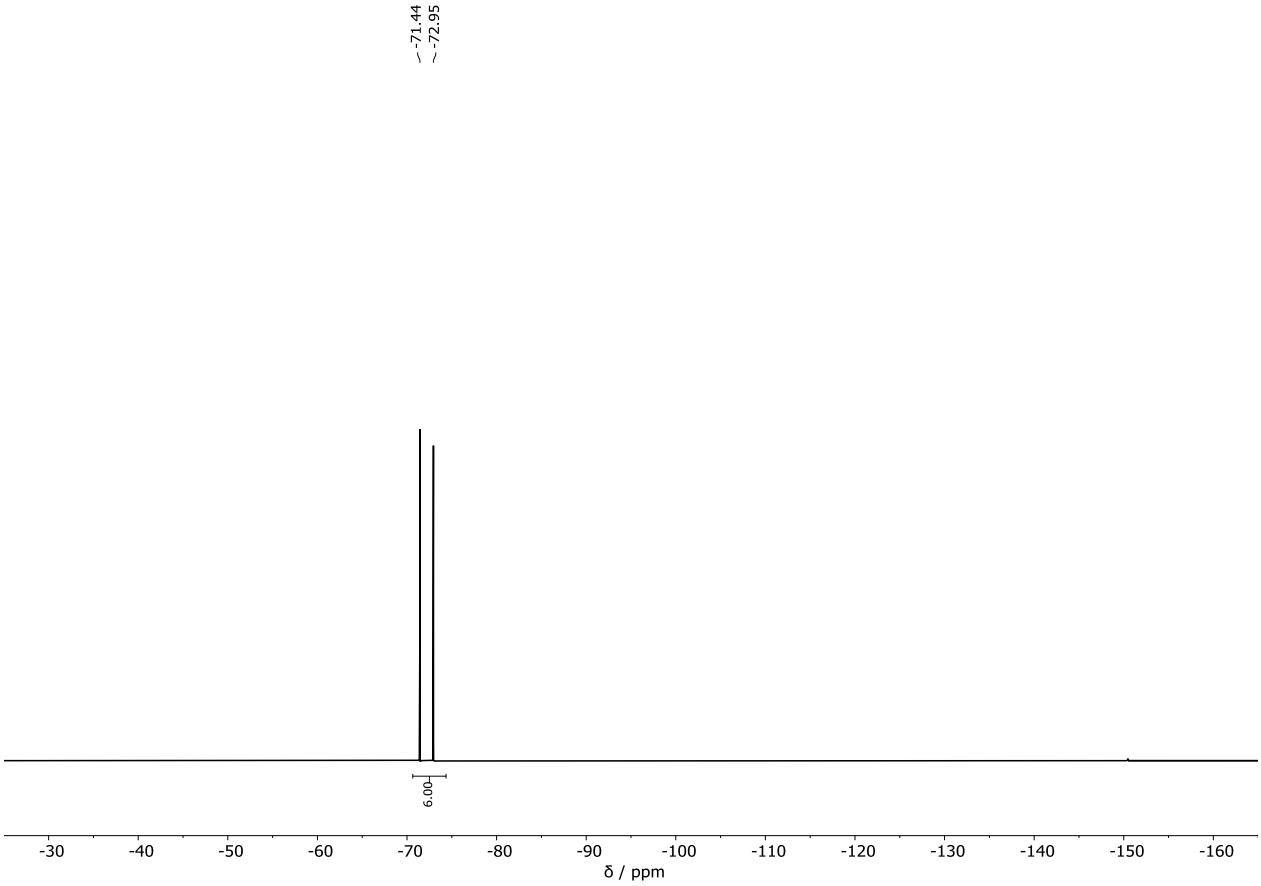

Supplementary Fig. 4. ^{19}F NMR spectrum of **1** (Acetone-d_6, 298 K, 470 MHz).

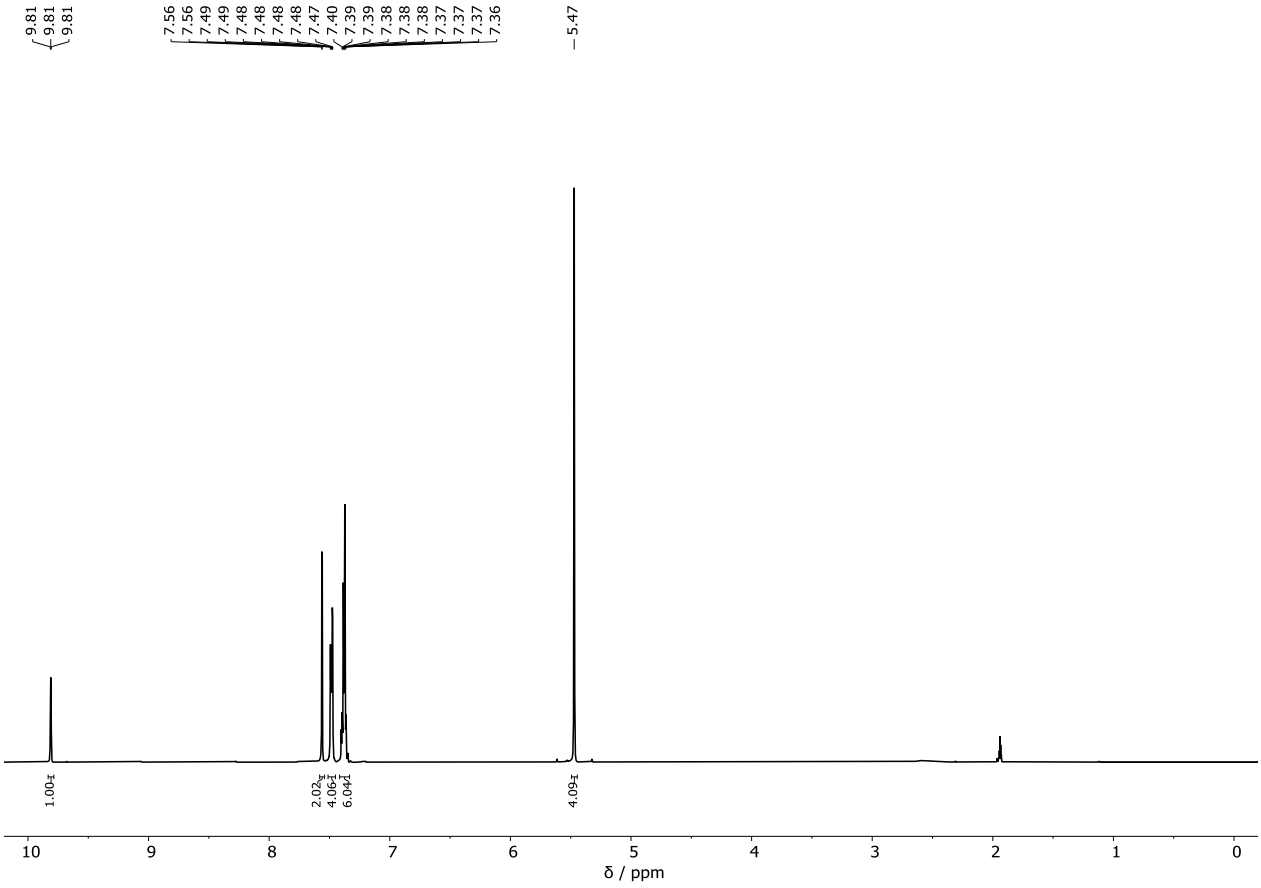

Supplementary Fig. 5. ^{1}H NMR spectrum of **2** (Acetonitrile-d_3, 298 K, 500 MHz).

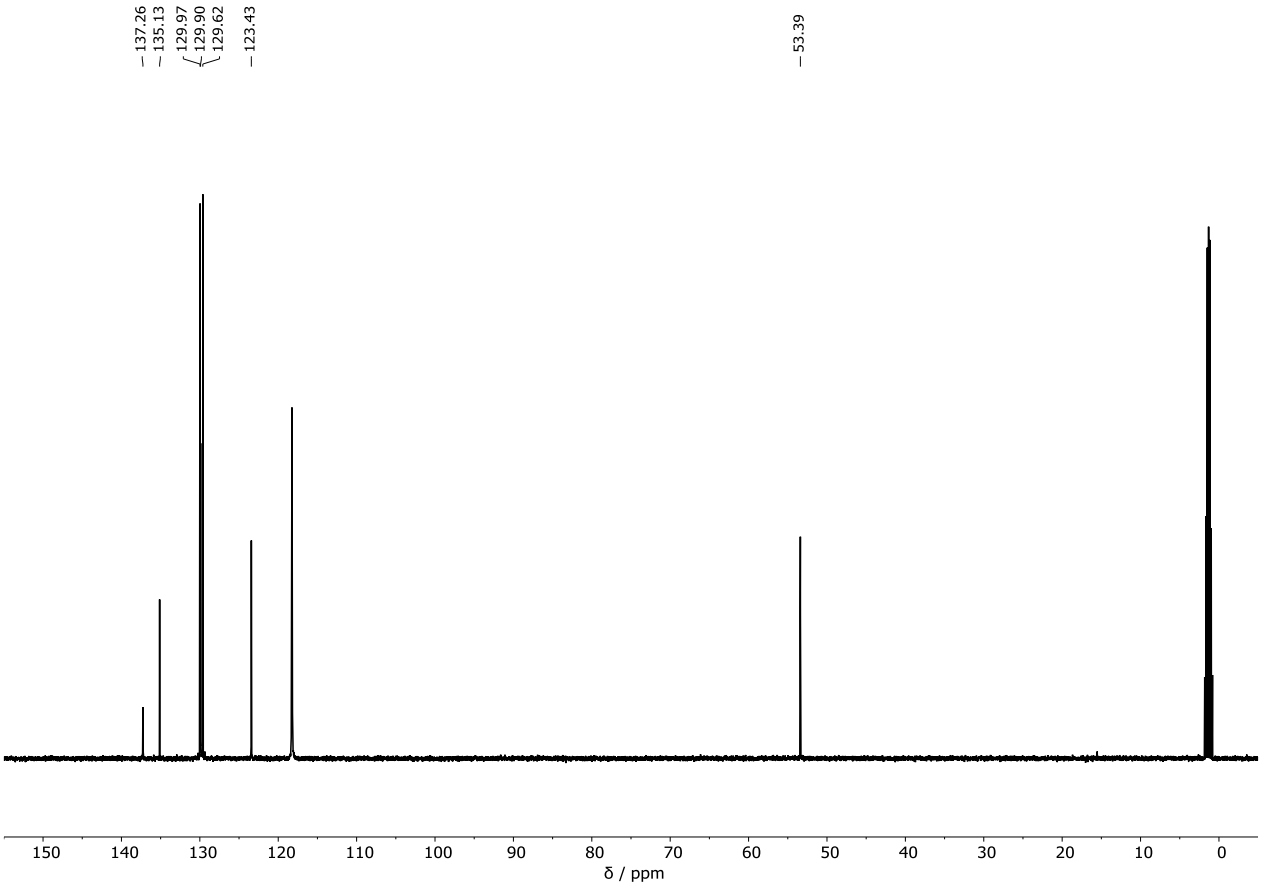

Supplementary Fig. 6. ^{13}C NMR spectrum of **2** (Acetonitrile-d_3, 298 K, 126 MHz).

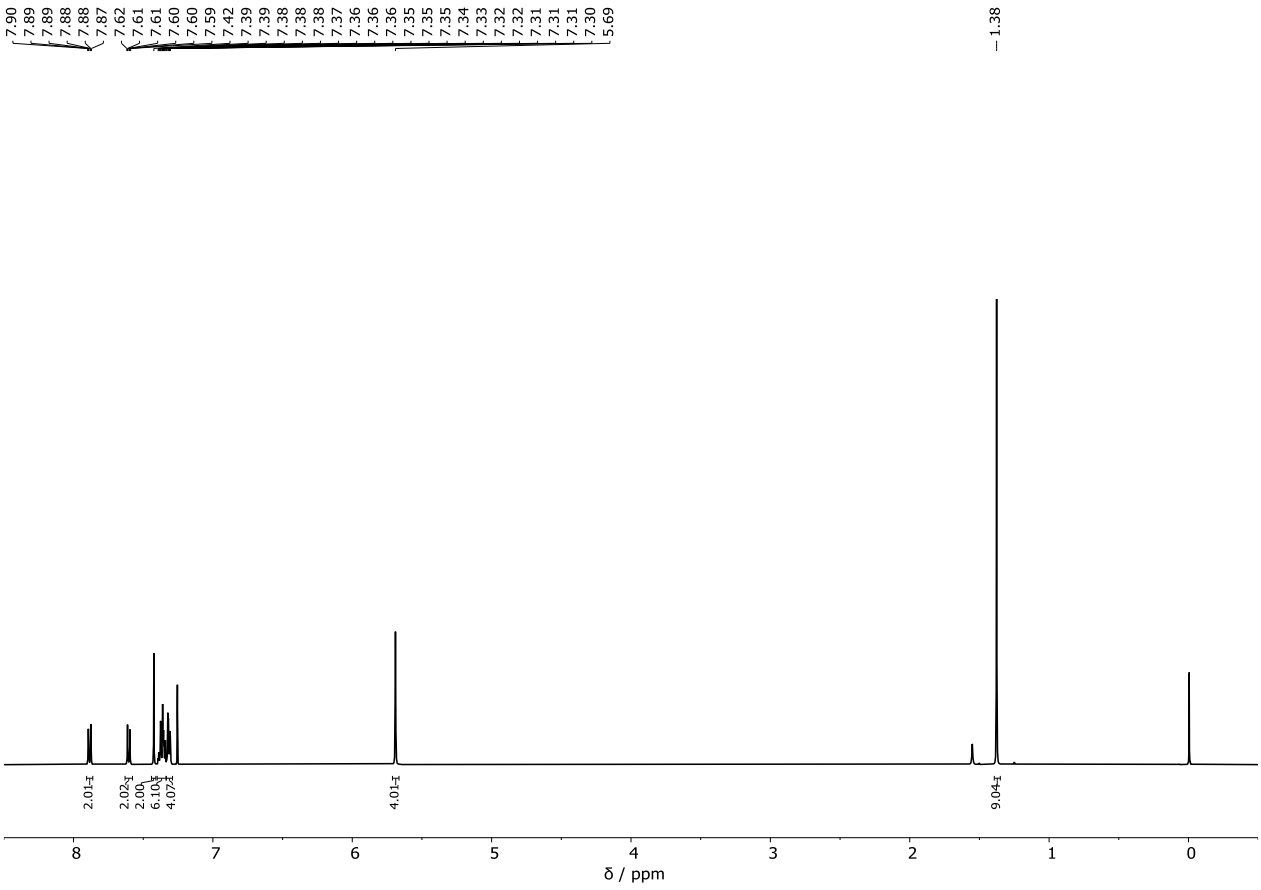

Supplementary Fig. 7. ^{1}H NMR spectrum of **[R1][PF_6]** (Chloroform-*d*, 298 K, 500 MHz).

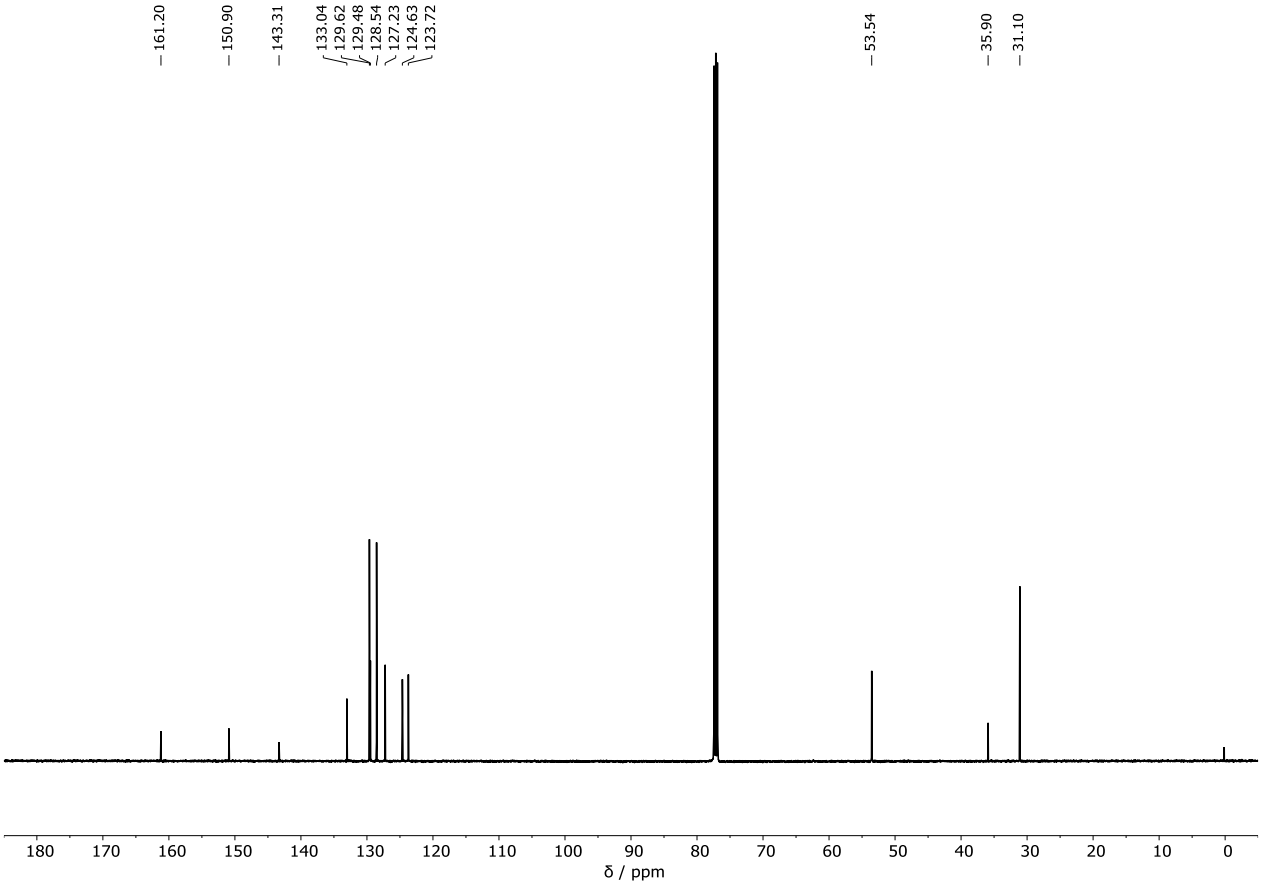

Supplementary Fig. 8. ^{13}C NMR spectrum of **[R1][PF$_6$]** (Chloroform-*d*, 298 K, 126 MHz).

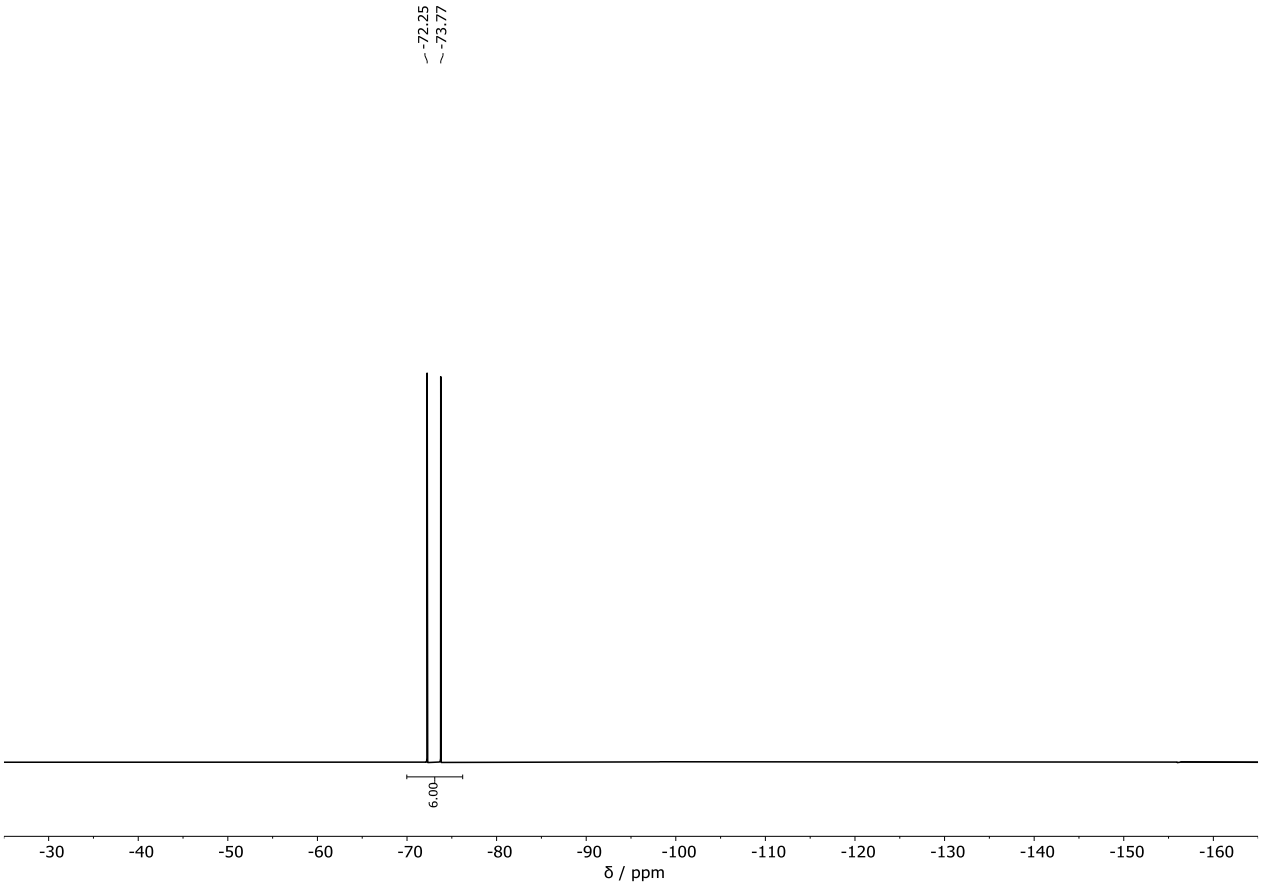

Supplementary Fig. 9. ^{19}F NMR spectrum of **[R1][PF$_6$]** (Chloroform-*d*, 298 K, 470 MHz).

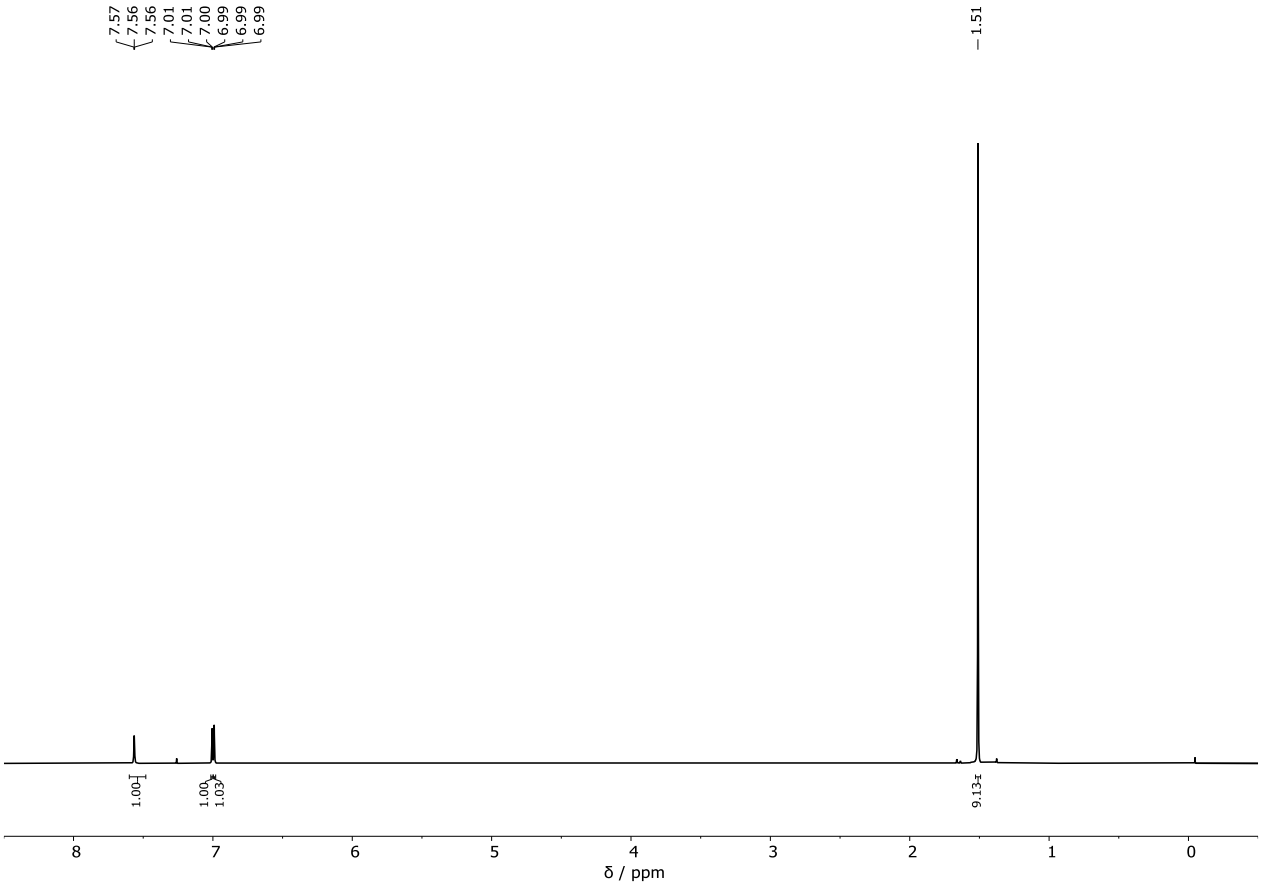

Supplementary Fig. 10. ^{1}H NMR spectrum of **3** (Chloroform-*d*, 298 K, 500 MHz).

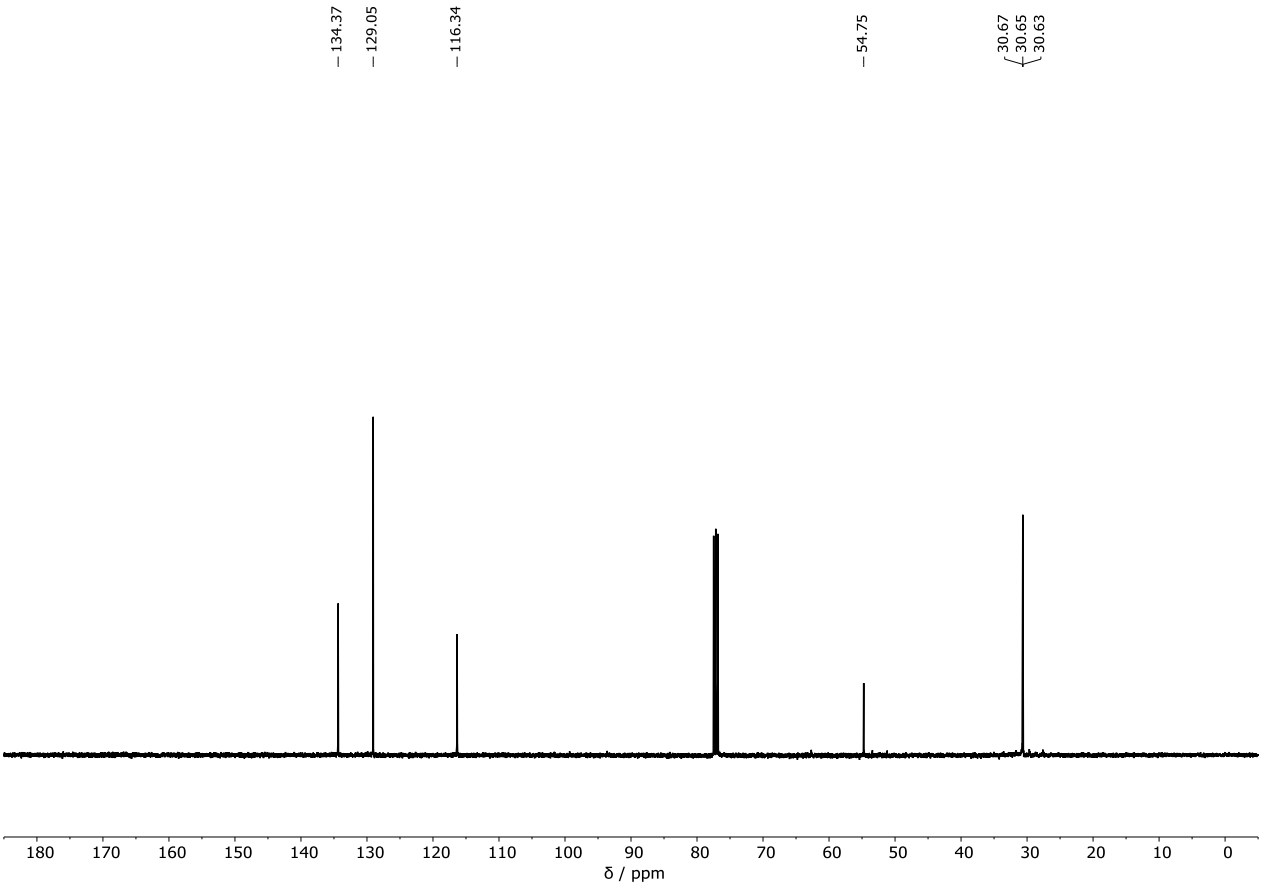

Supplementary Fig. 11. ^{13}C NMR spectrum of **3** (Chloroform-*d*, 298 K, 126 MHz).

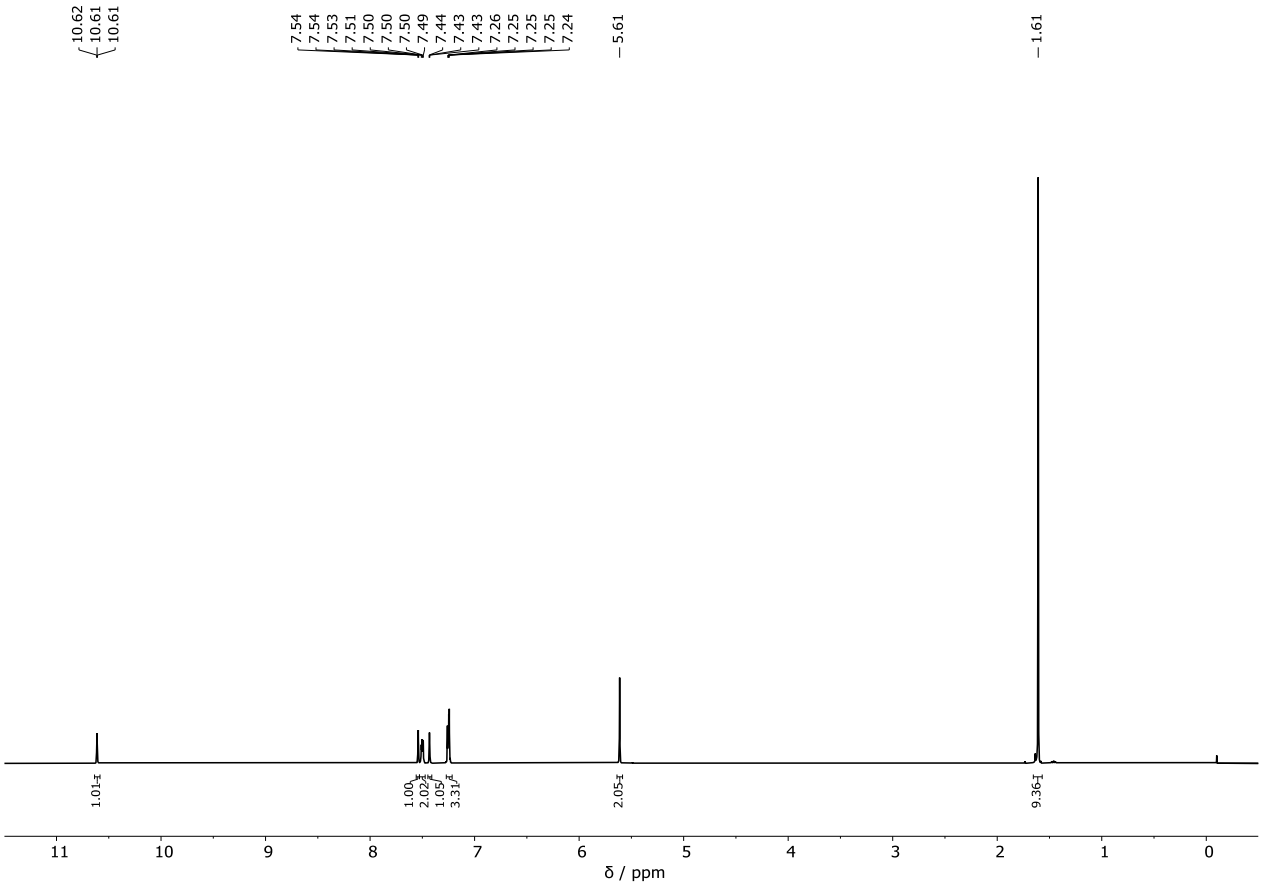

Supplementary Fig. 12. ^{1}H NMR spectrum of **4** (Chloroform-*d*, 298 K, 500 MHz).

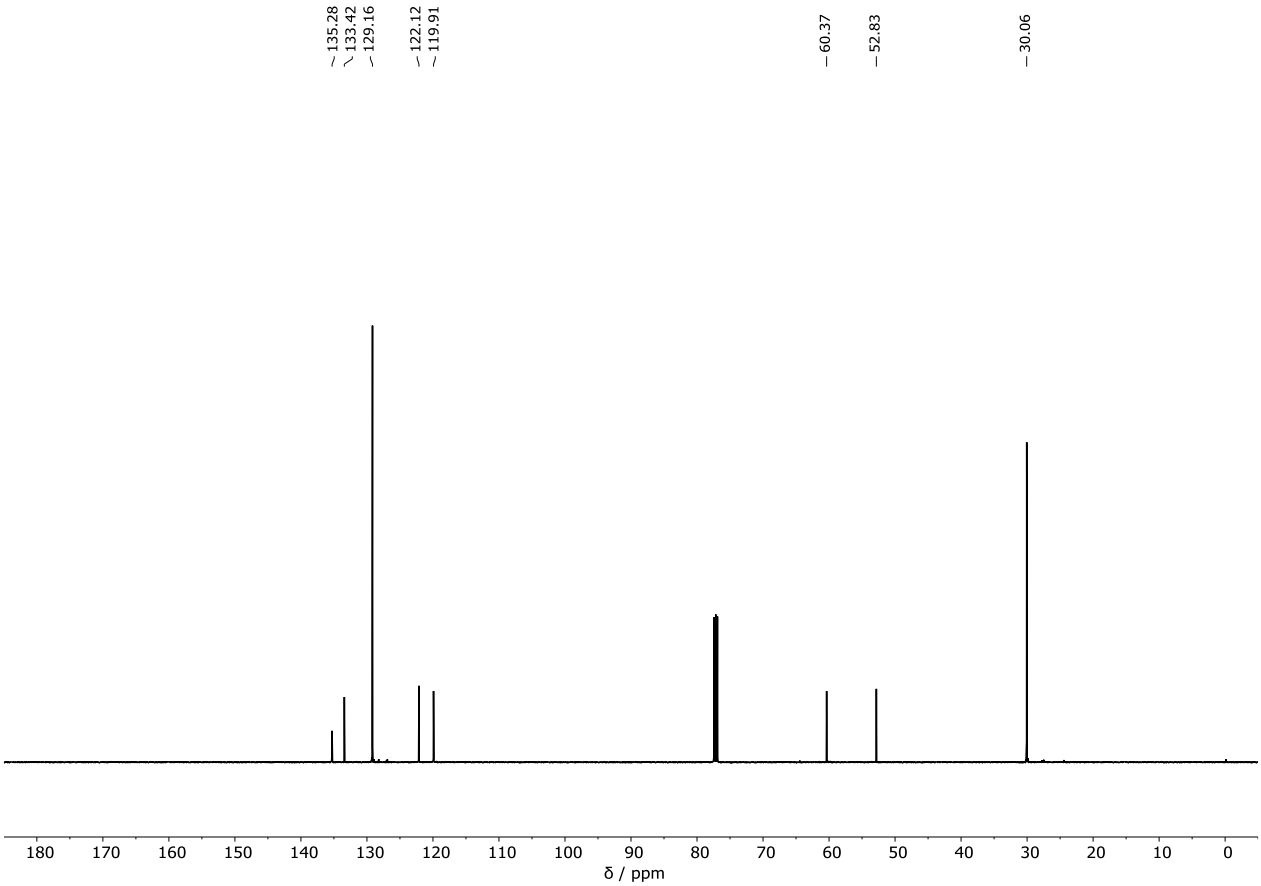

Supplementary Fig. 13. ^{13}C NMR spectrum of **4** (Chloroform-*d*, 298 K, 126 MHz).

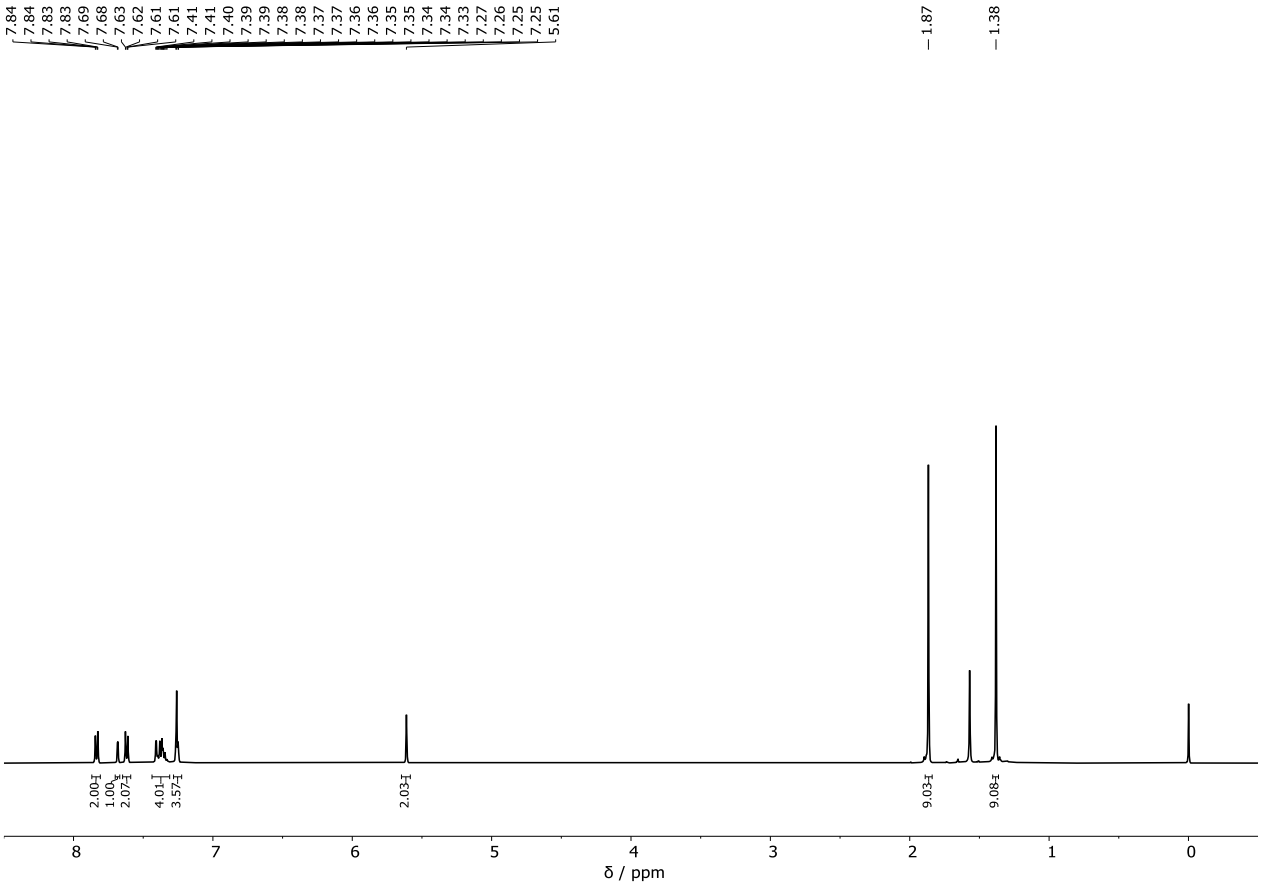

Supplementary Fig. 14. ^{1}H NMR spectrum of **[R2][PF$_6$]** (Chloroform-*d*, 298 K, 500 MHz).

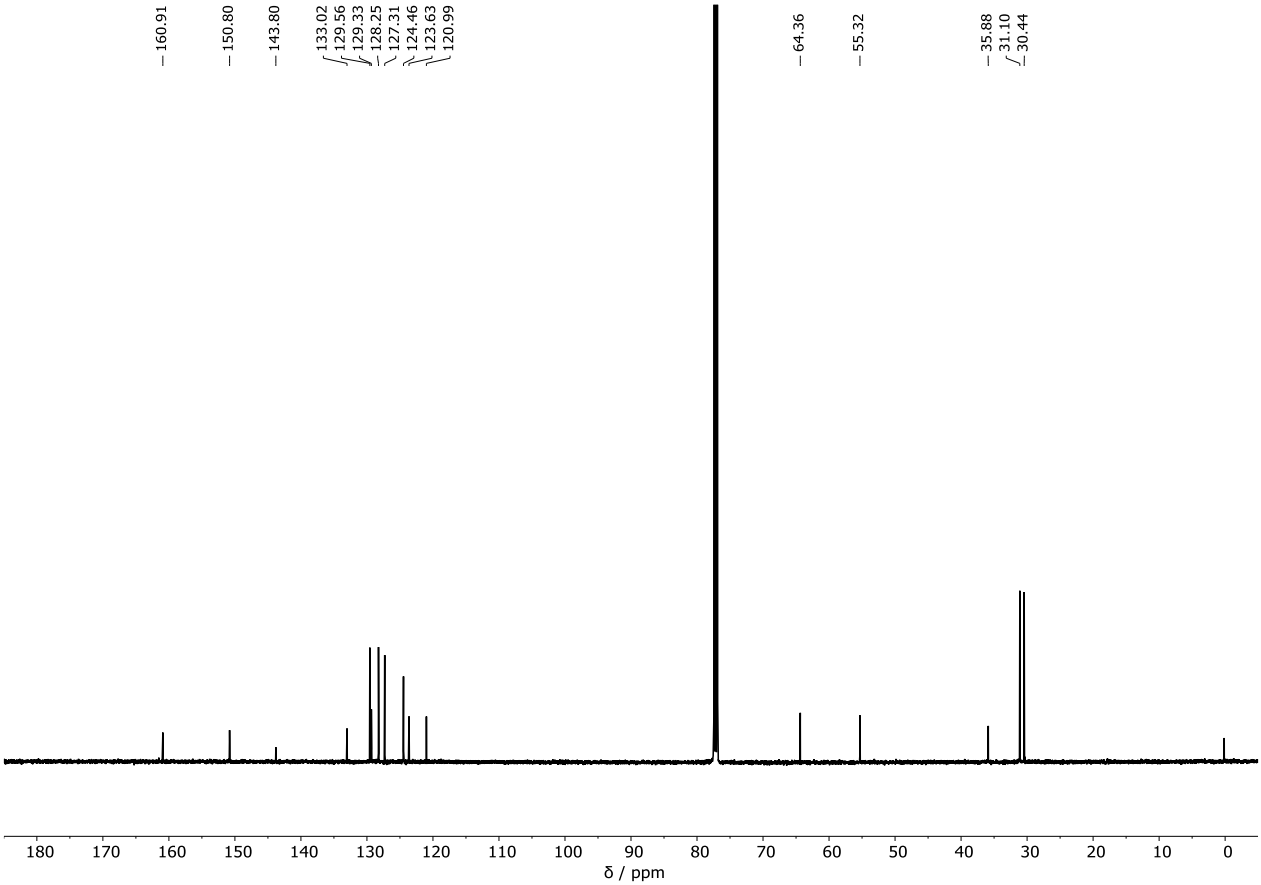

Supplementary Fig. 15. ^{13}C NMR spectrum of **[R2][PF$_6$]** (Chloroform-*d*, 298 K, 126 MHz).

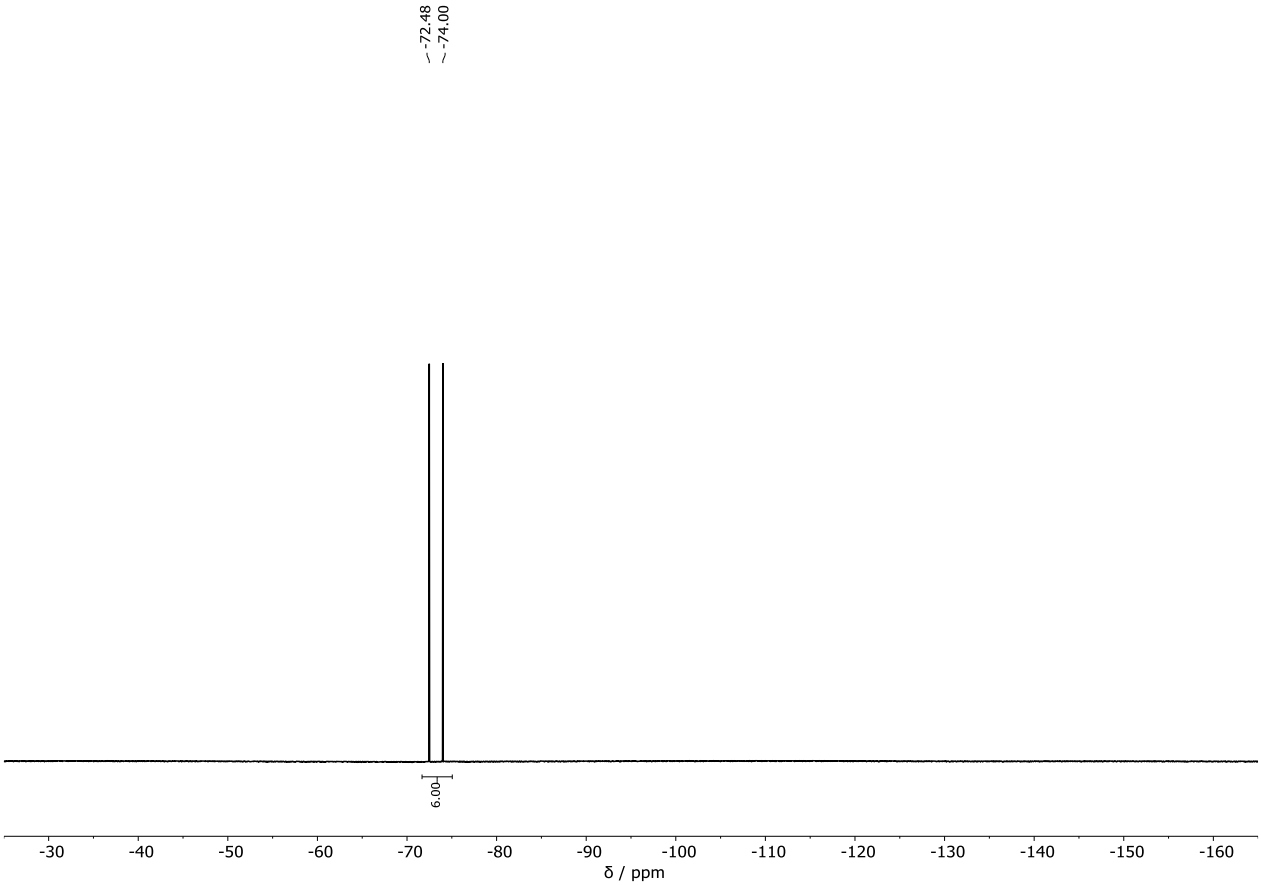

Supplementary Fig. 16. ^{19}F NMR spectrum of **[R2][PF_6]** (Chloroform-*d*, 298 K, 470 MHz).

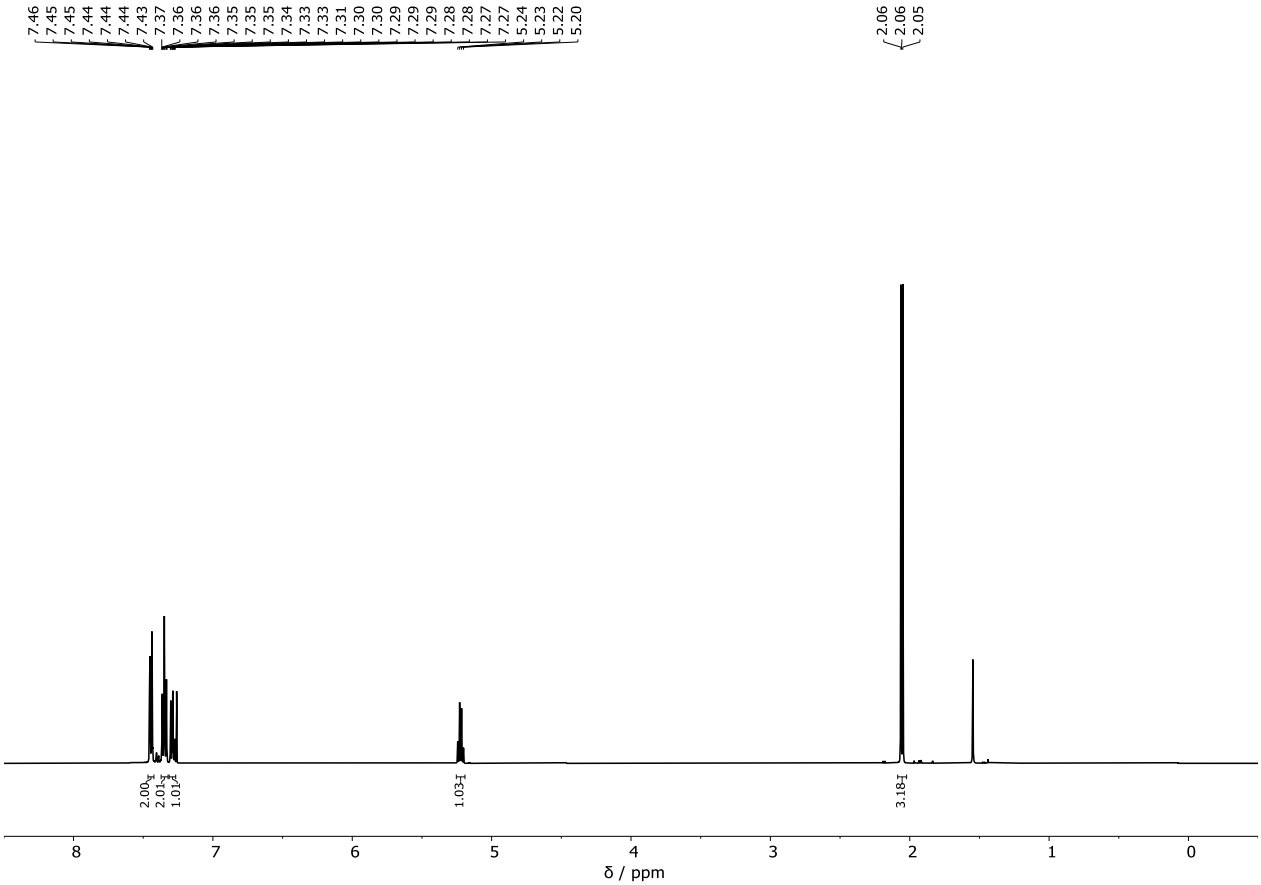

Supplementary Fig. 17. ^{1}H NMR spectrum of **5** (Chloroform-*d*, 298 K, 500 MHz).

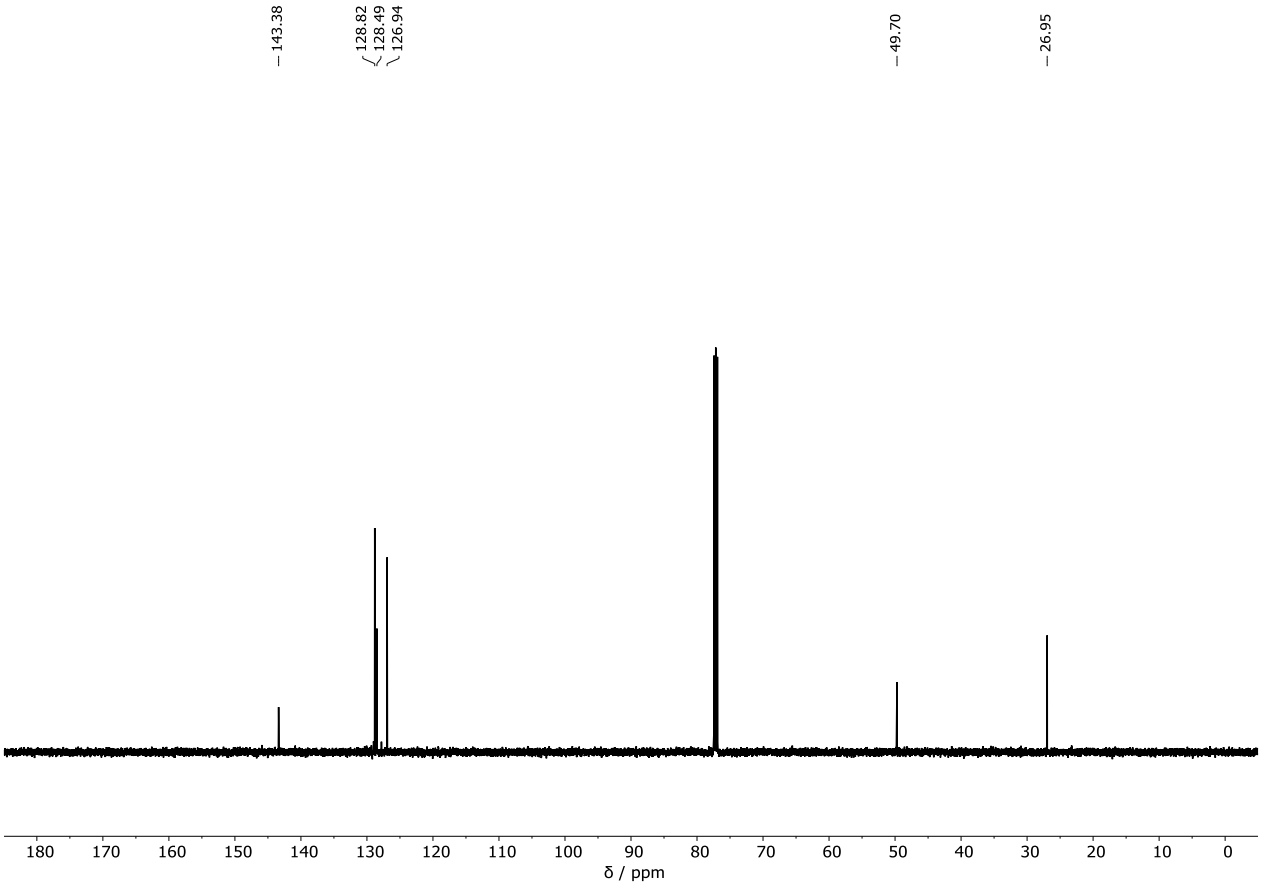

Supplementary Fig. 18. ^{13}C NMR spectrum of **5** (Chloroform-*d*, 298 K, 126 MHz).

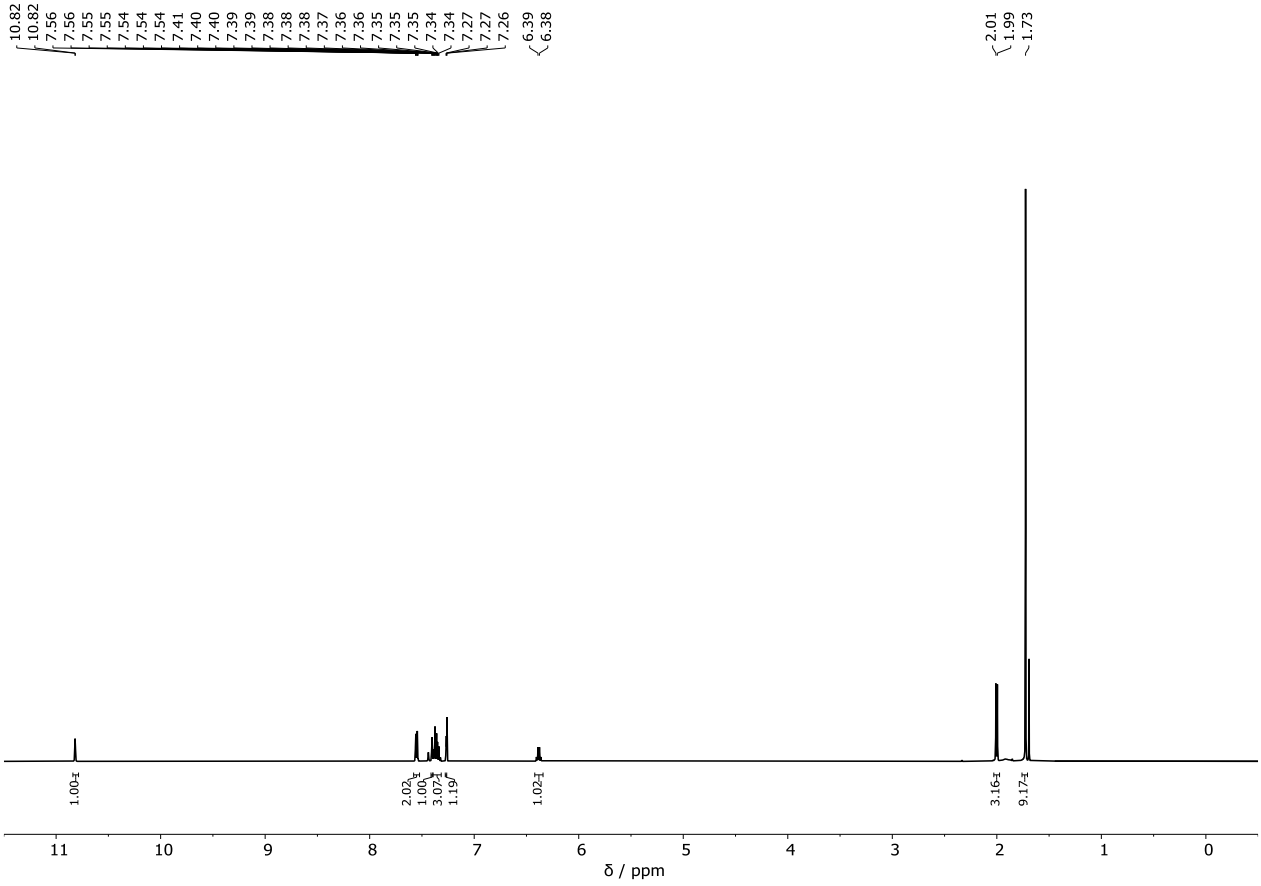

Supplementary Fig. 19. ^{1}H NMR spectrum of **6** (Chloroform-*d*, 298 K, 500 MHz).

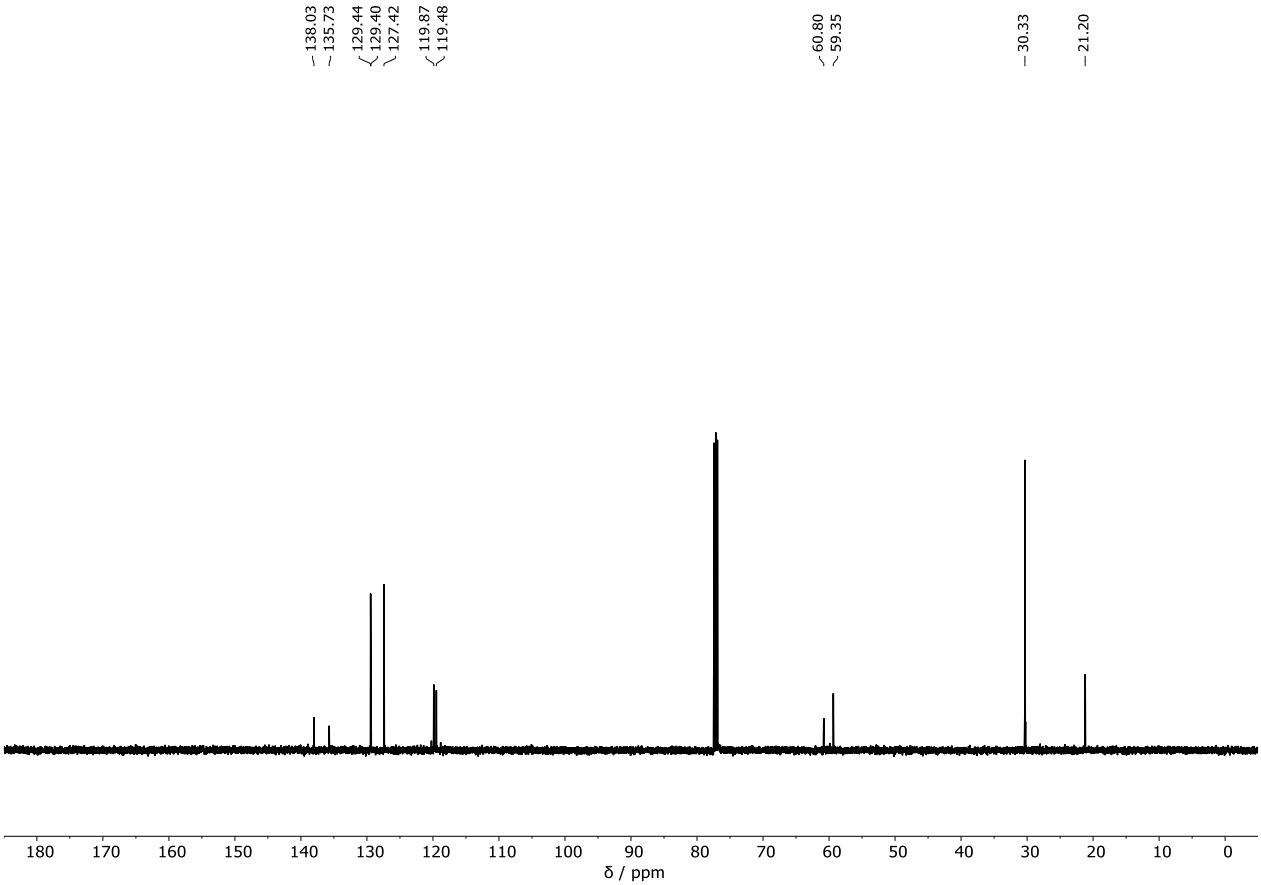

Supplementary Fig. 20. ^{13}C NMR spectrum of **6** (Chloroform-*d*, 298 K, 126 MHz).

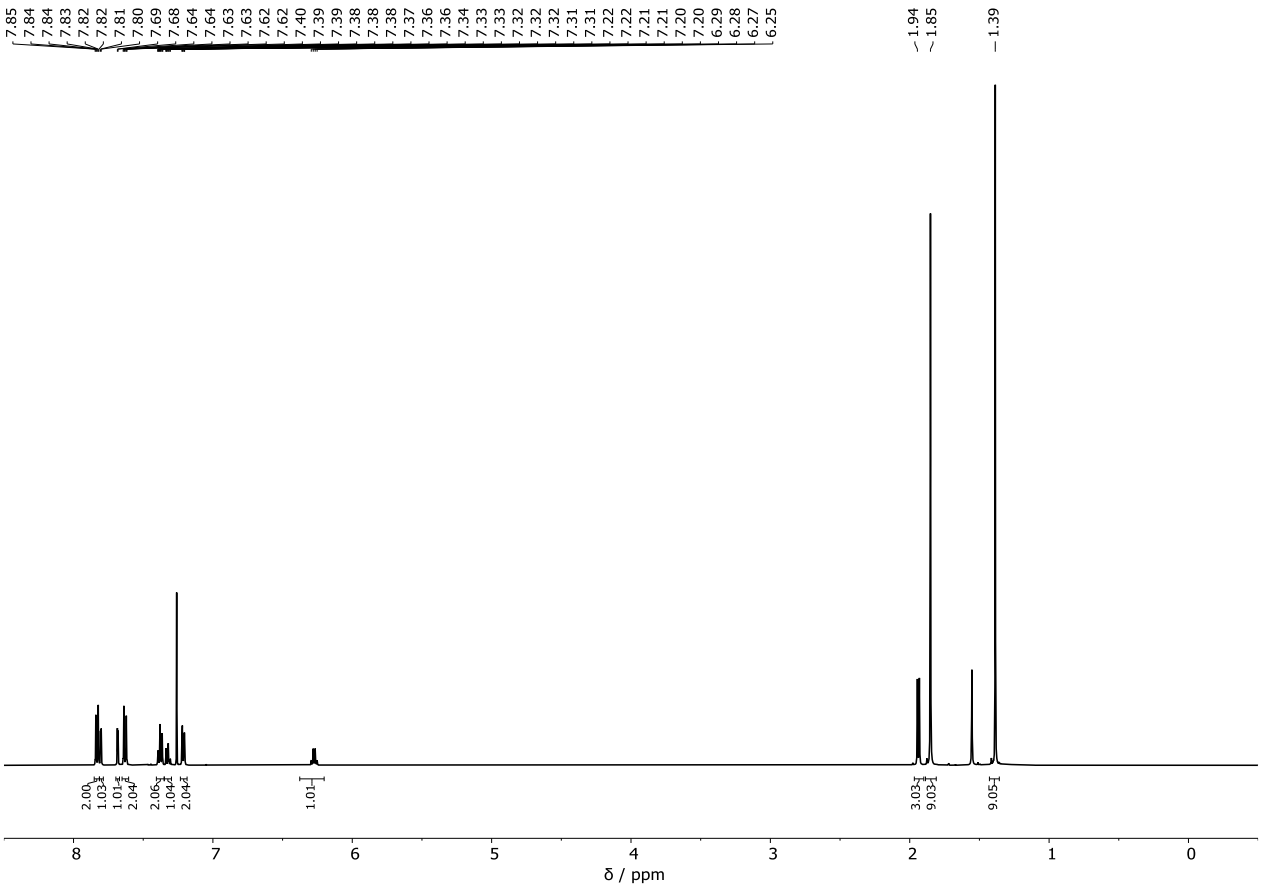

Supplementary Fig. 21. ^{1}H NMR spectrum of **[R3][PF$_6$]** (Chloroform-*d*, 298 K, 500 MHz).

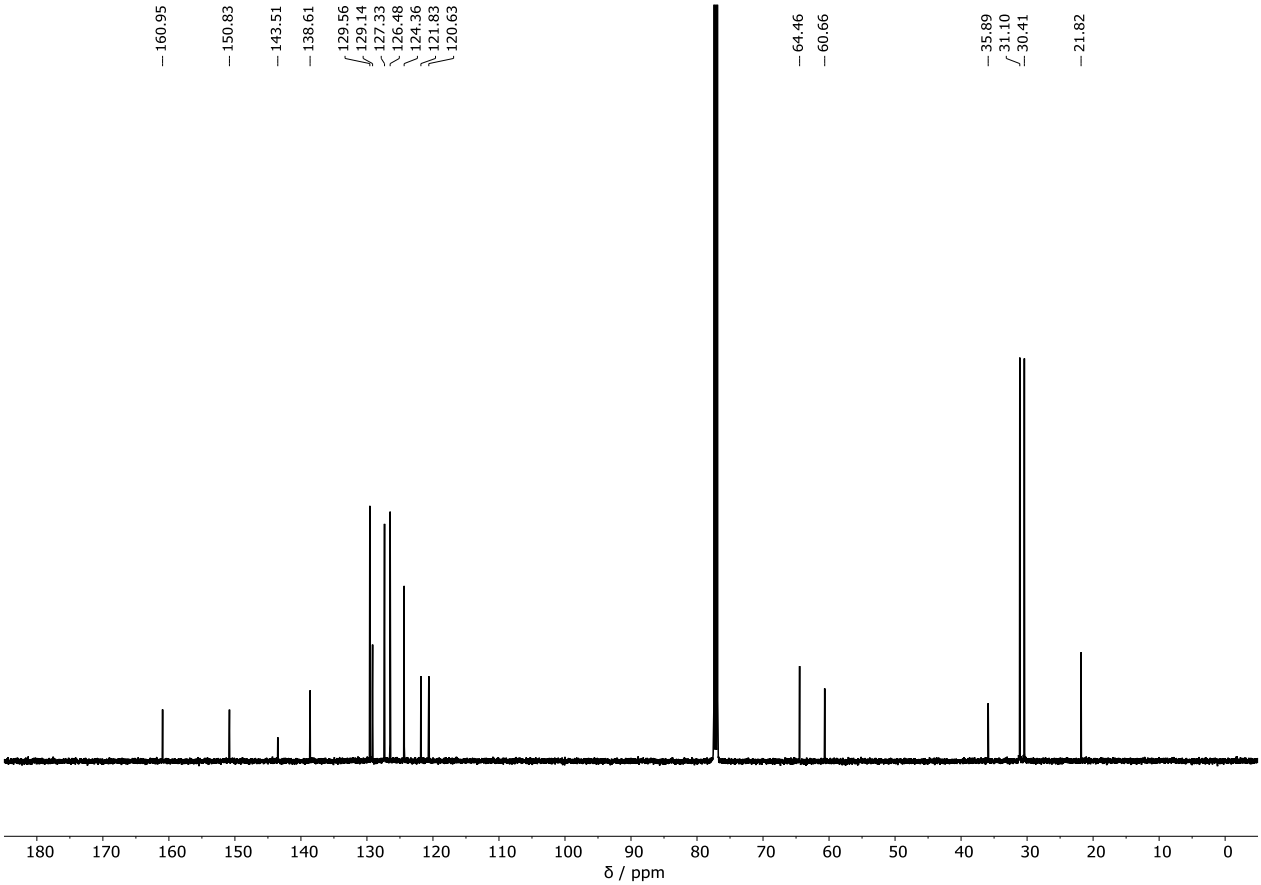

Supplementary Fig. 22. ^{13}C NMR spectrum of **[R3][PF$_6$]** (Chloroform-*d*, 298 K, 126 MHz).

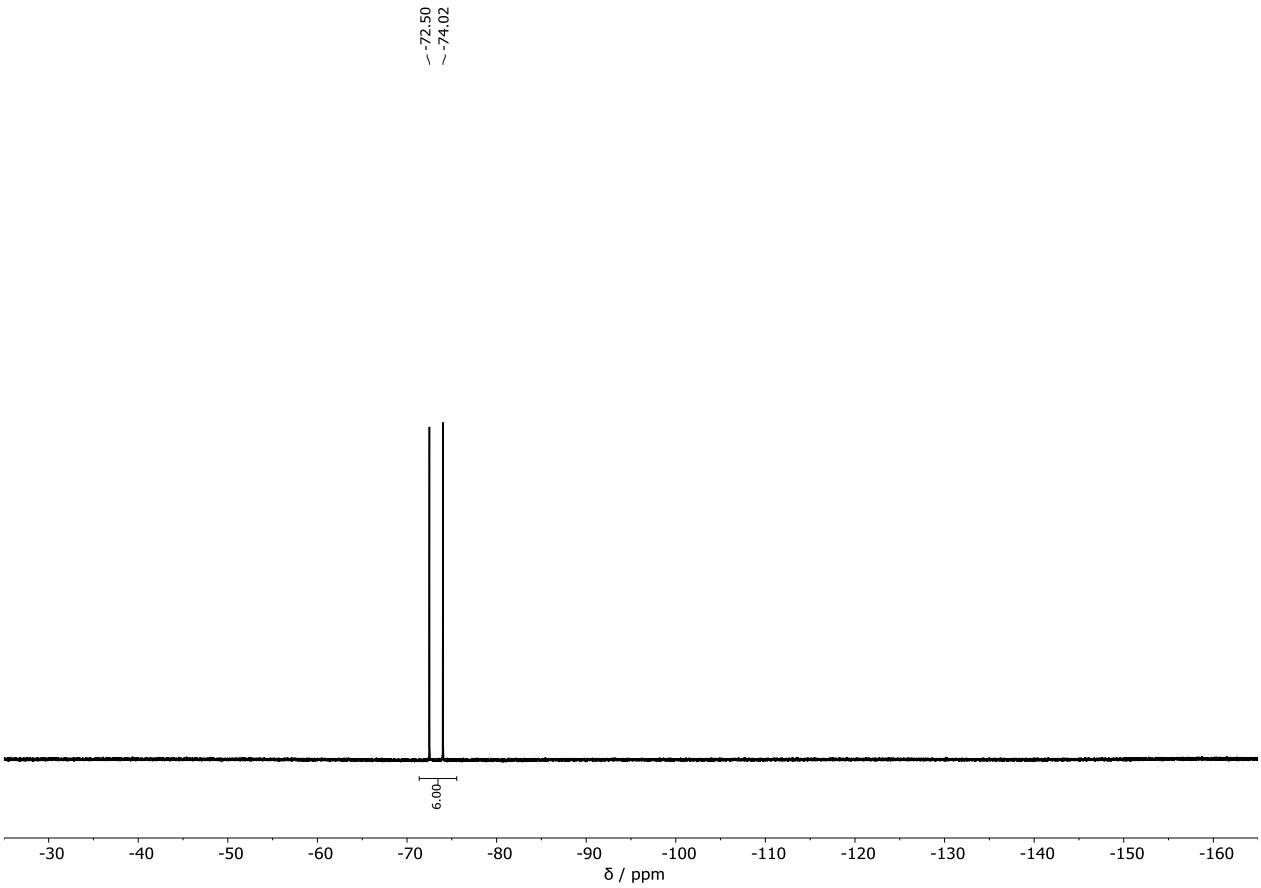

Supplementary Fig. 23. ^{19}F NMR spectrum of **[R3][PF$_6$]** (Chloroform-*d*, 298 K, 470 MHz).

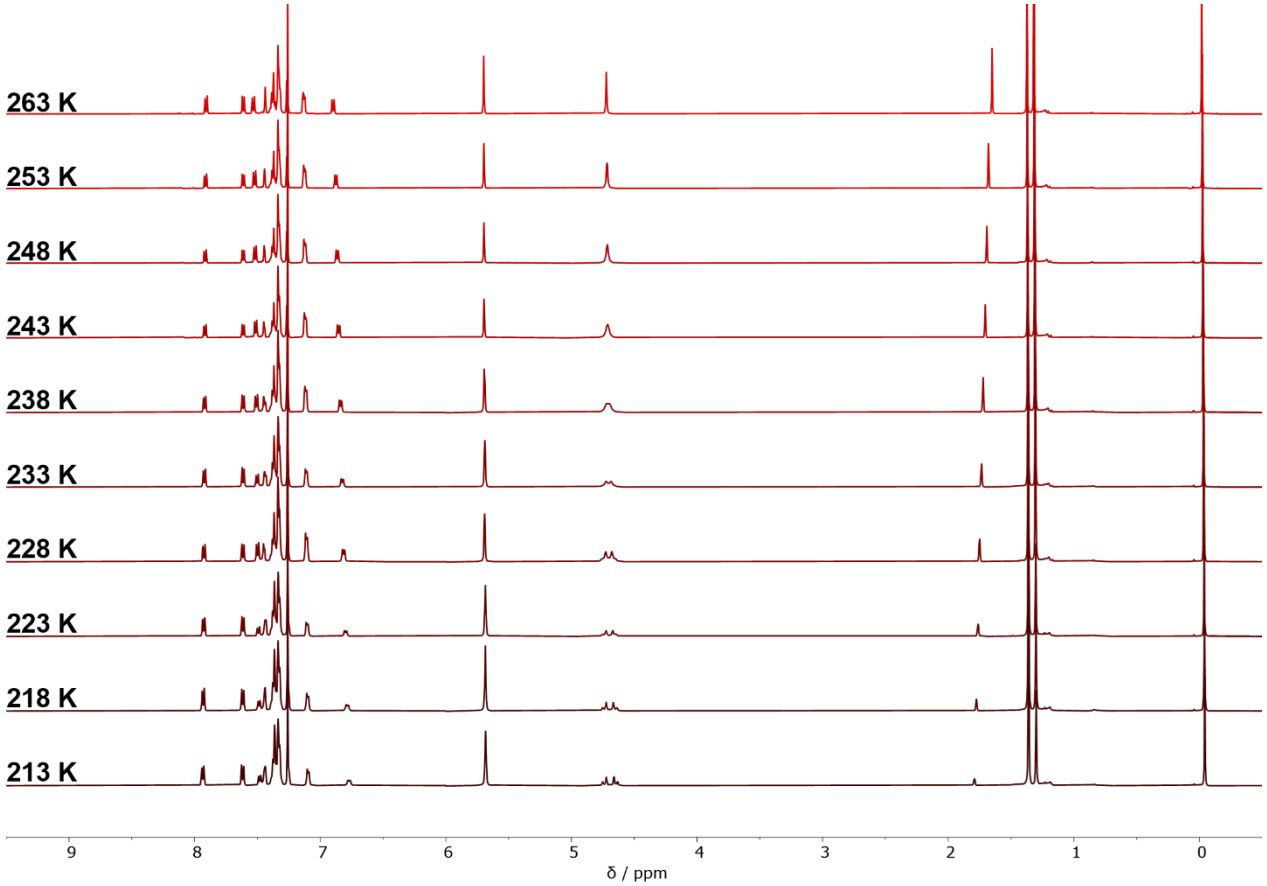

Supplementary Fig. 24. Variable-temperature ^{1}H NMR spectra of a solution of **[R1][PF$_6$]** irradiated at 365 nm at the PSS; C_{R1} = 3.0×10^{-3} M, Chloroform-*d*, 500 MHz.

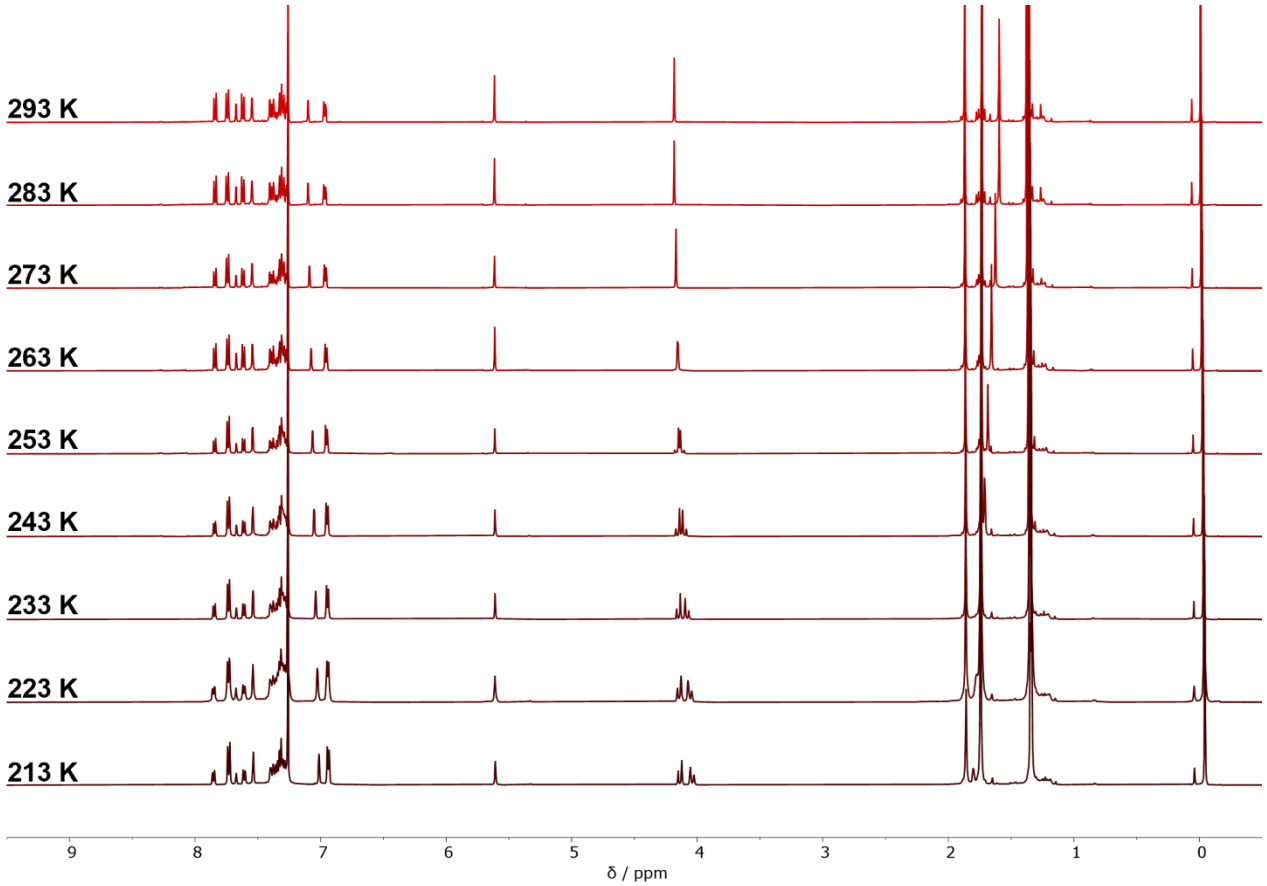

Supplementary Fig. 25. Variable-temperature ^{1}H NMR spectra of a solution of **[R2][PF$_6$]** irradiated at 365 nm at the PSS; C_{R2} = 3.0×10^{-3} M, Chloroform-*d*, 500 MHz.

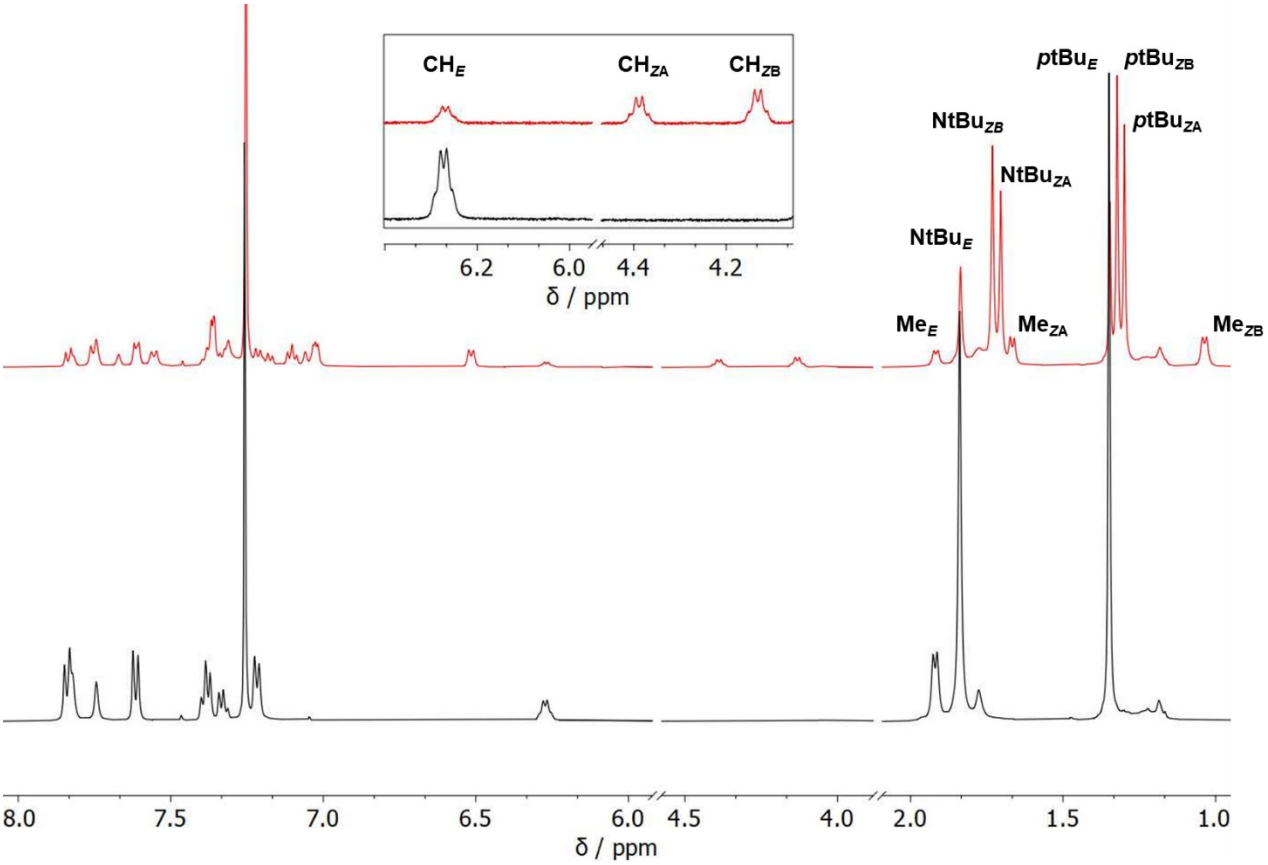

Supplementary Fig. 26. ^{1}H NMR spectrum of **[R3][PF$_6$]** (black trace) and of the PSS mixture obtained upon in situ irradiation at 365 nm (red trace); the inset highlights the quartets related to the benzylic CH proton of the three isomers; 218 K, C_{R3} = 1.0 ×10^{-2} M, Chloroform-*d*, 500 MHz.

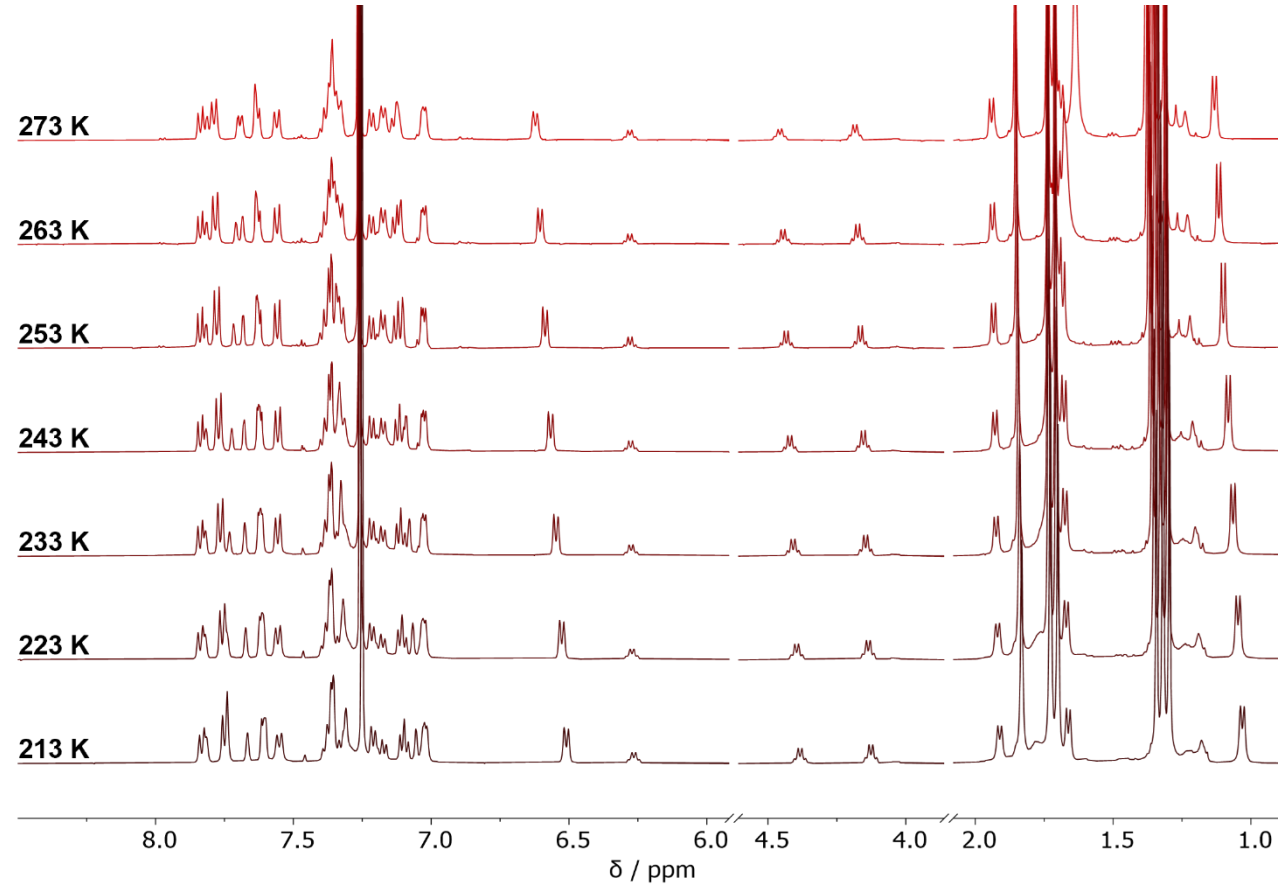

Supplementary Fig. 27. Variable-temperature ^{1}H NMR spectra of a solution of **[R3][PF$_6$]** irradiated at 365 nm at the PSS; C_{R3} = 1.0×10^{-2} M, Chloroform-*d*, 500 MHz.

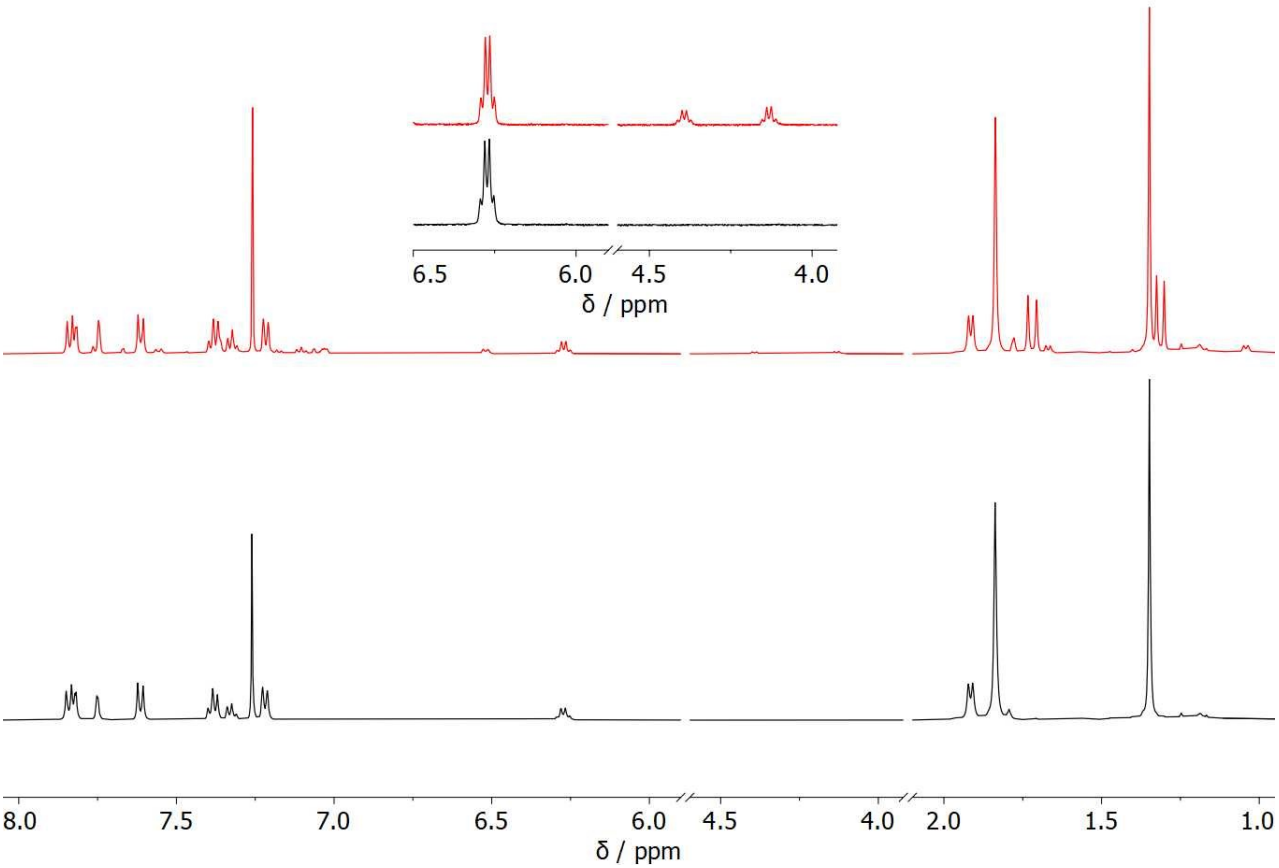

Supplementary Fig. 28. ^{1}H NMR spectrum of **[R3][PF$_6$]** (black trace) and of the PSS mixture obtained upon in situ irradiation at 453 nm (red trace); the inset highlights the quartets related to the benzylic CH proton of the three isomers; 218 K, C_{R3} = 1.0×10^{-2} M, Chloroform-*d*, 500 MHz.

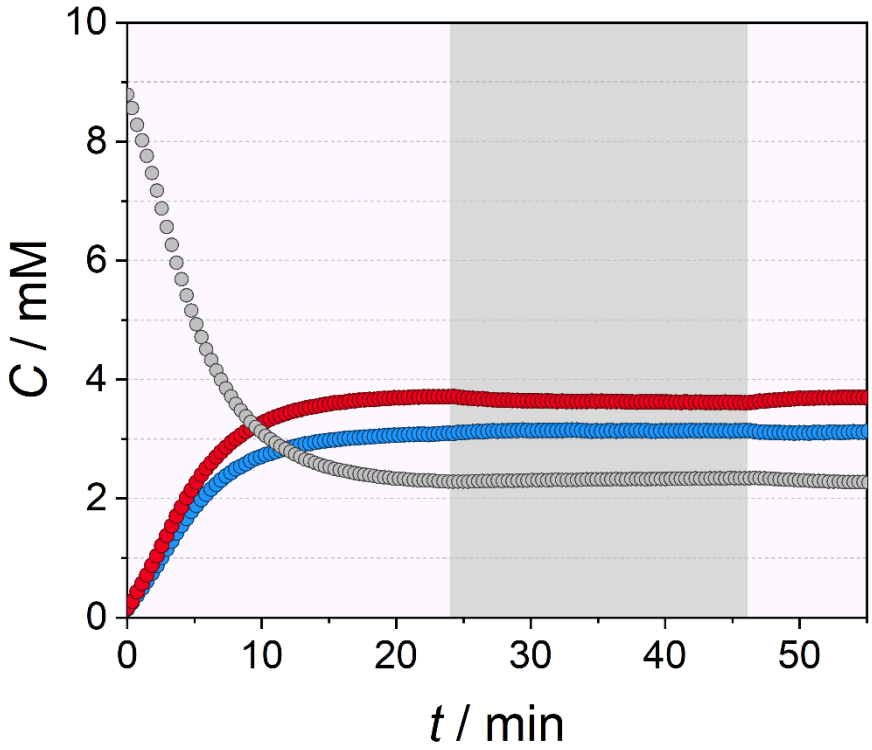

Supplementary Fig. 29. Experimental variations in concentration of [*E*-**R3**]$^+$ (grey dots), [Z_A-**R3**]$^+$ (blue dots) and [Z_B-**R3**]$^+$ (red dots) upon irradiation at 365 nm (violet background) or in the dark (grey background); 218 K, C_{R3} = 1.0×10^{-2} M, Chloroform-*d*, 500 MHz.

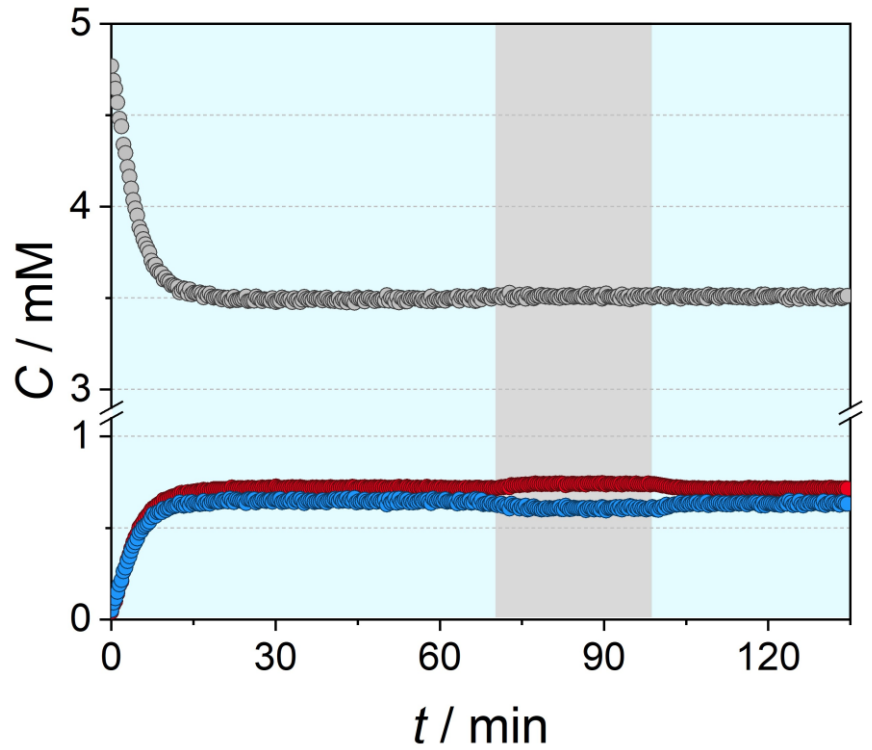

Supplementary Fig. 30. Experimental variations in concentration of [*E*-**R3**]$^+$ (grey dots), [Z_A-**R3**]$^+$ (blue dots) and [Z_B-**R3**]$^+$ (red dots) upon irradiation at 453 nm (cyan background) or in the dark (grey background); 218 K, C_{R3} = 4.8×10^{-3} M, Chloroform-*d*, 500 MHz.

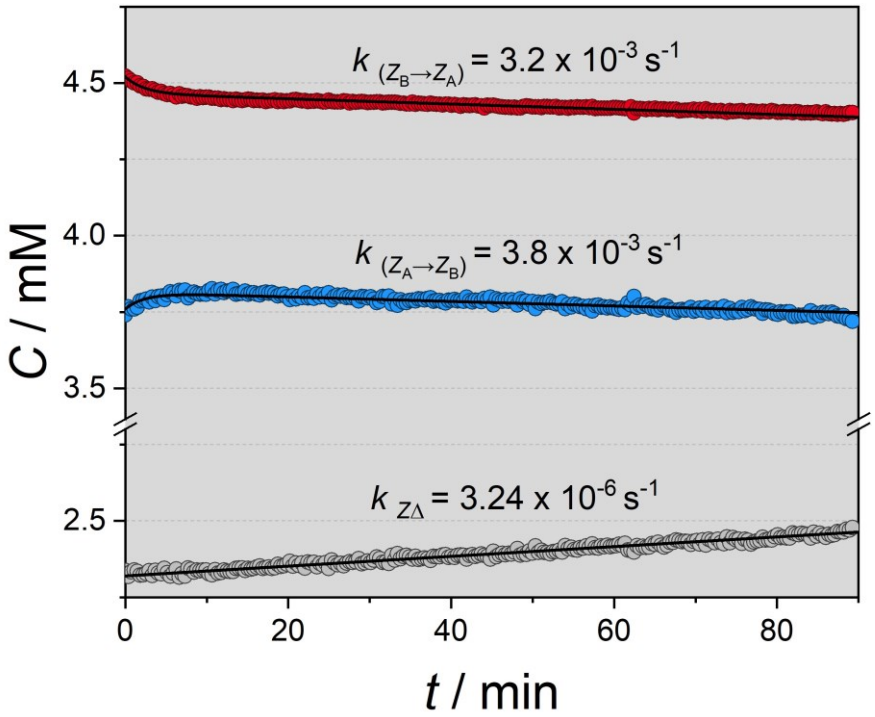

Supplementary Fig. 31. Experimental variations in concentration of the PSS_{365} mixture of [*E*-**R3**]$^+$ (grey dots), [Z_A-**R3**]$^+$ (blue dots) and [Z_B-**R3**]$^+$ (red dots) in the dark, and data fitting (black traces) to obtain the kinetic constants relative to the thermal equilibration ($Z_A \rightleftarrows Z_B$) and total thermal back-isomerization ($Z_A \rightarrow E$ and $Z_B \rightarrow E$) processes; 218 K, C_{R3} = 1.0×10^{-2} M, Chloroform-*d*, 500 MHz.

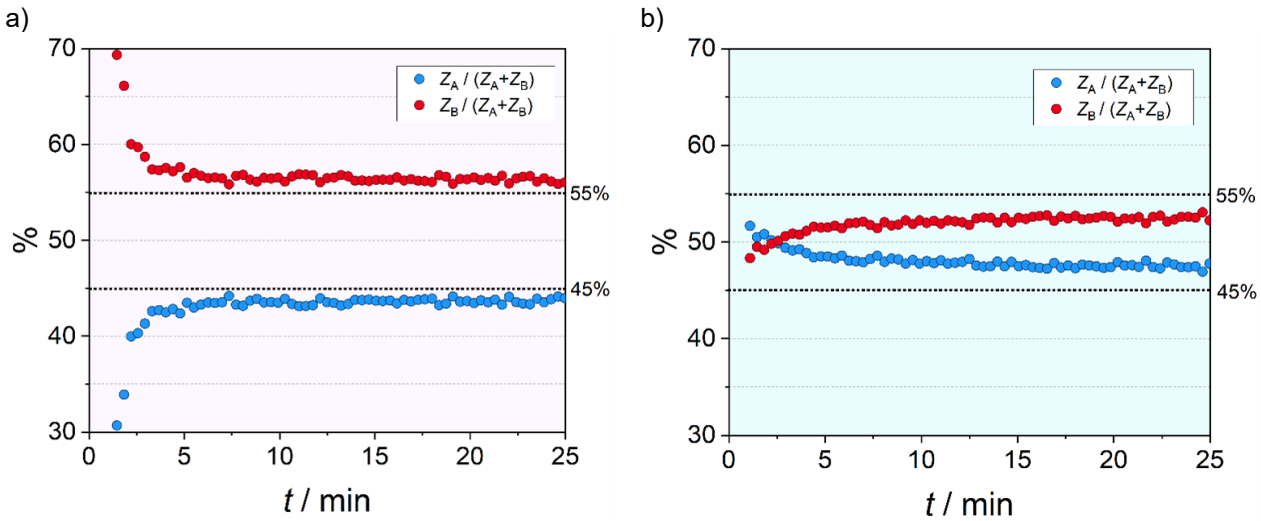

Supplementary Fig. 32. Percentage composition over time ([Z_A-**R3**]$^+$, blue dots; [Z_B-**R3**]$^+$, red dots) of an [*E*-**R3**]$^+$ solution upon irradiation at 365 nm (a) or 453 nm (b); C_{R3} = 1.0×10^{-2} M (a) or 4.8×10^{-3} M (b), $CDCl_3$, 218 K.

4. Spectrophotometric data

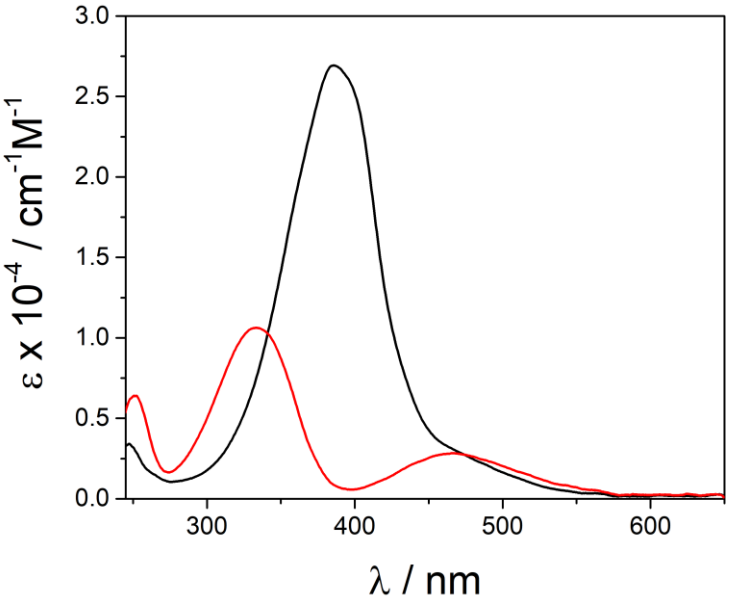

Supplementary Fig. 33. Absorption spectra of [*E*-**R1**][PF_6] (black trace) and [*Z*-**R1**][PF_6] (red trace); 298 K, $CHCl_3$.

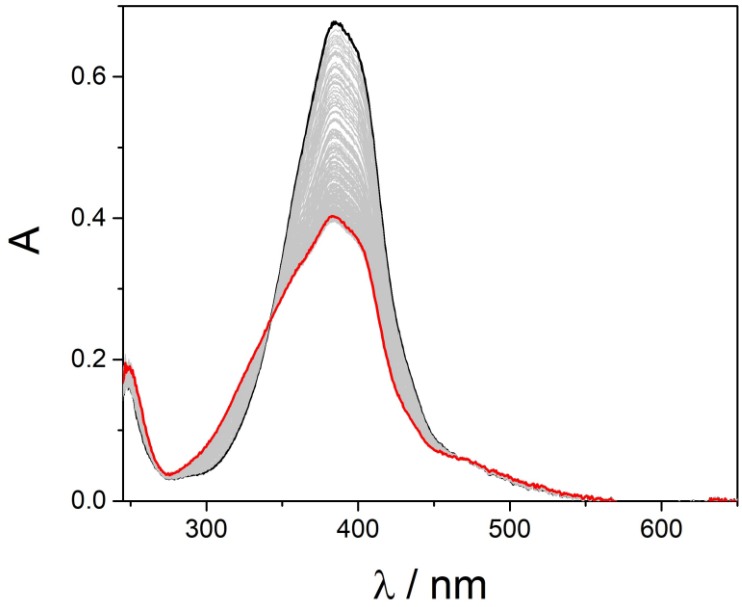

Supplementary Fig. 34. Absorption variations of [*E*-**R1**][PF_6] (black trace) upon irradiation at 365 nm until PSS (red trace); $C_{\mathbf{R1}}$ = 2.6×10^{-5} M, 298 K, $CHCl_3$.

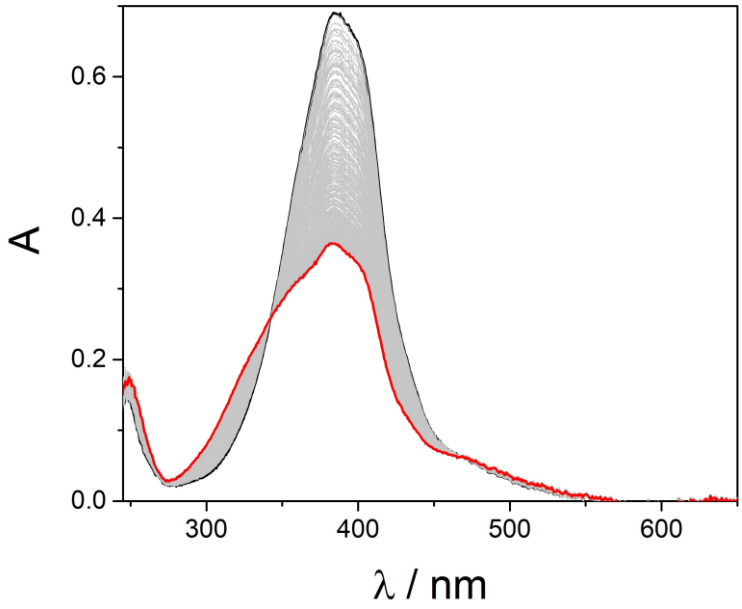

Supplementary Fig. 35. Absorption variations of [*E*-**R1**][PF_6] (black trace) upon irradiation at 436 nm until PSS (red trace); $C_{\mathbf{R1}}$ = 2.6×10^{-5} M, 298 K, $CHCl_3$.

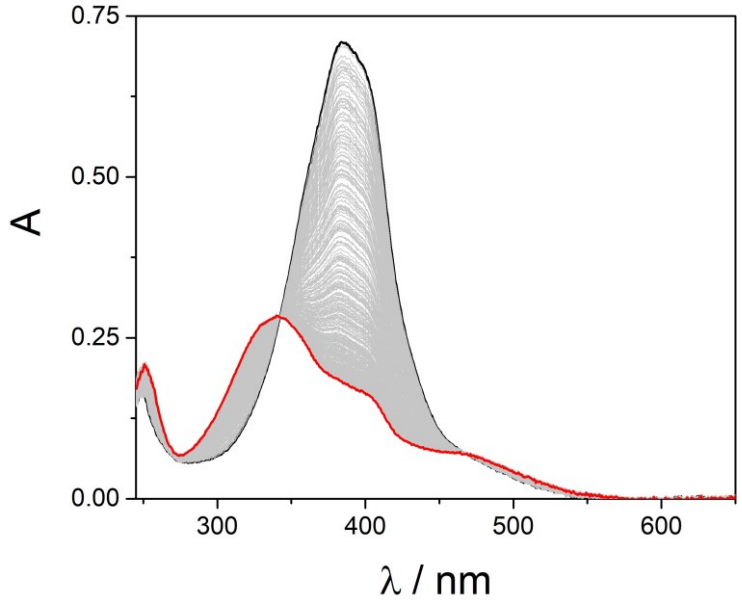

Supplementary Fig. 36. Absorption variations of [*E*-**R1**][PF_6] (black trace) upon irradiation at 405 nm until PSS (red trace); $C_{\mathbf{R1}}$ = 2.6×10^{-5} M, 298 K, $CHCl_3$.

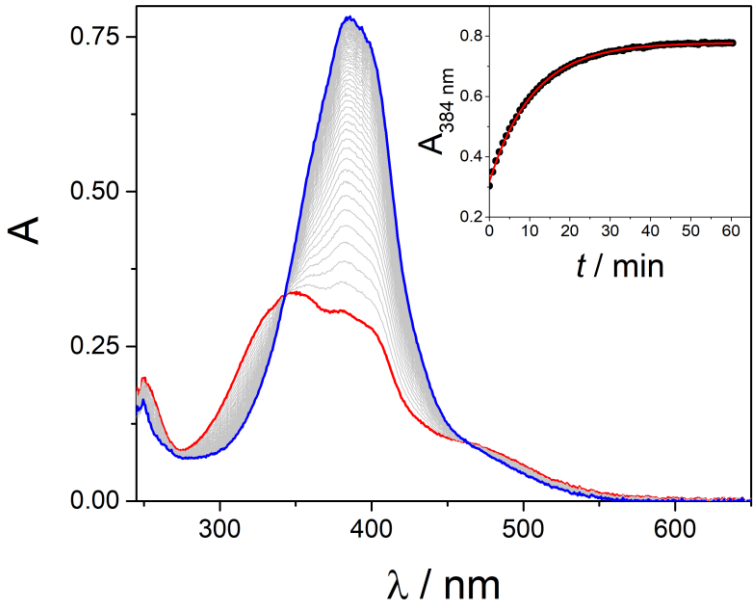

Supplementary Fig. 37. Absorption variations of [*Z*-**R1**][PF_6] (red trace) upon thermal back-isomerization in the dark (grey traces) until total recovery of [*E*-**R1**][PF_6] (blue trace); insert: absorption changes at 384 nm (black dots) together with data fitting (red trace); $C_{\mathbf{R1}}$ = 2.6×10^{-5} M, 298 K, $CHCl_3$.

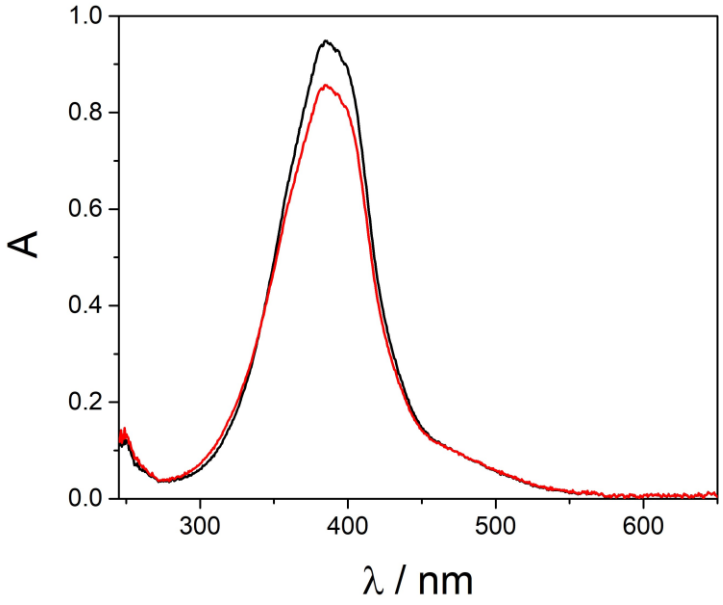

Supplementary Fig. 38. Absorption variations of [*E*-**R1**][PF_6] (black trace) upon irradiation at 546 nm until PSS (red trace); $C_{\mathbf{R1}}$ = 3.5×10^{-5} M, 298 K, $CHCl_3$.

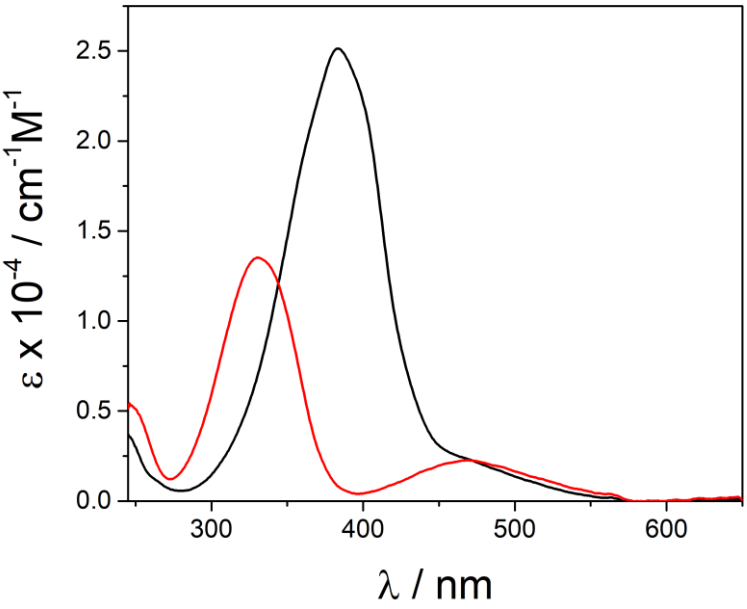

Supplementary Fig. 39. Absorption spectra of [*E*-**R2**][PF_6] (black trace) and [*Z*-**R2**][PF_6] (red trace); 298 K, $CHCl_3$.

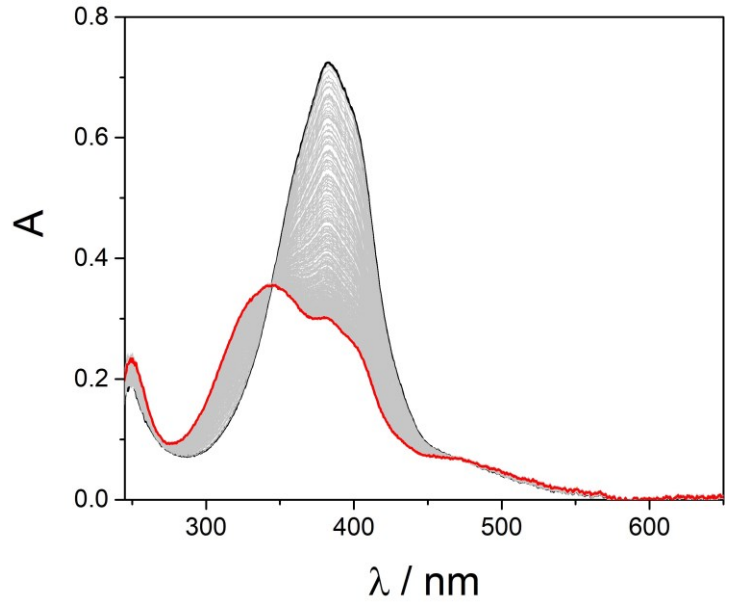

Supplementary Fig. 40. Absorption variations of [*E*-**R2**][PF_6] (black trace) upon irradiation at 365 nm until PSS (red trace); $C_{\mathbf{R2}} = 3.3\times10^{-5}$ M, 298 K, $CHCl_3$.

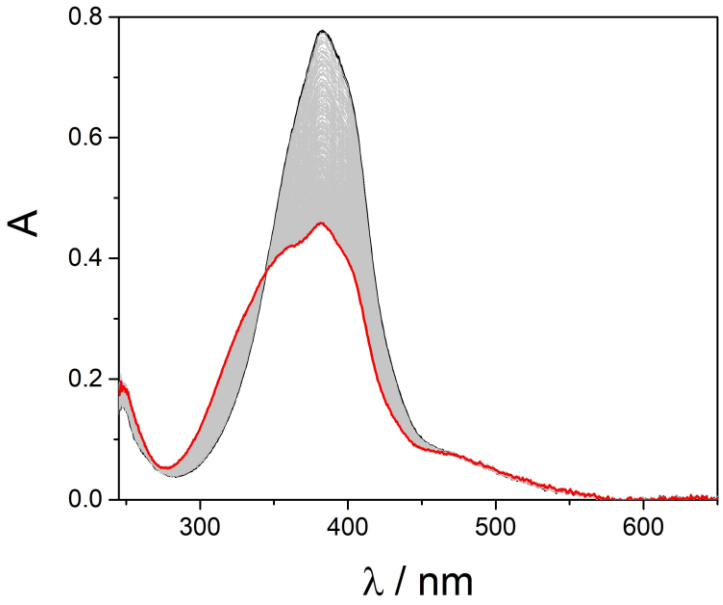

Supplementary Fig. 41. Absorption variations of [*E*-**R2**][PF_6] (black trace) upon irradiation at 436 nm until PSS (red trace); C_{R2} = 3.3×10^{-5} M, 298 K, $CHCl_3$.

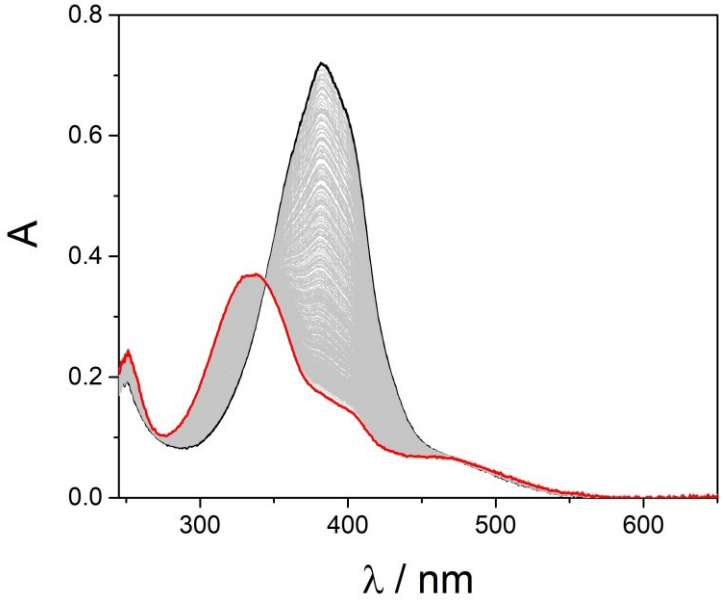

Supplementary Fig. 42. Absorption variations of [*E*-**R2**][PF_6] (black trace) upon irradiation at 405 nm until PSS (red trace); C_{R2} = 3.3×10^{-5} M, 298 K, $CHCl_3$.

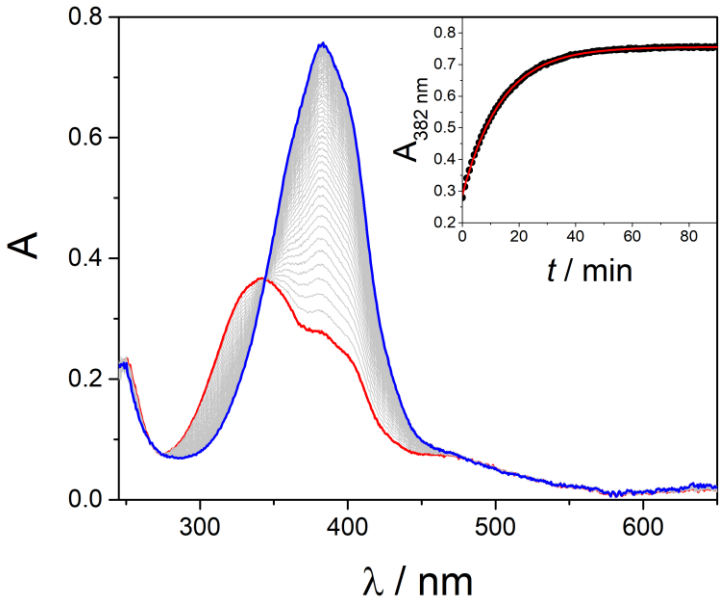

Supplementary Fig. 43. Absorption variations of [*Z*-**R2**][PF_6] (red trace) upon thermal back-isomerization in the dark (grey traces) until total recovery of [*E*-**R2**][PF_6] (blue trace); inset: absorption changes at 382 nm (black dots) together with data fitting (red trace); $C_{\mathbf{R2}}$ = 3.3×10^{-5} M, 298 K, $CHCl_3$.

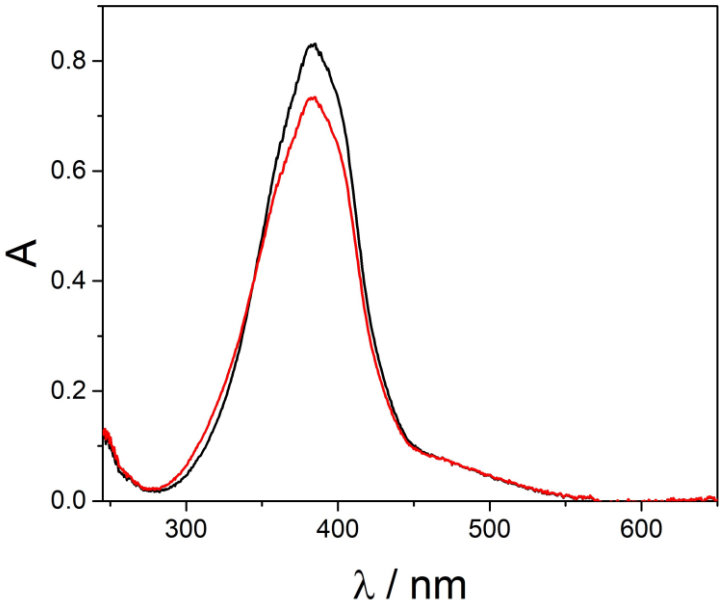

Supplementary Fig. 44. Absorption spectra of [*E*-**R2**][PF_6] (black trace) and of the mixture obtained upon irradiation at 546 nm until PSS (red trace); $C_{\mathbf{R2}}$ = 3.3×10^{-5} M, 298 K, $CHCl_3$.

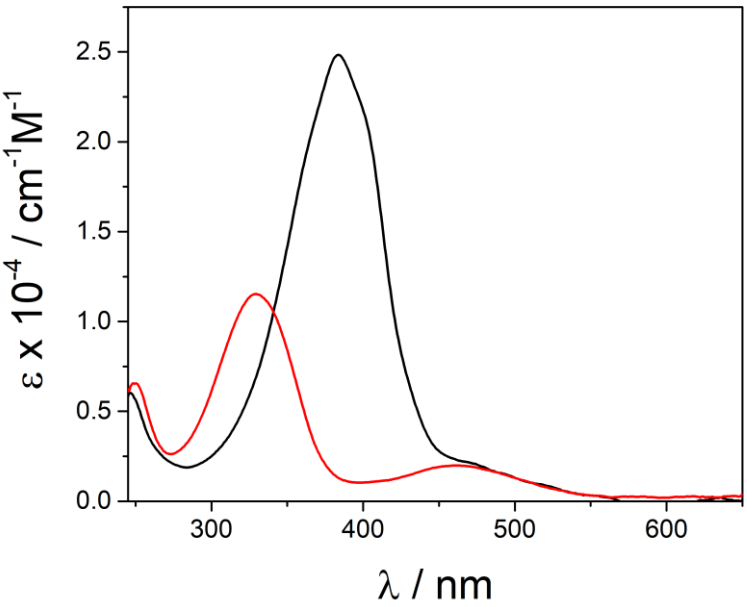

Supplementary Fig. 45. Absorption spectra of [*E*-**R3**][PF_6] (black trace) and [*Z*-**R3**][PF_6] (red trace); 298 K, $CHCl_3$.

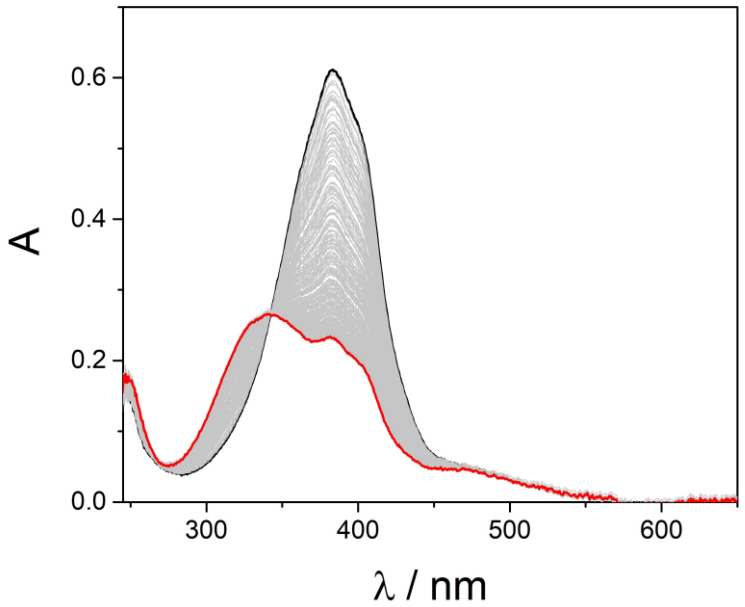

Supplementary Fig. 46. Absorption variations of [*E*-**R3**][PF_6] (black trace) upon irradiation at 365 nm until PSS (red trace); $C_{\mathbf{R3}} = 2.4\times10^{-5}$ M, 298 K, $CHCl_3$.

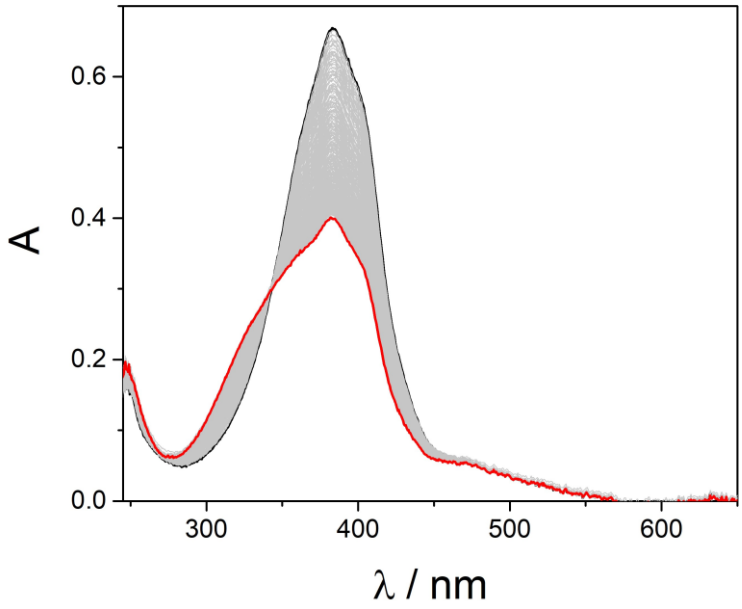

Supplementary Fig. 47. Absorption variations of [*E*-**R3**][PF_6] (black trace) upon irradiation at 436 nm until PSS (red trace); $C_{\mathbf{R3}}$ = 2.4×10^{-5} M, 298 K, $CHCl_3$.

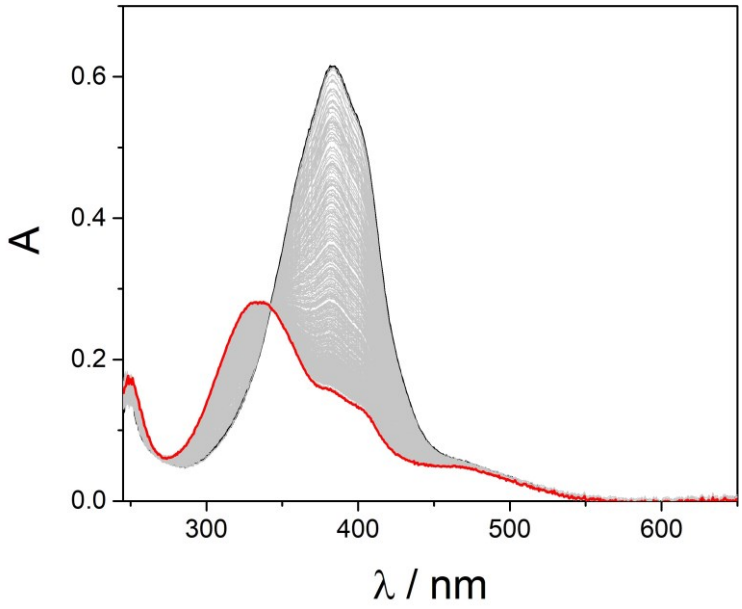

Supplementary Fig. 48. Absorption variations of [*E*-**R3**][PF_6] (black trace) upon irradiation at 405 nm until PSS (red trace); $C_{\mathbf{R3}}$ = 2.4×10^{-5} M, 298 K, $CHCl_3$.

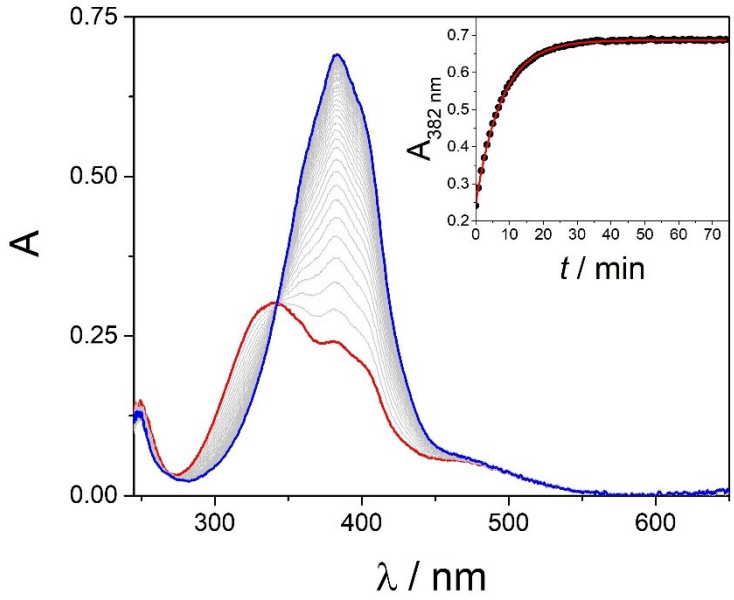

Supplementary Fig. 49. Absorption variations of [*Z*-**R3**][PF_6] (red trace) upon thermal back-isomerization in the dark (grey traces) until total recovery of [*E*-**R3**][PF_6] (blue trace); inset: absorption changes at 382 nm (black dots) together with data fitting (red trace); $C_{\mathbf{R3}}$ = 2.4×10^{-5} M, 298 K, $CHCl_3$.

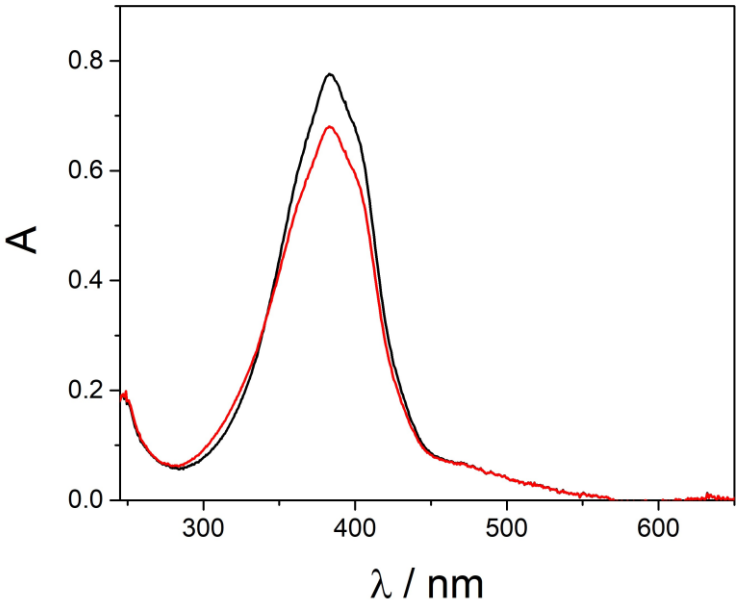

Supplementary Fig. 50. Absorption variations of [*E*-**R3**][PF_6] (black trace) upon irradiation at 546 nm until PSS (red trace); $C_{\mathbf{R3}}$ = 3.1×10^{-5} M, 298 K, $CHCl_3$.

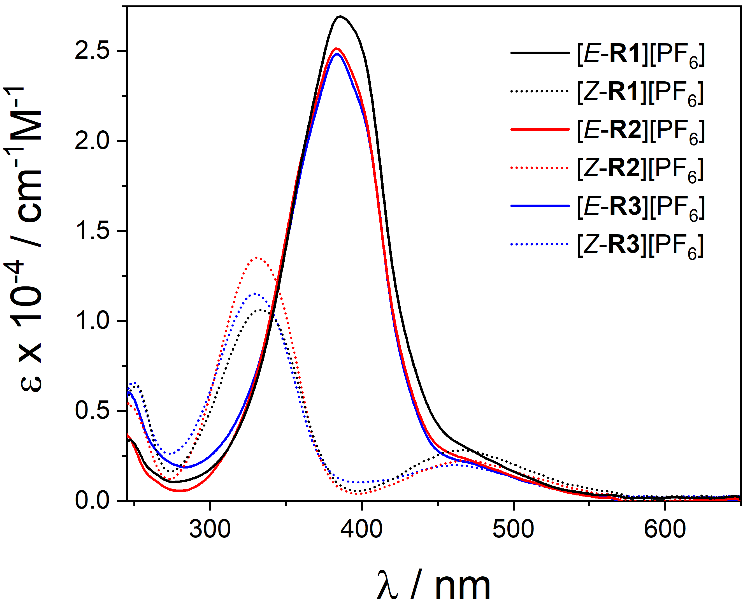

Supplementary Fig. 51. Experimental absorption spectra of the *E*-isomers (solid traces) and calculated absorption spectra of the *Z*-isomers (dotted traces) of the studied azoimidazolium compounds [**R1**][PF_6], [**R2**][PF_6] and [**R3**][PF_6]; 298 K, $CHCl_3$.

Supplementary Table 1. Photochemical properties, composition of the photostationary state and rates of back-isomerization for the three photochromes [**R1**][PF_6], [**R2**][PF_6] and [**R3**][PF_6]; 298 K, $CHCl_3$.

Compound	**Absorption**		**Isomerization**			
	λ_{max} / nm	**ε / $cm^{-1}M^{-1}$**	**λ_{irr} / nm**	**$\Phi_{E\rightarrow Z}$**	***Z* : *E* PSS, %**	**$k_{Z\Delta}$ / s^{-1}**
[**R1**][PF_6]	384	27000	365	0.17	42 : 58	1.5×10^{-3}
	474	2400	405	0.31	78 : 22	
			436	0.36	44 : 56	
			546	–*	10 : 90	
[**R2**][PF_6]	382	25300	365	0.22	65 : 35	1.2×10^{-3}
	470	2400	405	0.30	80 : 20	
			436	0.29	48 : 52	
			546	–*	12 : 88	
[**R3**][PF_6]	382	25000	365	0.24	65 : 35	2.2×10^{-3}
	470	2300	405	0.27	80 : 20	
			436	0.33	43 : 57	
			546	–*	13 : 87	

* the quantum yields of photoisomerization at this wavelength were not calculated.

5. Computational details

Results obtained in gas phase corresponded qualitatively to the ones obtained in PCM: we will only refer to the latter ones unless stated otherwise. For clarity, in the following paragraph the isomers of cation [**R3**]$^+$ will be referred to as Z_A, Z_B and E.

DFT calculations

Two types of coordinate scans were performed: geometry optimizations with constraints applied to one single coordinate (single scan) or applied to two coordinates at the same time (double scan).The coordinates of interest are the ones majorly involved in the isomerization mechanisms between Z_A and Z_B (Σ, Ψ) and between E and the Z isomers (Ω, α, β) as shown in Figure 4a of the manuscript. Each single scan generated a sequence of 24 geometries with steps of 15° for the inspected dihedral angle (Σ, Ψ, Ω). The generation of the single geometries was performed through a progressive refinement of optimizations, starting with a lighter basis set (3-21G), then employing cc-pVDZ basis set. The energies and geometries were ultimately refined with aug-cc-pVDZ basis set in gas phase and in chloroform.

Looking at the energy profile obtained from the single scan of the dihedral angle Σ (Supplementary Fig. 54) we can assess the presence of two minima corresponding to the position of the rotor group on the side of the two faces of the imidazolium plane: the structures centered at 225° and 135° would correspond respectively to Z_A and Z_B basins. A single scan of Ψ dihedral was performed on both structures to investigate the relevance of a possible gearing effect of the benzylic group. Indeed, the results (Supplementary Fig. 55) showed the presence of at least three low energy regions in function of Ψ for both Z_A and Z_B conformers. This double dependence of the geometrical stability on the Σ / Ψ dihedrals was further assessed in gas phase through a double scan of these two coordinates constrained in regions corresponding to the minima observed in the single scans (Σ: [90° - 150°], [210° - 285°], Ψ:[60° - 150°], [240° - 375°]) containing 170 geometries. Furthermore, the whole double conformational space was explored in chloroform with the Polarizable Continuum Model (PCM) for a total of 576 geometries. The resulting potential energy maps (Supplementary Fig. 57) highlight a slightly higher stability of Z_A diastereomer, however, we must consider that in this map the zero-point energy and vibrational contributions are excluded. Therefore, the structures corresponding to the lowest minima of the potential energy surface were further optimized without any coordinate constraint and are shown in Supplementary Fig. 53. The vibrational (at 298.15 K) and zero-point energy contributions were summed up to the electronical energy to obtain the free energy values reported in Supplementary Table 2 along with the three main geometrical parameters and the distance between the phenyl rings. The conclusion that emerges from the results in Supplementary Table 2 is that our calculation predict Z_A and Z_B isomers to have comparable stability.
To confirm this result, we compared the conformer energies obtained at our chosen level of theory with those given by other functionals that incorporate the empirical dispersion for VdW interactions. We performed single point calculations in gas phase on Z_A and Z_B structures with wB97X-D and M06-2X functionals. From the values of the energy difference between the two structures (Supplementary Table 3) we assess that the results align regardless of the specific functional used.
Starting from the structures Z_A and Z_B, we also investigated the thermal back-isomerization to the isomer E with a single scan of the azoimidazolium torsion. The energy profiles in function of the Ω dihedral, shown in Supplementary Fig. 56, highlight the presence of two minima centered at 180° (isomer E) and 0/360° (isomer Z) with the former having higher stability like a typical *cis-trans* system. The change of the other coordinates during the scan is also displayed in the same graphs. The structures of the two *trans* minima were further

optimized without any constrained applied to the coordinates to obtain *E*' and *E*'' geometries (Supplementary Fig. 53) and their free energy is reported in Supplementary Table 2. In addition, we also performed a double scan of the **Ω** dihedral and **α** angle (Supplementary Fig. 58) starting from the *E*' structure, from which we can assess the presence of the minima corresponding to the *E* isomer (**Ω** = 180°, **α** = 120°) and a combination of the *Z* diastereomers (**Ω** = 0°, **α** = 130°).

TDDFT calculations

We performed an optimization of the first two excited states S_1 and S_2 on the Frank-Condon geometry of the isomer *E''*. The maximum optimization step was set to 0.05 Bohr.
The energy evolution is shown in Supplementary Fig. 61 along with the values of dihedral for the $N = N$ torsion (**Ω**), and the $C - N = N$ bending (**α**, **β**).
Both optimizations did not reach full convergence, because along the pathway of energy relaxion on the two states the molecule encounters a region of avoided crossing to the lower state. Many authors highlighted that this is what happens for azobenzene and individuated conical intersection at these crossing, using multireference methods.[7,8,9,10,11] In Supplementary Fig. 61 we show the geometrical and energetic changes that occur during the TDDFT optimization on S_2 starting from the FC point (left panels) and on S_1 starting with the presumed crossing with S_2 (right panels). For both optimizations it is possible to distinguish two separate regions: an initial quick relaxation following the slope of the PES, followed by a sequence of fluctuations (shaded in grey) of the molecular geometries and of the energies once the (avoided) crossing with the underlying electronic states is reached. On S_2 the geometrical relaxation is minimal, while on S_1 bending angles increase while the torsion angle Ω decreases from about 180 to about 90 degrees for [**R3**]$^+$ and 100 for azobenzene. Although the systematic application of CASPT2 or similar methods is not affordable for [**R3**]$^+$, the similarity between the TDDFT S_0, S_1, and S_2 potential energy surfaces and those of obtained for azobenzene hints to a similar isomerization mechanism mainly determined by the variation of the torsion angle Ω. The TDDFT results were subsequently assessed by comparison with CASPT2 conical intersections obtained in explicit solvent (see below). The CASPT2 structures confirmed the presence of the electronic states crossings found by TDDFT (both S_2/S_1 and S_1/S_0) as well as the similarities between their PESs and those of pristine azobenzene (i.e., S_2/S_1 is found crossing close to FC point, while S_1/S_0 crossing is reached mainly by Ω torsion and opening of α, β angles) Although the systematic application CASPT2 or similar methods is not affordable for [**R3**]$^+$ the similarity between the TDDFT S_0, S_1, and S_2 potential energy surfaces and those of obtained for azobenzene hints to a similar isomerization mechanism mainly determined by the variation of the torsion angle **Ω**.

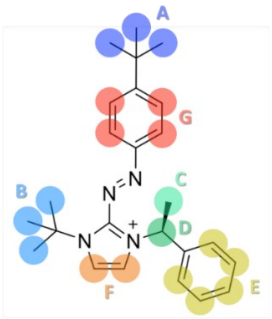

Supplementary Fig. 52. Visualization of [**R3**]$^+$ carbon atoms connected to the hydrogens responsible for the signals observed in the ^{1}H-NMR simulated spectrum.

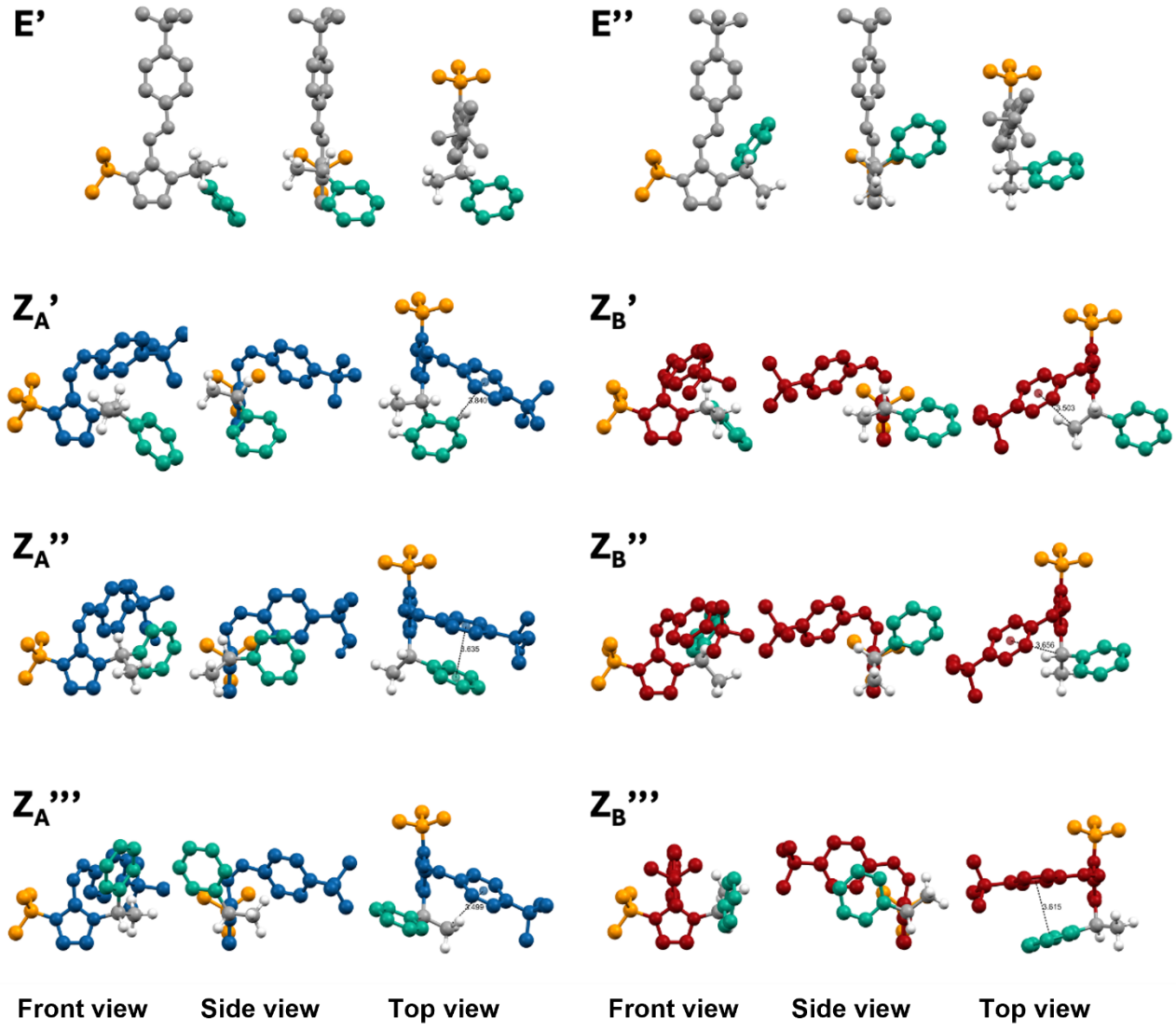

Supplementary Fig. 53. Optimized structure of the most important [**R3**]$^+$ conformers. All hydrogen atoms except those at the benzylic position and at the methyl substituent have been removed for clarity. In some cases, in the top view representations, the distance between the centroids of the phenyl and arylazo arene rings has been reported to highlight their π-stacking interaction.

a) b)

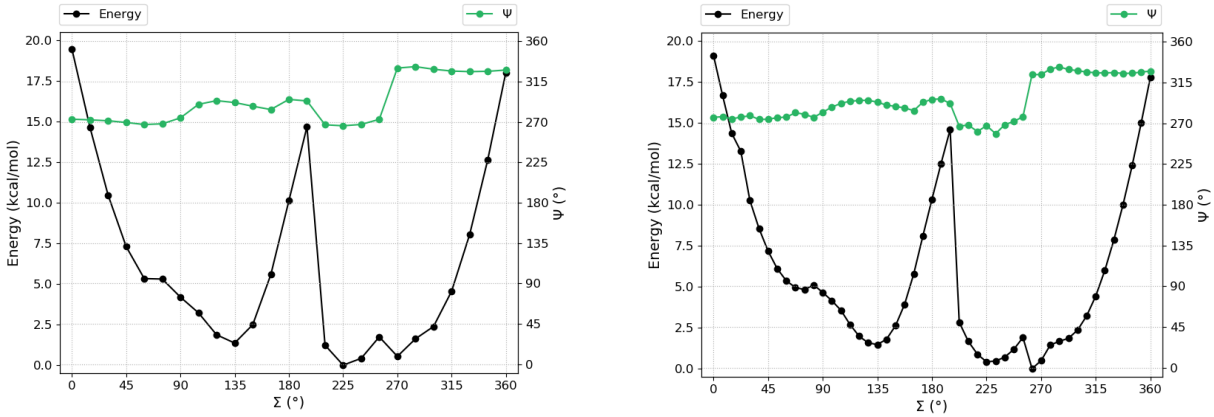

Supplementary Fig. 54. Energy profiles for the scan of the Σ dihedral for [**R3**]⁺ in gas phase (a) and PCM (b).

a)

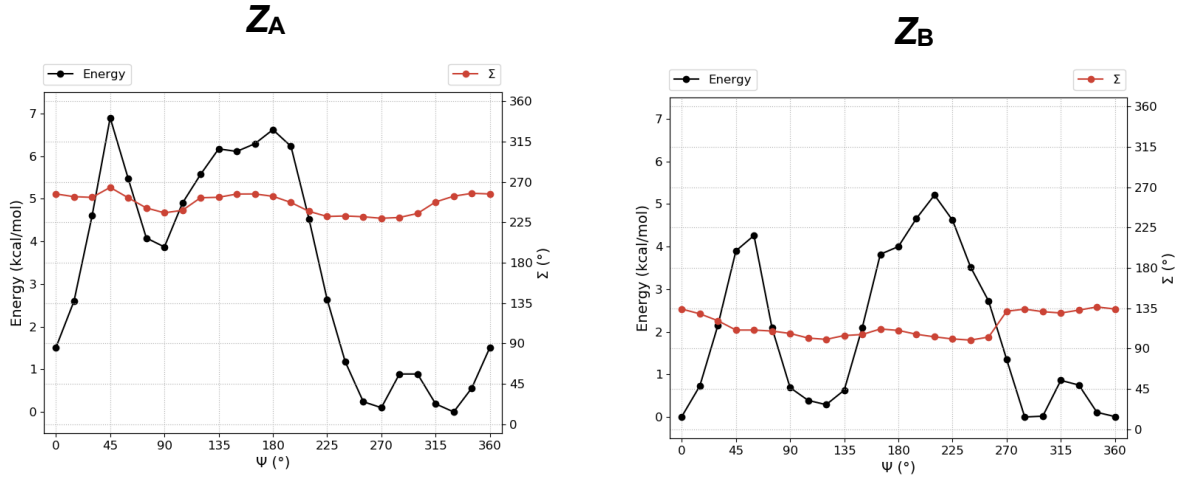

b)

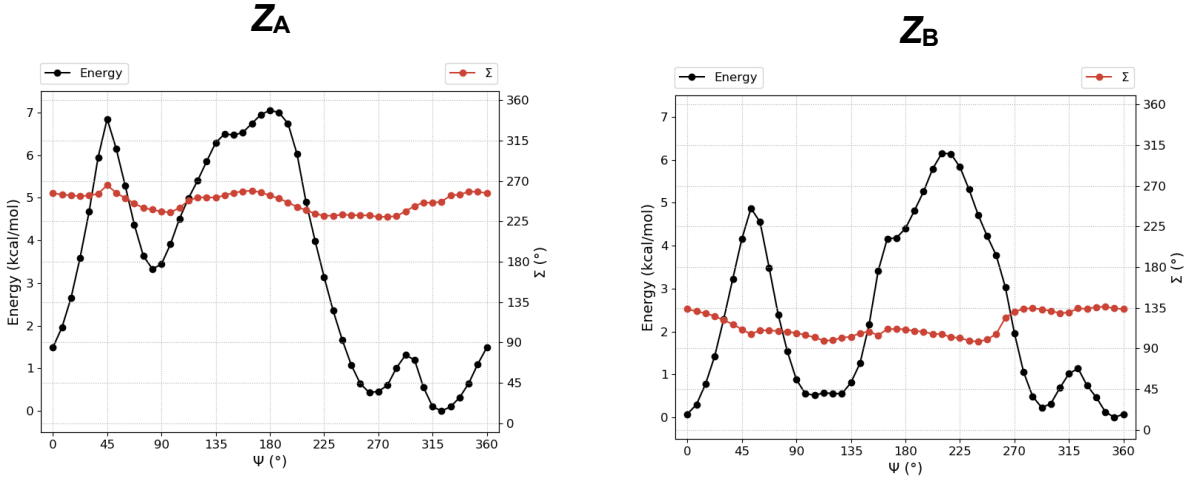

Supplementary Fig. 55. Energy profiles for the scan of the Ψ dihedral for [**R3**]⁺ in gas phase (a) and PCM (b), starting with the Σ = 225° (left) and the Σ = 135° geometry (right).

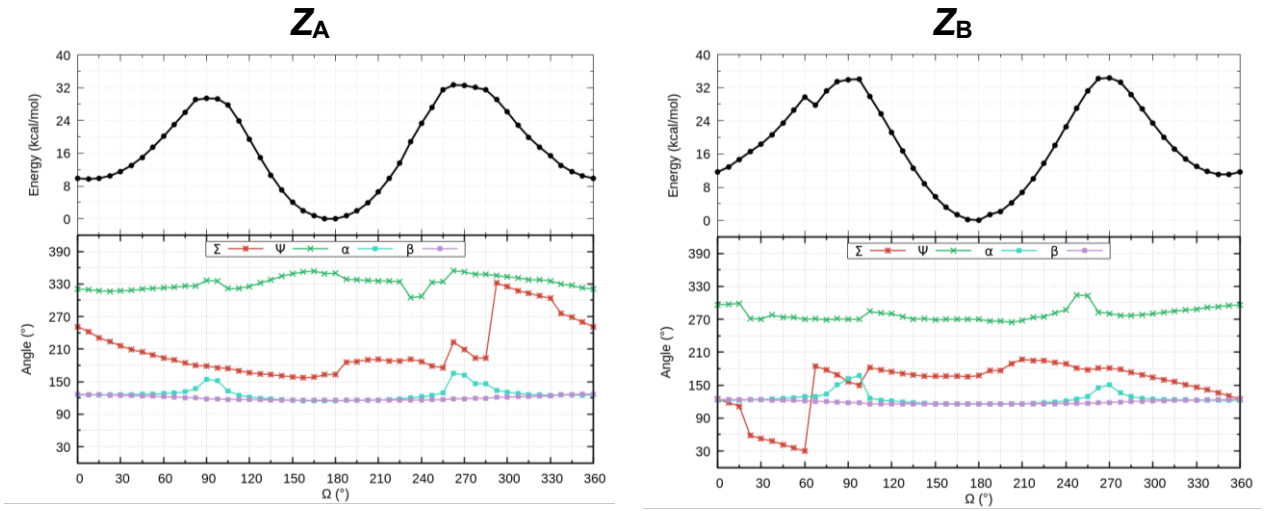

Supplementary Fig. 56. Single scan of **Ω** dihedral angle in PCM for [**R3**]⁺ starting from the optimized Z_A geometry (**Σ** = 243°, **Ψ** = 320°) and the optimized Z_B geometry (**Σ** = 133°, **Ψ** = 294°): energy profiles (top plates) and corresponding values of **Σ**, **Ψ** dihedrals and **α**, **β** angles (bottom plates).

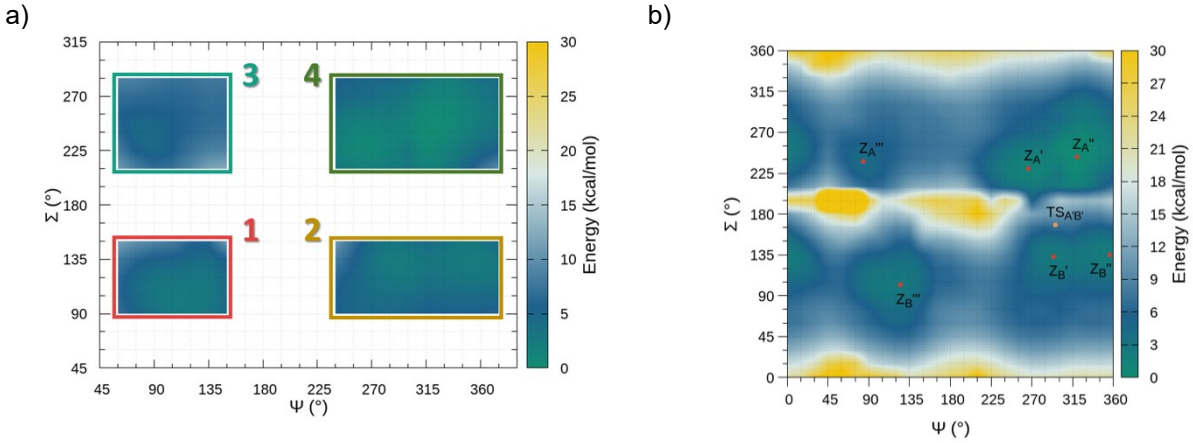

Supplementary Fig. 57 Ground state potential energy surface as a function of the **Σ** and **Ψ** coordinates of the four regions at lower energy in gas phase (a) and of the whole conformational space in chloroform (b) for [**R3**]⁺. The position of the structures shown in Supplementary Fig. 51 are marked in (b) along with the transition state between Z_A' and Z_B'.

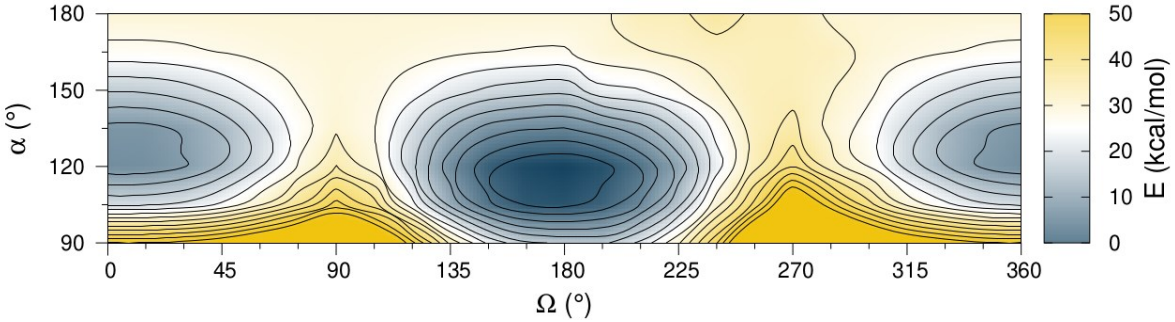

Supplementary Fig. 58. Ground state potential energy surface for [**R3**]⁺ as obtained from the double scan of **Ω** dihedral ($N = N$ torsion) and α bending ($C - N = N$) angles in chloroform, with E' as starting geometry.

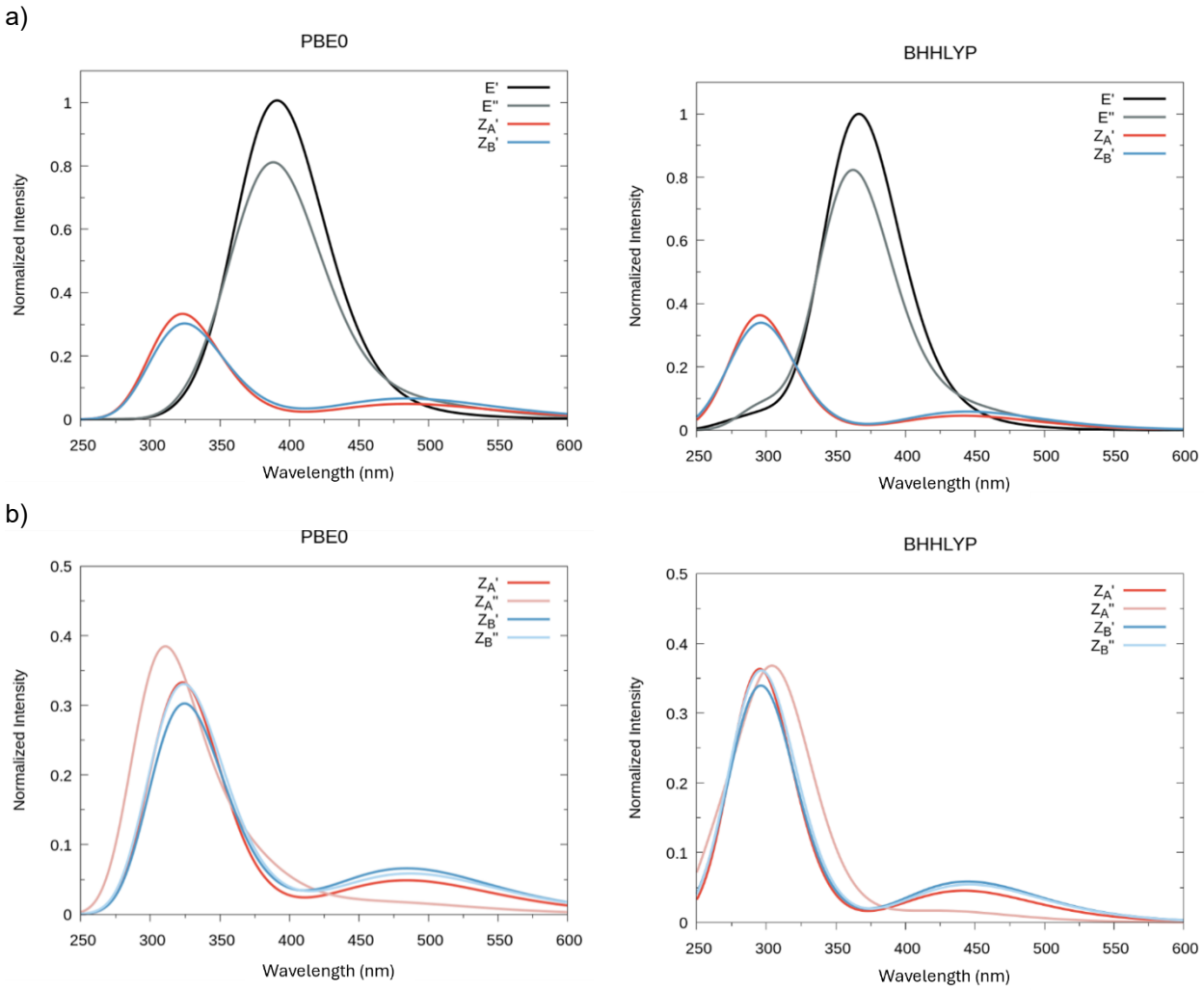

Supplementary Fig. 59. Absorption spectra of [**R3**]$^+$ conformers, calculated with TDDFT using the aug-cc-pVDZ basis set with PBE0-D3BJ and BHHLYP functionals in chloroform: a) comparison between *E*-*Z* isomers and b) between the first two most stable conformers of Z_A and Z_B. All spectra are calculated at the at their PBE0-D3BJ optimized geometries.

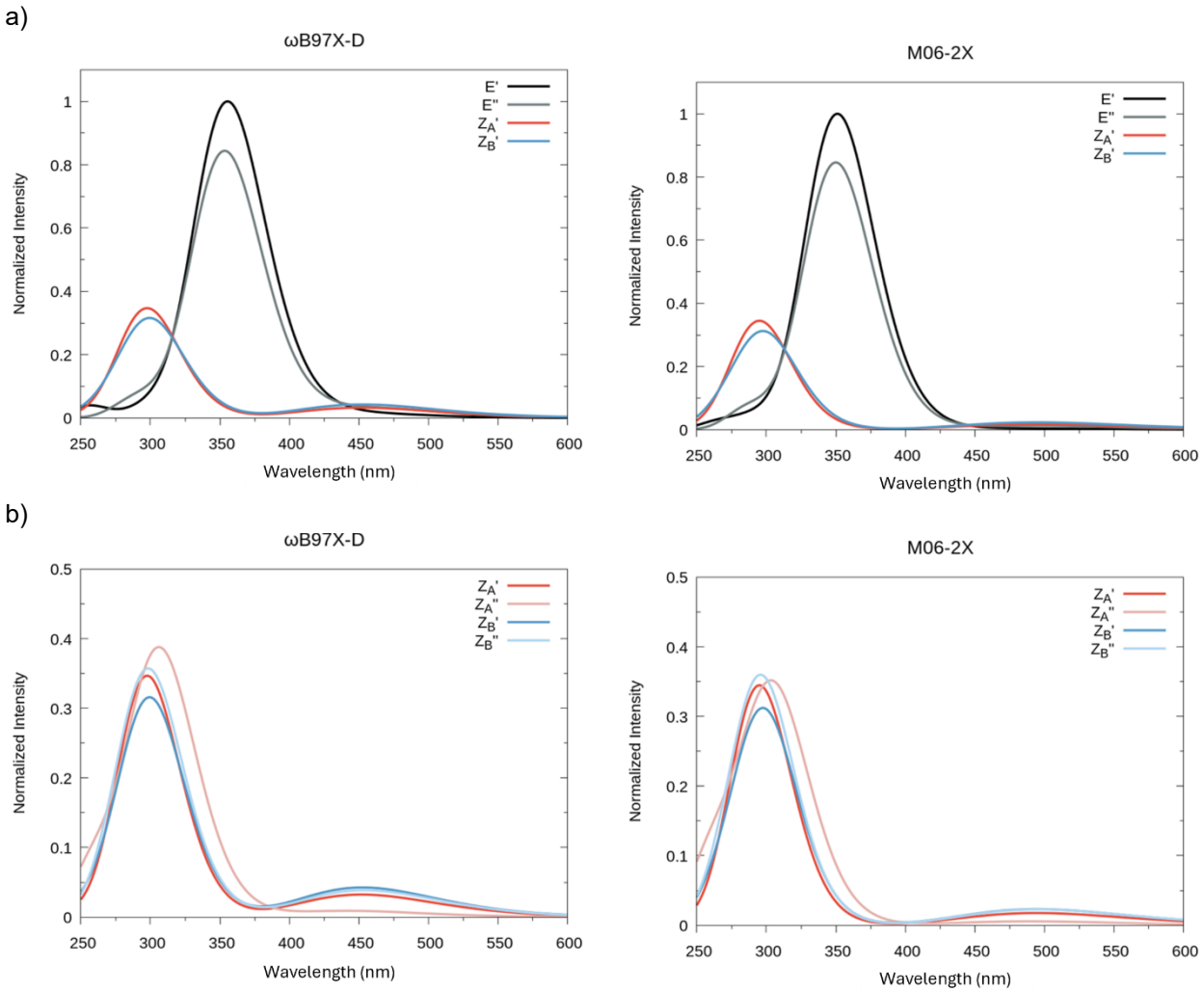

Supplementary Fig. 60. Absorption spectra of [**R3**]$^+$ conformers, calculated with TDDFT at their optimized geometries, using the aug-cc-pVDZ basis set with wB97X-D and M06-2X functionals in chloroform: a) comparison between *E-Z* isomers and b) between the first two most stable conformers of Z_A and Z_B.

a)

[R3]⁺ S_2

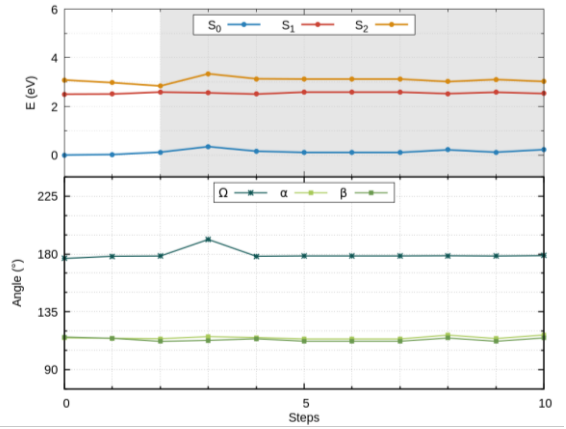

[R3]⁺ S_1

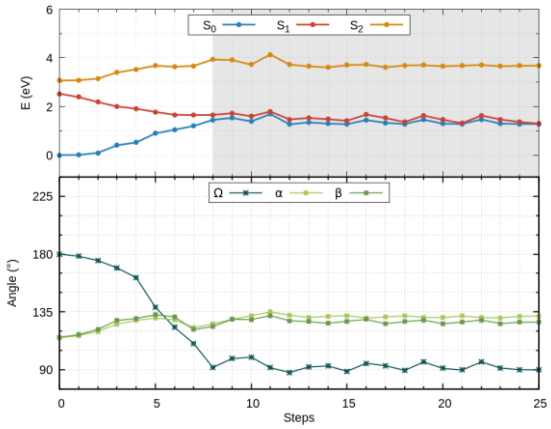

b)

Azobenzene S_2

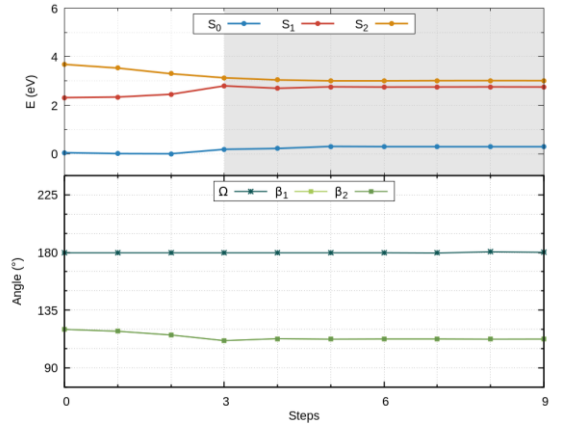

Azobenzene S_1

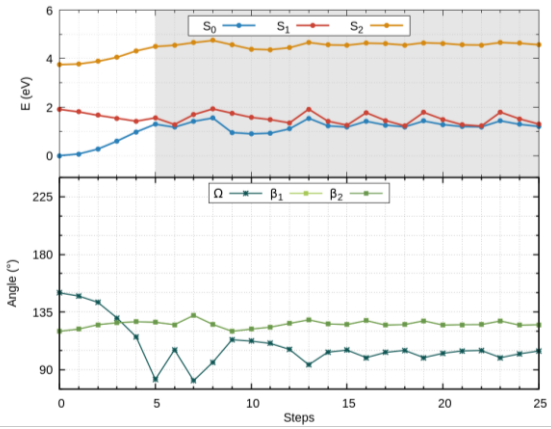

Supplementary Fig. 61. Energy trend of S_0, S_1 and S_2 states and corresponding evolution of **Ω** dihedral and $C-N=N$ **α**, **β** bending angles during excited state optimizations of [**R3**]⁺ (a) and azobenzene (b) for S_2 (left) and S_1 (right) states. The circles highlight the points of avoided crossing and of possible conical intersection between S_1 and S_2, and S_0 and S_1. For azobenzene the values of bending angles β_1, β_2 are identical and therefore only one appears in the plots.

Supplementary Table 2. Calculated free energy values (corrected with the vibrational zero-point energy) and geometrical parameters from unconstrained optimization and frequency calculations of **[R3]$^+$** conformers in gas phase and chloroform. The different *Z* conformers correspond to the energy minima shown in Supplementary Fig. 55. *D* indicates the distance between the centres of mass of the two phenyl rings.

	Gas phase				
	ΔG *kcal/mol*	Ω °	Σ °	Ψ °	*D* Å
Z_A' (R4)	-	-	-	-	-
Z_A'' (R4)	12.32	7	–116	–39	3.7
Z_A''' (R3)	-	-	-	-	-
Z_B' (R2)	13.32	–11	133	–68	6.7
Z_B'' (R2)	-	-	-	-	-
Z_B''' (R1)	-	-	-	-	-
E'	0.00	178	169	–93	8.0
E''	0.33	177	160	–10	5.0

	Chloroform				
	ΔG *kcal/mol*	Ω °	Σ °	Ψ °	*D* Å
Z_A' (R4)	11.10	9	–130	–94	5.2
Z_A'' (R4)	11.88	7	–117	–40	3.6
Z_A''' (R3)	15.25	7	–122	84	5.1
Z_B' (R2)	11.68	–11	133	-66	6.7
Z_B'' (R2)	11.71	–10	135	–4	5.4
Z_B''' (R1)	14.40	–1	102	125	3.6
E'	0.10	178	166	–90	7.9
E''	0.00	176	163	–10	5.0

Supplementary Table 3. Internal energy difference between [**R3**]$^+$ Z_A' and Z_B' structures calculated using different functionals and VdW corrections with the same basis set (aug-cc-pVDZ) in gas phase.

Functional	*ΔE kcal/mol*
PBE0 (D3BJ)	1.14
wB97X-D	1.33
M06-2X	0.66

Supplementary Table 4. Averaged chemical shifts (ppm) of [**R3**]$^+$ isomer optimized structures obtained from ^{1}H-NMR simulations in chloroform. Functional group classification and proton integration corresponds to the one depicted in Supplementary Fig. 50.

Group	Integratio	*E*'	*E*''	Z_A'	Z_A''	Z_B'	Z_B''
A	9	1.47	1.53	1.59	1.36	1.47	1.52
B	9	1.89	1.96	1.88	1.60	1.90	1.85
C	3	1.98	2.09	1.62	1.82	0.54	1.44
D	1	6.56	6.78	4.34	4.78	4.46	3.07
E	5	7.51	8.07	7.53	7.35	7.86	7.63
F	2	8.13	7.33	7.03	8.06	7.30	7.85
G	4	8.28	8.54	8.13	7.39	8.06	8.03

CASPT2 calculations

Gas phase calculations on ground state minima and transition states

We calculated the CASPT2 energy (gas phase) of the ground state minima and transition states structures obtained from DFT optimizations with the OpenMolcas software.[12] For doing so, the structure of the [**R3**]$^+$ ion was partitioned in QM/MM layers, placing the methyl and ter-butyl substituents in the MM layer, and filling the coordination vacancies created at the QM-MM boundaries with H atoms during the calculations (Supplementary Fig. 62)

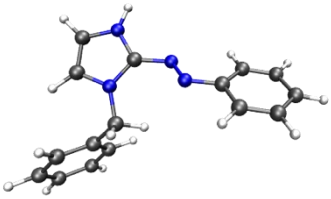

Supplementary Fig. 62. High layer (QM) atoms used for the QM/MM CASPT2 calculations on [**R3**]$^+$.

This partitioning ensured the inclusion of all the (photo)chemically relevant atoms in the CASPT2 calculations, while reducing the computational cost. The extended-multistate version of CASPT2 (XMS-CASPT2) was applied to the three lowest electronic singlet states obtained from SA3-CASSCF(10,8)/aug-cc-pVDZ calculations. The active space was composed of 10 electrons in 8 orbitals, which were selected to be the most relevant (*i.e.*, occupation farther from 0-2) across the different geometries to ensure active space stability and allow energy comparison. The selected active space orbitals are reported in Supplementary Fig. 63, while a comparison of relative energies and excited state properties is attempted in Supplementary Figures 64, 65 and Tables 5-9.

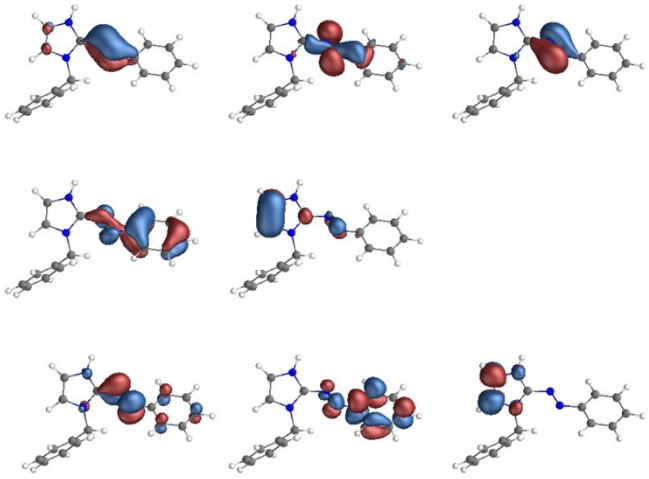

Supplementary Fig. 63. Active space molecular orbitals (SA-3-CASSCF(10,8)/aug-cc-pVDZ) used throughout all gas phase calculations on [**R3**]$^+$.

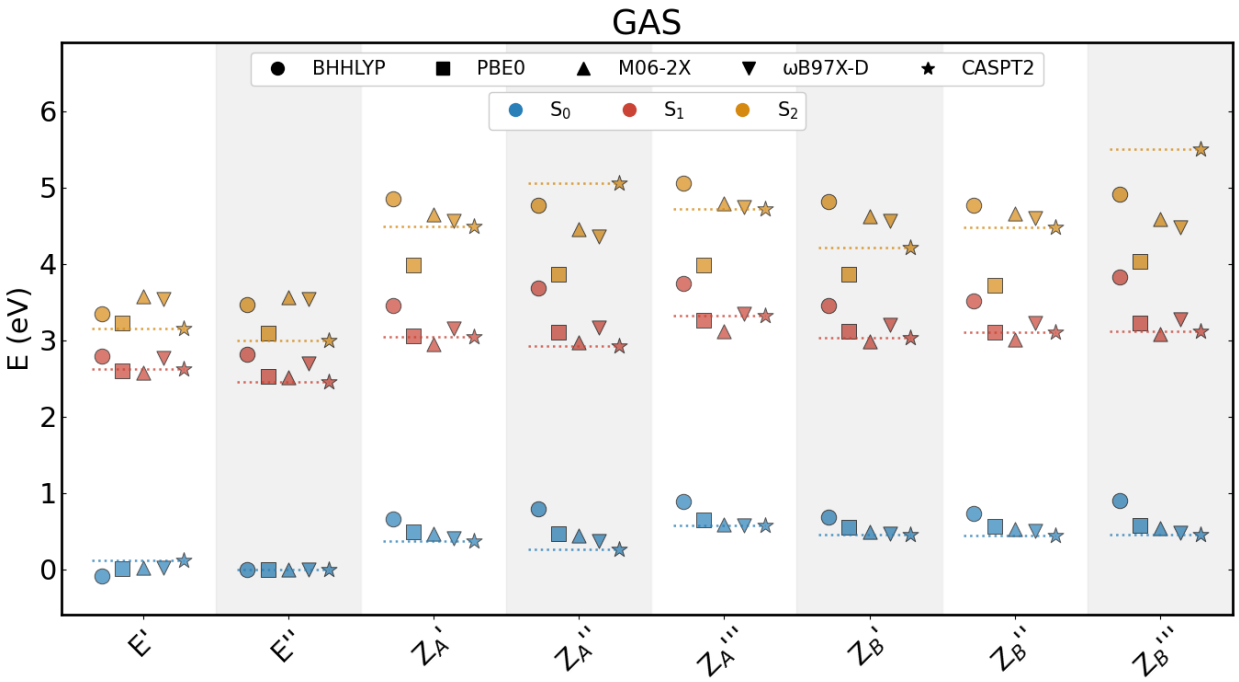

Supplementary Fig. 64. Comparison between gas phase XMS-CASPT2 (horizontal lines) and TDDFT S_0, S_1, S_2 energies obtained with different functionals for [**R3**]$^+$ conformers. All calculations were performed at the PBE0-D3BJ geometries, optimized in chloroform. With respect to XMS CASPT2, mean absolute errors in eV are 0.27 (S_0), 0.43 (S_1), 0.51 (S_2) for BHHLPY; 0.10 (S_0), 0.07 (S_1), 0.53 (S_2) for PBE0-D3BJ; 0.11 (S_0), 0.08 (S_1), 0.50 (S_2) for M06-2X; 0.06 (S_0), 0.16 (S_1), 0.46 (S_2) for wB97X-D, respectively. For each dataset, the energy scale is centred at the S_0 energy of the *E*'' conformer.

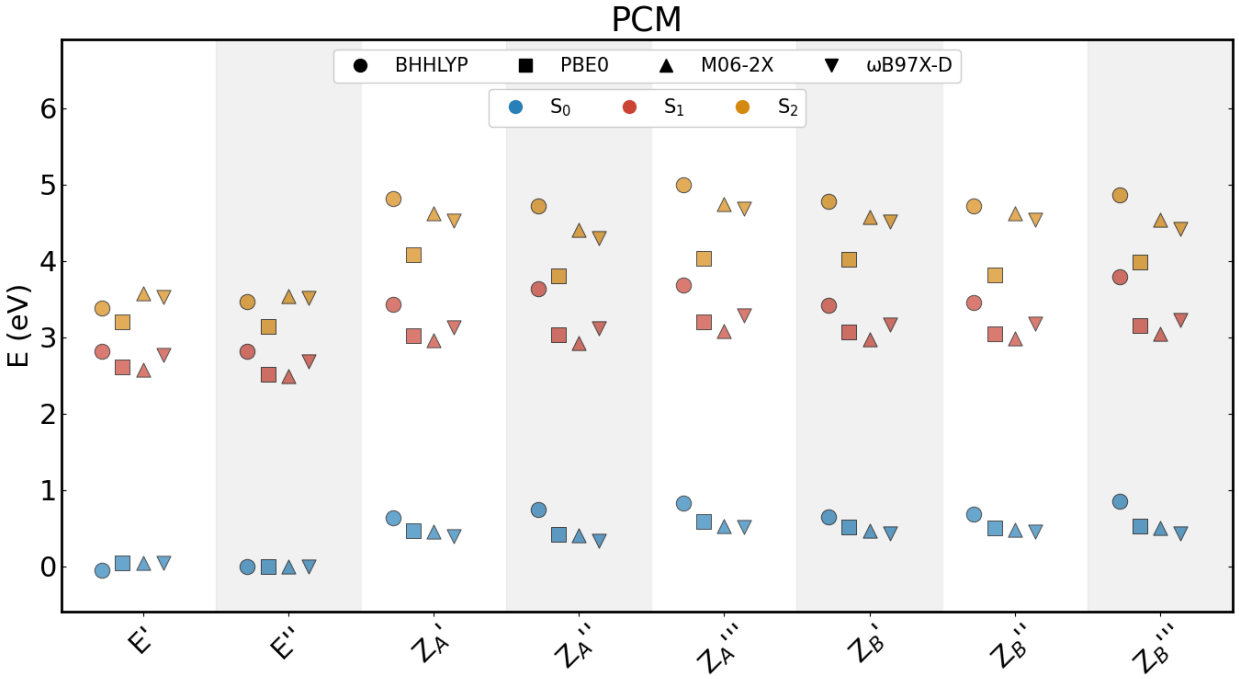

Supplementary Fig. 65. Comparison between TDDFT S_0, S_1, S_2 energies in chloroform for different functionals for [**R3**]$^+$ conformers. PBE0-D3BJ, M062-X and wB97X-D calculations were performed at the corresponding optimized geometries in chloroform. BHHLYP calculations were performed at the PBE0-D3BJ optimized geometries in chloroform. For each dataset, the energy scale is centred at the S_0 energy of the *E*'' conformer.

Supplementary Table 5. Gas phase XMS-CASPT2 energies for the first three electronic states and oscillator strength for $S_0 \rightarrow S_1$ and $S_0 \rightarrow S_2$ transitions, calculated for [**R3**]$^+$ conformers and transition states (TS) for clockwise (+) and counterclockwise (-) rotation about the azo bond. All calculations were performed at the PBE0-D3BJ optimized geometries in chloroform. The zero of the energy scale is set at the S_0 energy of the *E*'' conformer. Energies are given in eV units.

geometry	E_{S_0}	E_{S_1}	E_{S_2}	$f_{0\rightarrow1}$	$f_{0\rightarrow2}$
E'	0.11	2.62	3.15	0.01	0.59
E''	0.00	2.46	3.00	0.03	0.54
Z_A'	0.37	3.05	4.49	0.02	0.10
Z_A''	0.26	2.93	5.06	0.01	0.03
Z_A'''	0.57	3.32	4.72	0.02	0.10
Z_B'	0.45	3.03	4.21	0.04	0.16
Z_B''	0.44	3.10	4.48	0.02	0.10
Z_B'''	0.45	3.12	5.51	0.01	0.00
TS Z_A +	1.04	2.08	4.27	0.00	0.01
TS Z_A -	1.32	2.65	4.47	0.03	0.02
TS Z_B +	1.49	2.76	4.83	0.02	0.01
TS Z_B -	1.50	2.24	4.19	0.00	0.01

Supplementary Table 6. Gas phase BHHLYP energies for the first three electronic states and oscillator strength for $S_0 \rightarrow S_1$ and $S_0 \rightarrow S_2$ transitions, calculated for [**R3**]$^+$ conformers and transition states (TS) for clockwise (+) and counterclockwise (-) rotation about the azo bond. All calculations were performed at the PBE0-D3BJ optimized geometries in chloroform. The zero of the energy scale is set at the S_0 energy of the *E*'' conformer. Energies are given in eV units.

geometry	E_{S_0}	E_{S_1}	E_{S_2}	$f_{0\rightarrow1}$	$f_{0\rightarrow2}$
E'	-0.09	2.79	3.35	0.02	0.91
E''	0.00	2.82	3.47	0.04	0.72
Z_A'	0.66	3.46	4.85	0.04	0.33
Z_A''	0.79	3.69	4.77	0.01	0.24
Z_A'''	0.89	3.74	5.06	0.04	0.13
Z_B'	0.68	3.46	4.82	0.06	0.28
Z_B''	0.73	3.51	4.77	0.05	0.07
Z_B'''	0.90	3.83	4.92	0.00	0.29
TS Z_A +	1.58	2.73	5.01	0.00	0.21
TS Z_A -	1.66	3.04	5.23	0.02	0.28
TS Z_B +	1.54	2.88	5.31	0.01	0.56
TS Z_B -	1.54	2.51	5.16	0.00	0.02

Supplementary Table 7. Gas phase PBE0-D3BJ energies for the first three electronic states and oscillator strength for $S_0 \rightarrow S_1$ and $S_0 \rightarrow S_2$ transitions, calculated for [**R3**]$^+$ conformers and transition states (TS) for clockwise (+) and counterclockwise (-) rotation about the azo bond. All calculations were performed at the PBE0-D3BJ optimized geometries in chloroform. The zero of the energy scale is set at the S_0 energy of the *E*'' conformer. Energies are given in eV units.

geometry	E_{S_0}	E_{S_1}	E_{S_2}	$f_{0\rightarrow1}$	$f_{0\rightarrow2}$
E'	0.01	2.60	3.22	0.01	0.75
E''	0.00	2.53	3.09	0.03	0.15
Z_A'	0.49	3.06	3.99	0.04	0.00
Z_A''	0.47	3.10	3.86	0.01	0.06
Z_A'''	0.65	3.26	3.98	0.04	0.01
Z_B'	0.55	3.12	3.87	0.06	0.01
Z_B''	0.56	3.11	3.72	0.05	0.00
Z_B'''	0.57	3.22	4.03	0.00	0.06
TS Z_A +	1.26	2.09	3.96	0.00	0.02
TS Z_A -	1.42	2.65	4.19	0.02	0.00
TS Z_B +	1.49	2.60	4.47	0.02	0.01
TS Z_B -	1.50	2.15	3.96	0.00	0.00

Supplementary Table 8. Gas phase M06-2X energies for the first three electronic states and oscillator strength for $S_0 \rightarrow S_1$ and $S_0 \rightarrow S_2$ transitions, calculated for [**R3**]$^+$ conformers and transition states (TS) for clockwise (+) and counterclockwise (-) rotation about the azo bond. All calculations were performed at the

PBE0-D3BJ optimized geometries in chloroform. The zero of the energy scale is set at the S_0 energy of the *E*'' conformer. Energies are given in eV units.

geometry	E_{S_0}	E_{S_1}	E_{S_2}	$f_{0\rightarrow1}$	$f_{0\rightarrow2}$
E'	0.02	2.57	3.57	0.00	0.87
E''	0.00	2.51	3.56	0.01	0.70
Z_A'	0.46	2.95	4.65	0.02	0.29
Z_A''	0.44	2.97	4.46	0.00	0.25
Z_A'''	0.59	3.12	4.79	0.02	0.24
Z_B'	0.49	2.98	4.62	0.02	0.27
Z_B''	0.53	3.01	4.66	0.02	0.22
Z_B'''	0.54	3.08	4.59	0.00	0.27
TS Z_A +	1.35	2.11	4.75	0.00	0.21
TS Z_A -	1.53	2.54	5.07	0.01	0.34
TS Z_B +	1.59	2.55	5.32	0.01	0.58
TS Z_B -	1.62	2.19	5.26	0.00	0.06

Supplementary Table 9. Gas phase wB97X-D energies for the first three electronic states and oscillator strength for $S_0\rightarrow S_1$ and $S_0\rightarrow S_2$ transitions, calculated for [**R3**]$^+$ conformers and transition states (TS) for clockwise (+) and counterclockwise (-) rotation about the azo bond. All calculations were performed at the PBE0-D3BJ optimized geometries in chloroform. The zero of the energy scale is set at the S_0 energy of the *E*'' conformer. Energies are given in eV units.

geometry	E_{S_0}	E_{S_1}	E_{S_2}	$f_{0\rightarrow1}$	$f_{0\rightarrow2}$
E'	0.02	2.77	3.54	0.01	0.85
E''	0.00	2.70	3.54	0.02	0.69
Z_A'	0.41	3.15	4.57	0.03	0.30
Z_A''	0.37	3.17	4.36	0.01	0.23
Z_A'''	0.57	3.35	4.75	0.03	0.24
Z_B'	0.47	3.20	4.57	0.04	0.24
Z_B''	0.50	3.23	4.60	0.03	0.23
Z_B'''	0.48	3.28	4.48	0.00	0.27
TS Z_A +	1.24	2.36	4.66	0.00	0.22
TS Z_A -	1.46	2.78	4.99	0.02	0.33
TS Z_B +	1.52	2.81	5.22	0.01	0.47
TS Z_B -	1.52	2.45	5.13	0.00	0.25

Supplementary Table 10. BHHLYP energies for the first three electronic states and oscillator strength for $S_0\rightarrow S_1$ and $S_0\rightarrow S_2$ transitions, calculated in chloroform for [**R3**]$^+$ conformers and transition states (TS) for clockwise (+) and counterclockwise (-) rotation about the azo bond. All calculations were performed at the PBE0-D3BJ optimized geometries in chloroform. The zero of the energy scale is set at the S_0 energy of the *E*'' conformer. Energies are given in eV units.

geometry	E_{S_0}	E_{S_1}	E_{S_2}	$f_{0\rightarrow1}$	$f_{0\rightarrow2}$
E'	-0.06	2.82	3.38	0.02	0.91
E''	0.00	2.82	3.47	0.04	0.72
Z_A'	0.63	3.43	4.82	0.04	0.33
Z_A''	0.74	3.64	4.72	0.01	0.24
Z_A'''	0.83	3.68	5.00	0.04	0.13
Z_B'	0.64	3.42	4.78	0.06	0.28
Z_B''	0.68	3.46	4.72	0.05	0.07
Z_B'''	0.85	3.79	4.87	0.00	0.29
TS Z_A +	1.59	2.71	5.03	0.00	0.34
TS Z_A -	1.67	2.99	5.24	0.03	0.66
TS Z_B +	1.56	2.87	5.29	0.02	0.76
TS Z_B -	1.57	2.54	5.20	0.00	0.67

Supplementary Table 11. PBE0-3DBJ energies for the first three electronic states and oscillator strength for $S_0 \rightarrow S_1$ and $S_0 \rightarrow S_2$ transitions, calculated in chloroform for [**R3**]$^+$ conformers and transition states (TS) for clockwise (+) and counterclockwise (-) rotation about the azo bond. All calculations were performed at the PBE0-D3BJ optimized geometries in chloroform. The zero of the energy scale is set at the S_0 energy of the *E*'' conformer. Energies are given in eV units.

geometry	E_{S_0}	E_{S_1}	E_{S_2}	$f_{0\rightarrow1}$	$f_{0\rightarrow2}$
E'	0.04	2.61	3.20	0.02	1.00
E''	0.00	2.51	3.14	0.05	0.59
Z_A'	0.46	3.02	4.08	0.06	0.01
Z_A''	0.42	3.03	3.81	0.02	0.08
Z_A'''	0.59	3.20	4.03	0.05	0.02
Z_B'	0.51	3.07	4.02	0.08	0.02
Z_B''	0.50	3.05	3.82	0.07	0.01
Z_B'''	0.53	3.15	3.99	0.00	0.09
TS Z_A +	1.28	2.08	4.02	0.00	0.04
TS Z_A -	1.42	2.61	4.35	0.03	0.00
TS Z_B +	1.51	2.60	4.71	0.02	0.02
TS Z_B -	1.53	2.18	4.31	0.00	0.00

Supplementary Table 12. M06-2X energies for the first three electronic states and oscillator strength for $S_0 \rightarrow S_1$ and $S_0 \rightarrow S_2$ transitions, calculated in chloroform for [**R3**]$^+$ conformers and transition states (TS) for clockwise (+) and counterclockwise (-) rotation about the azo bond. Calculations for conformers were performed at the M06-2X optimized geometries in chloroform, while calculations for transition states were performed at the PBE0-D3BJ optimized geometries in chloroform. The zero of the energy scale is set at the S_0 energy of the E'' conformer. Energies are given in eV units.

geometry	E_{S_0}	E_{S_1}	E_{S_2}	$f_{0\rightarrow1}$	$f_{0\rightarrow2}$
E'	0.04	2.57	3.57	0.00	1.02
E''	0.00	2.49	3.54	0.01	0.86
Z_A'	0.45	2.96	4.63	0.02	0.39
Z_A''	0.40	2.93	4.41	0.01	0.34
Z_A'''	0.53	3.08	4.75	0.02	0.34
Z_B'	0.46	2.97	4.58	0.03	0.34
Z_B''	0.48	2.99	4.62	0.03	0.37
Z_B'''	0.50	3.04	4.54	0.00	0.36
TS Z_A +	1.38	2.11	4.78	0.00	0.33
TS Z_A -	1.54	2.51	5.09	0.01	0.67
TS Z_B +	1.63	2.56	5.32	0.01	0.76
TS Z_B -	1.66	2.22	5.27	0.00	0.70

Supplementary Table 13. wB97X-D energies for the first three electronic states and oscillator strength for $S_0 \rightarrow S_1$ and $S_0 \rightarrow S_2$ transitions, calculated in chloroform for [**R3**]$^+$ conformers and transition states (TS) for clockwise (+) and counterclockwise (-) rotation about the azo bond. Calculations for conformers were performed at the wB97X-D optimized geometries in chloroform, while calculations for transition states were performed at the PBE0-D3BJ optimized geometries in chloroform. The zero of the energy scale is set at the S_0 energy of the E'' conformer. Energies are given in eV units.

geometry	E_{S_0}	E_{S_1}	E_{S_2}	$f_{0\rightarrow1}$	$f_{0\rightarrow2}$
E'	0.04	2.77	3.53	0.01	1.00
E''	0.00	2.68	3.51	0.03	0.84
Z_A'	0.39	3.13	4.53	0.04	0.38
Z_A''	0.33	3.12	4.30	0.01	0.33
Z_A'''	0.51	3.29	4.69	0.04	0.36
Z_B'	0.43	3.17	4.52	0.05	0.31
Z_B''	0.45	3.18	4.54	0.05	0.35
Z_B'''	0.43	3.23	4.42	0.00	0.38
TS Z_A +	1.27	1.99	4.67	0.00	0.33
TS Z_A -	1.47	2.44	5.02	0.01	0.67
TS Z_B +	1.55	2.48	5.24	0.01	0.76
TS Z_B -	1.55	2.11	5.15	0.00	0.70

Optimization of conical intersections in chloroform

The geometries of the minimum energy CIs between S_2/S_1 and S_1/S_0 of [**R3**]$^+$ in chloroform were optimized using multireference methods (CASPT2/CASSCF) and applying the QM/MM scheme.

As starting structures for QM/MM setup and subsequent optimization, we have extracted the geometry showing the minimum energy gap from the TDDFT excited state optimization (see Supplementary Fig. 61). In both cases, the TDDFT structure was solvated in an octahedral box of chloroform molecules with buffer distance 20 Å, including one Cl^- counterion. Afterwards, we performed an MM optimization run (500 steepest descent + 500 conjugate gradient steps) and two molecular dynamics simulations: a thermalization run at constant volume (20 ps, time step 0.02 ps) to bring the sample to the target temperature of 300 K, followed by an second simulation (100 ps, time step 0.02 ps) at constant temperature to equilibrate the sample at the target pressure of 1 atm. In all these MM calculations, we have used periodic boundary conditions, and we have kept the geometry of the [**R3**]$^+$ ion frozen to retain the TDDFT structure. Non-bonded interactions were always truncated at 12 Å. Using the equilibrated sample, we have cut a droplet of solvent including [**R3**]$^+$ and the 400 closest chloroform molecules. All these setup steps were performed using the automated utilities of COBRAMM[13,14] interfaced with AmberTools,[15] while calculations all QM/MM calculations were performed with COBRAMM[13,14] interfaced with OpenMolcas.[12] The QM/MM partitioning for subsequent optimizations is as follows: the high layer (QM atoms) included the [**R3**]$^+$ ion, excluding the $–CH_3$ and -*t*-Bu residues (Supplementary Fig. 62); the medium layer (movable MM atoms) included the $–CH_3$ and -*t*-Bu residues of [**R3**]$^+$, as well as all the chloroform molecules within a distance of 4 Å from the high layer atoms. The dangling bonds originated by the QM/MM partitioning of the [**R3**]$^+$ molecule were saturated with H atoms for the QM/MM calculations. Eventually, the solvent molecules in the outer solvation shell were put in the low layer (frozen MM atoms). The conical intersection geometries were optimized at the XMS-CASPT2/CASSCF(12,10)/aug-cc-pVDZ level of theory, including 2 and 3 electronic states in the state averaging procedure for S_1/S_0 and S_2/S_1 CI optimization, respectively. The active space was composed of 12 electrons in 10 orbitals and includes all the most relevant π, $\pi^*$and n orbitals of the azo system, plus some benzyl π orbitals that showed to be relevant for active space stability and accurate wavefunction description of the excited states (see Supplementary Fig. 66 and 67). Due to the high computational cost (average time per CI optimization step: 42.5 h and 58.0 h for S_1/S_0 and S_2/S_1 CI, respectively) combined with the large number of degrees of freedom of the QM/MM system, it was not possible to reach a full convergence. However, both calculations reached a plateau, in which the two considered electronic states are degenerate (see Supplementary Fig. 68). In both cases, the quasi-converged structures (displayed in Supplementary Fig. 68) are similar to the starting TDDFT geometries (cartesian RMSD of high layer: 0.166 and 0.163 Å for S_2/S_1 and S_1/S_0 CI optimizations, respectively) thus validating the TDDFT results. At the S_2/S_1 CASPT2 minimum-energy crossing point the azo-system is almost planar (Ω = 172°). Indeed, this CI lies close to the S_0 minimum (Franck-Condon point), from which it is reached mainly by closing the two C-N=N angles (α, β). Instead, the lowest energy S_1/S_0 crossing lies further away from the FC region and shows a twisted geometry (Ω = 98°) with wider α, β angles.

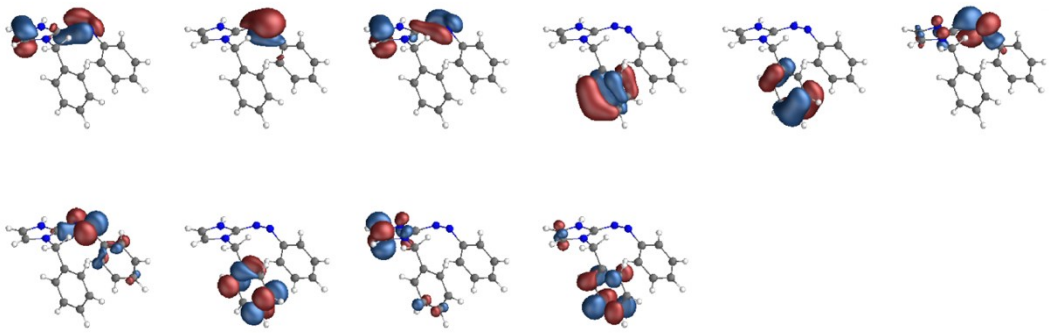

Supplementary Fig. 66. Active space molecular orbitals (SA-2-CASSCF(12,10)/aug-cc-pVDZ) used for the QM/MM optimization of S_1/S_0 CI of [**R3**]$^+$.

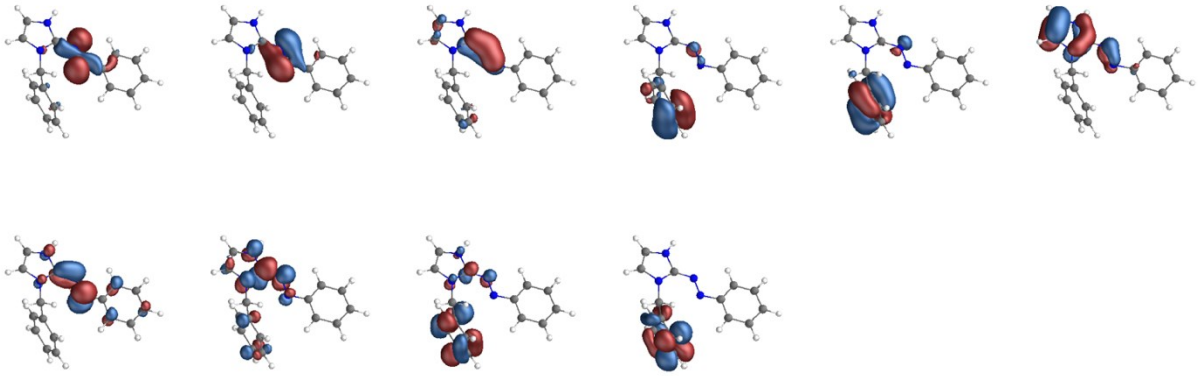

Supplementary Fig. 67. Active space molecular orbitals (SA-3-CASSCF(12,10)/aug-cc-pVDZ) used for the QM/MM optimization of S_2/S_1 CI of [**R3**]$^+$.

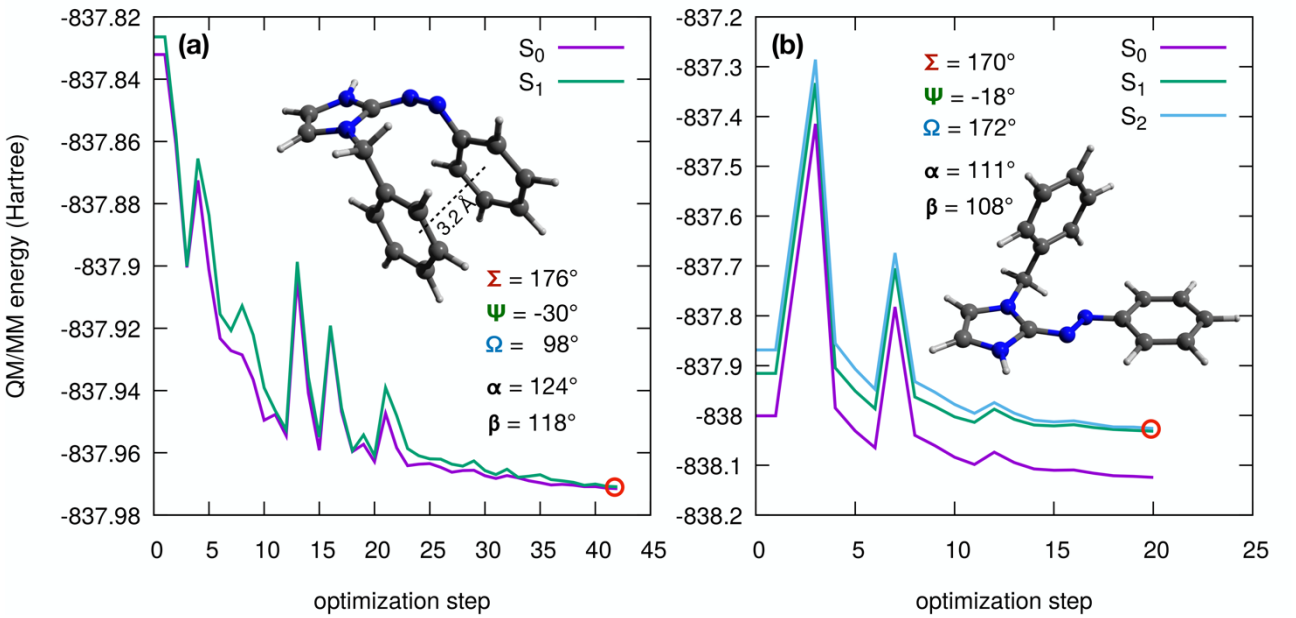

Supplementary Fig. 68. QM/MM energy profiles along the conical intersection optimizations of (a) S_1/S_0 states and (b) S_2/S_1 states of [**R3**]$^+$. The red circles highlight the optimization steps considered as quasi-converged geometries (step 43 and 20 for S_1/S_0 and S_2/S_1 CI, respectively). The corresponding structures (high layer, QM atoms) are reported together with values of the most relevant dihedrals (Σ, Ψ, Ω) and bending angles (α, β).

6. Kinetic considerations

The ratcheting constant (K_r) is defined as the ratio between the product of the rate constants of all the processes occurring within the closed reaction network that go in a direction (clockwise or counter-clockwise) and that of the rate constants of all the processes that go in the opposite direction (counter-clockwise or clockwise). In the presented system, by labelling the three reactions as follows, the K_r can be expressed as:

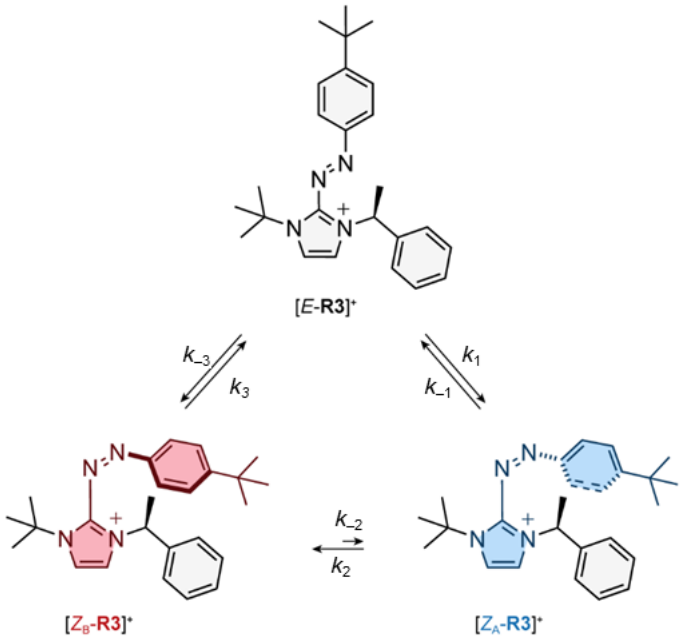

Supplementary Fig. 69. Triangular reaction network for the directional operation of [**R3**]$^+$. The six kinetic constants related to the three processes composing the network are labelled according to their individual directionality (clockwise or counterclockwise).

$$K_r = \frac{k_1}{k_{-1}} \times \frac{k_2}{k_{-2}} \times \frac{k_3}{k_{-3}}$$

As described in previous studies,[16,17] K_r can be estimated from the PSS concentrations of the photochemical processes (1 and 3) and the equilibrium concentrations of the thermal process 2. The resulting equation appears as

$$K_r = \frac{[Z_A]_{PSS}}{[E]_{PSS}} \times \frac{[Z_B]_{eq}}{[Z_A]_{eq}} \times \frac{[E]_{PSS}}{[Z_B]_{PSS}} = \frac{[Z_A]_{PSS}}{[Z_B]_{PSS}} \times \frac{[Z_B]_{eq}}{[Z_A]_{eq}}$$

In the irradiation regime used, the ratcheting constant results in $K_{r(CW/CCW)}$ = 0.92 under UV irradiation and $K_{r(CW/CCW)}$ = 1.08 under visible light irradiation, which translate into one directional rotation every 12 turns on average.

7. References

[1] Casimiro, L. et al. 4,4′-Dimethylazobenzene as a chemical actinometer. *Photochem. Photobiol. Sci.* **21**, 825-833 (2022).
[2] Fischer, E. The Calculation of Photostationary State in Systems A-B When Only A Is Known. *J. Phys. Chem.* **71**, 3704-3706 (1967).
[3] Stranius, K. & Börjesson, K. Determining the Photoisomerization Quantum Yield of Photoswitchable Molecules in Solution and in the Solid State. *Sci. Rep.* **7**, 41145 (2017).
[4] Hansen, M. J., Lerch, M. M., Szymanski, V. & Feringa, B. L. Direct and Versatile Synthesis of Red-Shifted Azobenzenes. *Angew. Chem. Int. Ed.* **55**, 13514-13518 (2016).
[5] Sauerbrey, S. et al. Synthesis, Structure, and Reactions of 1-*tert*-Butyl-2-diphenylphosphino-imidazole. *Inorg. Chem.* **50**, 793-799 (2011).
[6] Newman, S. G., Bryan, C. S., Perez, D. & Lautens, M. The Use of Bromotrichloromethane in Chlorination Reactions. *Synthesis* **2**, 0342-0346 (2011).
[7] Aleotti, F. et al. Multidimensional Potential Energy Surfaces Resolved at the RASPT2 Level for Accurate Photoinduced Isomerization Dynamics of Azobenzene. *J. Chem. Theory Comput.* **15**, 6813-6823 (2019).
[8] Nenov, A. et al. UV-Light-Induced Vibrational Coherences: The Key to Understand Kasha Rule Violation in trans-Azobenzene. *J. Phys. Chem. Lett.* **9**, 1534-1541 (2018).
[9] Casellas, J., Bearpark, M. J. & Reguero, M. Excited-state decay in the photoisomerization of azobenzene: a new balance between mechanisms. *ChemPhysChem* **17**, 3068-3079 (2016).
[10] Conti, I., Garavelli, M. & Orlandi, G. The Different Photoisomerization Efficiency of Azobenzene in the Lowest nπ* and ππ* Singlets: The Role of a Phantom State. *J. Am. Chem. Soc.* **130**, 5216-5230 (2008).
[11] Cattaneo, P. & Persico, M. An abinitio study of the photochemistry of azobenzene. *Phys. Chem. Chem. Phys.* **1**, 4739-4743 (1999).
[12] Li Manni, G. et al. The OpenMolcas Web: A Community-Driven Approach to Advancing Computational Chemistry. *J. Chem. Theory Comput.* **19**, 6933-6991 (2023).
[13] Weingart, O. et al. COBRAMM 2.0 — A software interface for tailoring molecular electronic structure calculations and running nanoscale (QM/MM) simulations. *J. Mol. Model.* **24**, 271 (2018).
[14] https://gitlab.com/cobrammgroup/cobramm/-/wikis/home.
[15] Case, D. A. et al. AmberTools. *J. Chem. Inf. Model.* **63**, 6183-6191 (2023).
[16] Corra, S. et al. Kinetic and energetic insights into the dissipative non-equilibrium operation of an autonomous light-powered supramolecular pump. *Nat. Nanotechnol*. **17**, 746-751 (2022).
[17] Sangchai, T., Al Shehimy, S., Penocchio, E.& Ragazzon, G. Artificial Molecular Ratchets: Tools Enabling Endergonic Processes. *Angew. Chem. Int. Ed*. **62**, e202309501 (2023).